THERMAL AND THERMOELECTRIC TRANSPORT IN CARBON-BASED NANOMATERIALS

A DISSERTATION

SUBMITTED TO THE DEPARTMENT OF

ELECTRICAL ENGINEERING

AND THE COMMITTEE ON GRADUATE STUDIES

OF STANFORD UNIVERSITY

IN PARTIAL FULFILLMENT OF THE REQUIREMENTS

FOR THE DEGREE OF

DOCTOR OF PHILOSOPHY

Feifei Lian
March 2018

This dissertation is online at: http://purl.stanford.edu/cf602pw1835

I certify that I have read this dissertation and that, in my opinion, it is fully adequate in scope and quality as a dissertation for the degree of Doctor of Philosophy.

Eric Pop, Primary Adviser

I certify that I have read this dissertation and that, in my opinion, it is fully adequate in scope and quality as a dissertation for the degree of Doctor of Philosophy.

Zhenan Bao

I certify that I have read this dissertation and that, in my opinion, it is fully adequate in scope and quality as a dissertation for the degree of Doctor of Philosophy.

Kenneth Goodson

I certify that I have read this dissertation and that, in my opinion, it is fully adequate in scope and quality as a dissertation for the degree of Doctor of Philosophy.

H.S.Philip Wong

Approved for the Stanford University Committee on Graduate Studies.

Patricia J. Gumport, Vice Provost for Graduate Education

This signature page was generated electronically upon submission of this dissertation in electronic format. An original signed hard copy of the signature page is on file in University Archives.

Abstract

Thermoelectric (TE) energy harvesting was first used by NASA in 1961 but has been too inefficient and expensive for widespread applications on Earth. Conventional TE materials (Bi_2Te_3 and PbTe) rely on rare minerals, making it difficult to reduce costs. In contrast, carbon is an abundant material, and carbon-based TEs could decrease costs and increase adoption of thermal energy scavenging technologies, particularly by taking advantage of carbon nanostructures. To optimize such TEs, it is important to understand key yet interdependent material properties, such as thermopower or Seebeck coefficient (S), their electrical (σ) and thermal conductivity (k).

This work has focused on developing accurate metrologies to unravel the physics of thermal and TE transport in carbon-based nanomaterials. First, we describe the design and construction of a bulk thermal and TE measurement tool that can be used to rapidly characterize *cross-plane* thermal conductivity and Seebeck voltage of *macroscale* materials. We discuss the sample limitations for using a one-dimensional (1D) steady-state thermal conductivity measurement technique. We show the use of this tool to study the thermal performance of polymer-embedded, vertical Cu nanowire arrays for use as a thermal interface material. We also show the use of this tool to simultaneously measure the thermal conductivity and Seebeck coefficient of bulk materials to help determine optimum compositions for material synthesis and fabrication studies.

Next, we discuss a suspended infrared microscopy-based technique that is designed to measure the *in-plane* thermal conductivity of suspended thin films. We utilize this method to characterize thermal transport in chirality-sorted single-walled carbon nanotube (SWNT) networks which are ~400 nm thick. We uncover the importance of SWNT junction and mass density to thermal transport in SWNT networks. These

networks display high thermal conductivities comparable to those of the best metals (~370 W/m/K), despite having order-of-magnitude lower mass densities (~1 g/cm^3).

Finally, we describe the design and fabrication of an on-chip thermometry platform used to measure TE properties of sub-10 nm thin films. We present a comprehensive study of the effect of temperature and doping (both n- and p-type) on the TE properties of ultra-pure (> 99.9 %) semiconducting SWNT (s-SWNT) networks. We demonstrate the highest electron and hole Seebeck coefficients for polymer-free s-SWNT networks, over the 80 to 600 K temperature range (up to ~600 μV/K, or more than double that of conventional bulk TE materials like Bi_2Te_3). We develop a compact theoretical model that uncovers the physics of electron and phonon transport between SWNTs, evaluating the relative contributions of 1D tubes versus the zero-dimensional (0D) SWNT junctions to the TE properties of the network. Using the metrologies designed and built in this thesis, we are able to comprehensively study nano- to macroscale materials for thermal and TE applications.

To my family

Acknowledgements

I would like to thank my advisor, Prof. Eric Pop. I am extremely grateful for the opportunity to work in your lab. I learned many invaluable skills. I would like to thank Prof. Zhenan Bao for support and involvement in all our collaborations. I would like thank Prof. Kenneth Goodson for the support throughout my years at Stanford. I would like to thank Prof. Yoshio Nishi, Prof. Xiaolin Zheng, and Prof. H.-S. Philip Wong for serving on my dissertation defense and reading committees. I would like to acknowledge Dr. Vincent Gambin and Northrop Grumman for supporting me in the last few years of my PhD.

To my lab mates, you guys made this journey much more enjoyable. I would like to acknowledge David Estrada for mentoring me all these years. Your wisdom has helped me through so much. I would like to acknowledge Zuanyi Li, Sharnali Islam, Albert Liao, Vincent Dorgan, Enrique Carrion, Joshua Wood, Zhun-Yong Ong, Kyle Grosse, Ashkan Behnam, and Myung-ho Bae, from our group at University of Illinois at Urbana-Champaign (UIUC).

To the Pop group at Stanford, I really enjoyed my time with you guys. I would like to acknowledge Chris English and Ning Wang for all their help with moving our lab and my stuff across the country. To my cubicle pals, Alex Gabourie and Connor McClellan, thanks for keeping it lively in the office. To Saurabh Suryavanshi, Sanchit Deshmukh, Juan Pablo Llinás, Chris Neumann, Michelle Chen, Victoria Chen, Connor Bailey, Isha Datye, Michal Mleczko, Lily Xu, Rachel Luo, and Stephanie Bohaichuk, it has been a pleasure working together and hanging out with you guys. To the Goodson group, thank you guys for sharing your lab with me. I would like to acknowledge my collaborators in the Bao group especially Ting Lei. I really enjoyed our projects together. To the Wong group, thank you guys for your eagerness to help with challenges

and collaborate. To Michael Barako, thank you for your help and support as I worked through these last few years. To Aditya Sood, you are one of my closest collaborators and friends. Thank you for sharing in this journey with me. To Aparajita Sood, I am so thankful for your cheerfulness and love of yoga, puppies, and going to Korean spa.

To my parents, you taught me that there is always room for improvement. Going forward in my life, I will continue to strive for the best. To Daniel and Jessica, your love and support has meant so much. To all my friends and family, this journey would not be the same without you. To Bo, thank you for your unconditional love. To my husband, Nansi Xue, you spoil me so much. Thank you for everything, and I look forward to the next part of our life together.

Table of Contents

List of Tables

List of Figures

Chapter 1
Introduction

This chapter introduces the use of carbon-based thermoelectrics for energy harvesting applications. We also discuss various thermal metrologies necessary to study materials on different length-scales from fundamental physics to application-based parameters.

1.1 Towards Wearable Computing

With the advent of the Internet of Things, there are more and more forms of wearable computing on the market. As components of computer processors continue to scale, we can fit computing power in smaller form factors. Figure 1.1 illustrates the evolution of wearable forms of computing over the years. However, one of the factors that limits wearable computing performance and capabilities is the battery performance. Current batteries are utilizing lithium ion technology first commercialized in 1991, with energy densities increasing at a rate of about ~5-8% every year.[1] To get around the battery technology limitations, product designers have resorted to improving charging speeds, circuit power consumption, and software power management. In 2017, the state of the art Apple Watch 3 consumes ~60 mW of power (on average) and can be used 4-20 hours depending on the enabled functions (cellular data, GPS tracking or music playback).

These challenges bring us to an interesting question; *can we harvest energy from humans?* Humans generate varying amounts of power depending on the activity. In 1996, Starner calculated human energy expenditures dependent on different activities by using the number of kilocalories/hour consumed by the body as the metric.[2] Someone who is hiking at 4 miles per hour expends about 350 kCal/hr or 407 Watts which would be expended in the form of thermal and mechanical energy. However, a study published in 2008 that measured how much Americans spent in sedentary behaviors (sitting,

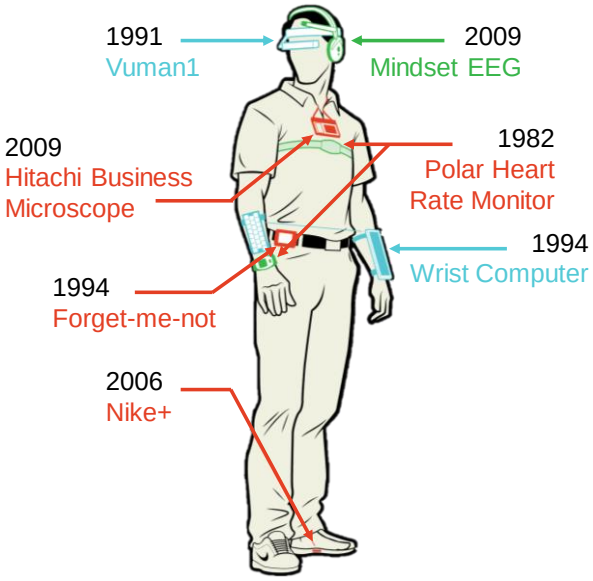

Figure 1.1. Wearable computing technologies timeline adapted from Harvard Business Review.[3]

reclining, lying down) found that the average adult spends about 60% of their waking hours in sedentary activities.[4] While sitting, the human expends about 100 kCal of energy (116 Watts).[2] Most of this energy will be from heat, therefore thermal energy harvesting would be the best choice for the average wearable electronic user. Table 1.1 shows a comparison of various energy scavenging technologies and the amount of power that can be potentially generated adapted from Spansion-Cypress Semiconductor. The upper efficiency limit of thermal energy harvest is given by the Carnot efficiency:

$$\eta_{Carnot} = \frac{T_H - T_C}{T_H} = \frac{T_{body} - T_{ambient}}{T_{body}} = \frac{310\ \text{K} - 293\ \text{K}}{310\ \text{K}} \qquad (1.1)$$

where T_{body} and T_{ambient} are the temperatures of human skin surface and ambient environment (which correspond to T_{H} and T_{C}, the hot and cold temperatures) respectively. For the expression above, we find that the maximum efficiency is only

Energy Source	Harvester	Generated Power	Output Voltage	Environment of power generation
Light/Sun	Solar Cell	10 mW/cm^2	> DC 0.7 V (1 cell)	Outdoor (daytime)
		30 μW/cm^2		Indoor (Office)
Vibration	Piezoelectric Device	500 μW/cm^2	> AC 80 V (Open)	Mechanical Vibration (Compressor vibration @ 30 Hz)
		10 μW/cm^2		Human action – button pressing
Temperature	Thermoelectric Generator	0.5 W/cm^2	0 V to several V depending on material	Temperature difference: 100 ˚C

Table 1.1. Table of energy sources, energy harvesting technologies, amount of generated power, output voltages, and environment of use adapted from Spansion-Cypress Semiconductor.[5]

about 5.5%. If we assume 25% of the heat is already lost to sweating,[2] the maximum thermal energy that can be captured from a human is ~5 W (0.25 mW/cm^2). An existing technology that would be suitable for harvesting thermal energy is thermoelectrics (TEs). Thermoelectric generators (TEGs) are solid state devices that convert temperature gradients into voltages. TEGs require an n- and p-type semiconductor and have no moving parts. Figure 1.2a shows a typical TEG. Currently, most TEGs are used in space exploration such as Voyager,[6] and most recently the Mars Curiosity Rover, which has a TEG powered by the heat of a radioactively decaying Pu-238 isotope.[7] However, the current technology is too inefficient for harvesting energy on Earth, because of the large temperature gradients required.[8]

Unfortunately, at ~1% efficiency near room temperature, we can only harvest about 5 μW/cm^2 from the human body using TEGs. This technology was implemented into watches (which use about 5 – 20 μW of power) in 1998, in the Seiko Thermic watch,

which only used ~1 μW of power from wrist heat.[9] However, modern smart watches such as the Apple Watch 3 require tens of milliwatts of power. TEGs are currently too inefficient and expensive to be considered for wearable consumer electronics. Therefore, to engineer more efficient TEs, we must first understand TE transport on a fundamental level.

1.2 Thermal and Thermoelectric Transport

1.2.1 Thermoelectric Transport

TE transport relies on the Seebeck effect which is the diffusion of charge carriers (electrons or holes) in the presence of a temperature gradient (illustrated in Figure 1.2). This effect was first discovered in 1821 when Thomas Johann Seebeck discovered that a heated junction of two different metals would deflect a magnet.[10] In 1834, Jean Charles Peltier discovered that when current flowed through the junction of two conductors, there was a heating or cooling effect depending on the direction of current flow. These two phenomena are now known as the Seebeck and Peltier effects, which are both aspects of TE transport. The Seebeck coefficient of a material is the electrical potential that can be established in the presence of a temperature gradient:

$$S = -\frac{\Delta V}{\Delta T} = -\frac{V_H - V_C}{T_H - T_C} \tag{1.2}$$

where S is the Seebeck coefficient, ΔV is the potential difference, and ΔT is the temperature gradient (between the hot side, T_H, and the cold side, T_C). In an n-type semiconductor, where there is an excess of electrons, the temperature gradient will lead to the diffusion of electrons towards the cold end of the semiconductor (for p-type semiconductors, holes will diffuse to the cold end) as illustrated in Figure 1.2a. For a single thermoelectric material, the generated voltage is on the order of hundreds of microvolts for every Kelvin temperature difference. For usable power, n- and p-type semiconductors can be connected electrically in series (such that the voltages add up) while thermally in parallel (Figure 1.2b).

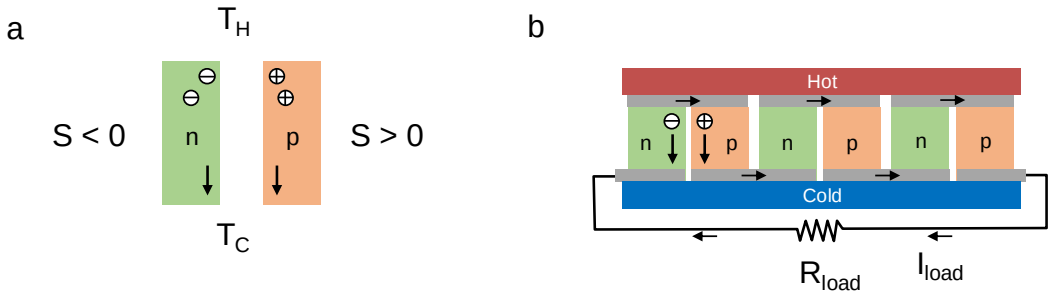

Figure 1.2. (a) Illustration of the Seebeck effect in n- (green) and p-type (orange) semiconductors. The hot end (T_H) causes electrons (or holes) to diffuse to the cold end (T_C). For an n-type semiconductor, the voltage established at the cold end is negative, therefore the Seebeck coefficient have a negative sign ($S < 0$). (b) Thermoelectric generator where the n- and p- semiconductors are connected electrically in series (to increase output voltage) and thermally in parallel.

A TEG behaves as a power source in the presence of a constant temperature gradient, although the internal resistance of the TEG limits current output. In contrast, TEGs can be used as coolers due to the Peltier effect, where the flow of current results in cooling at the junctions. TEGs have been extremely useful for space explorations where solar power is not always a reliable source of energy, especially for deep space missions. Since TEGs are solid-state devices, there are no moving parts; making them reliable for long periods of time.

Equation 1.2 gives us a general idea of how to measure the Seebeck coefficient of a material, however understanding the microscopic origins of thermoelectric transport will elucidate how to tune materials for energy harvesting. The Seebeck effect exists because charge carriers (such as electrons or holes) also carry heat. Using the Boltzmann transport equation (BTE) under the Relaxation Time Approximation (RTA) and assuming small deviations from equilibrium, we can describe electrical conductivity in the form of integrals over electron energy:[11]

$$\sigma = \int \sigma(E)\left(-\frac{\partial f}{\partial E}\right)dE \tag{1.3}$$

where ($-\partial f / \partial E$) is the Fermi window factor, and $\sigma(E)$ is the differential conductivity which represents the contributions to conductivity from electrons with energy (E). The differential conductivity is given as:

$$\sigma(E) \approx q^2 \tau(E) \overline{v}_x^2(E) D(E) \tag{1.4}$$

where q is the elementary charge, τ is the relaxation time, v_x is the carrier velocity, and D is the density of states (DOS). The Fermi window (shown in Figure 1.3a) which is centered around the Fermi energy (E_F) with a width of ~ $k_B T$, describes the energy of electrons that contribute to conduction. Here k_B is the Boltzmann constant and T is the temperature. Only electrons close to the Fermi surface can conduct to empty states above the Fermi level. The Seebeck coefficient is therefore expressed as:

$$S \equiv \frac{k_B}{q} \frac{\int \sigma(E) \frac{E - E_F}{k_B T} \left(-\frac{\partial f}{\partial E} \right) dE}{\int \sigma(E) \left(-\frac{\partial f}{\partial E} \right) dE} \ . \tag{1.5}$$

From Equation 1.5, we can see that the Seebeck coefficient is enhanced when there is a large asymmetry in the DOS around E_F. This suggests that low-dimensional materials such as 1D (nanotubes or nanowires) and 0D (fullerenes or nanotube junctions) would have large Seebeck coefficients.[12] However, low-dimensional materials (such as single nanowires) cannot be made into a TEG. Therefore, we will need to understand how low-dimensional materials behave thermoelectrically in a composite.

1.2.2 Thermoelectric Figure of Merit (ZT)

An ideal thermoelectric material should have: (1) high electrical conductivity (σ) to reduce self-heating in the presence of current flow, (2) low thermal conductivity (k) to maintain temperature gradients, and (3) high Seebeck coefficient to generate large voltages. In 1949, Abram Ioffe introduced the figure of merit (ZT) to help researchers optimize the TE performance of a material:

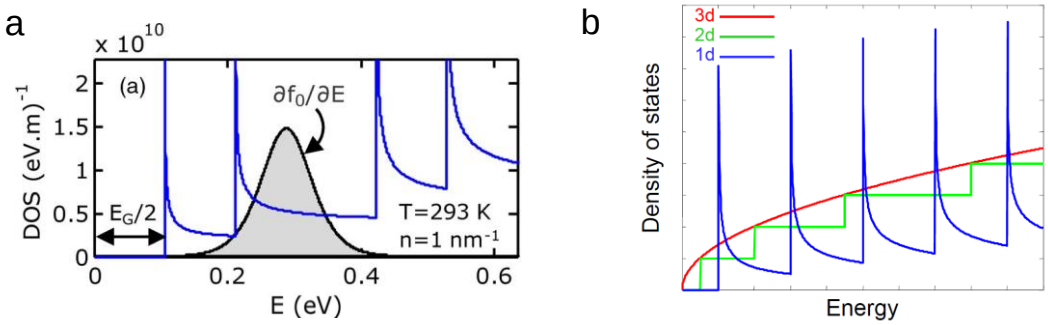

Figure 1.3. (a) Fermi window factor (gray region) and density of states (DOS) for a semiconducting SWNT as a function of electron energy (E). E_G is the band gap and f_0 is the equilibrium Fermi-Dirac distribution. Figure reproduced after Ref. 14. (b) Density of states in 3D, 2D, and 1D shows increasingly sharp features and asymmetry if the Fermi level is positioned near such a sharp feature.[15]

$$ZT = \frac{S^2\sigma}{k}T \tag{1.6}$$

where S is the Seebeck coefficient, σ and k are the electrical and thermal conductivity respectively, and T is the temperature. With a figure of merit, we can define an efficiency that is a scaled form of the Carnot efficiency:[13]

$$\eta_{TEG} = \frac{\Delta T}{T_H}\frac{\sqrt{1+ZT}-1}{\sqrt{1+ZT}+\frac{T_C}{T_H}} \tag{1.7}$$

where $\Delta T = T_H - T_C$. Based on Equation 1.7, we can see that the ZT of a thermoelectric would have to be infinite to reach the Carnot efficiency. Conventional bulk thermoelectrics[13] have $ZT \sim 1$ which means for that low temperature gradients (such as human skin to ambient), the efficiency is only about 1%.

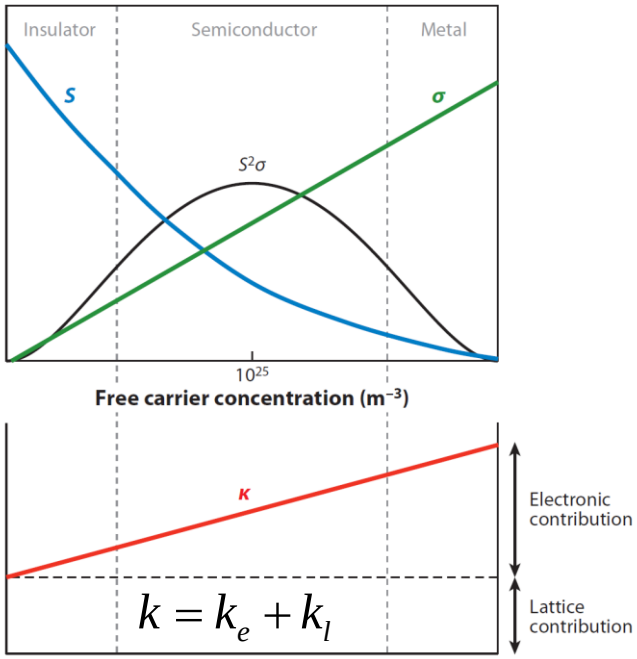

Figure 1.4. Seebeck coefficient, electrical and thermal conductivity dependence on carrier doping. As carrier concentrations increase, the Seebeck coefficient decreases which means there is an optimum carrier concentration for the power factor of a thermoelectric material. The thermal conductivity has an electronic component (k_e) that depends on carrier concentration. Figure reproduced after Ref. 11.

Understanding the individual components of *ZT* will help us fine tune materials for better efficiency. The numerator of Equation 1.6 is also known as the power factor ($S^2\sigma$). Figure 1.4 shows the tradeoffs between the factors in the figure of merit. Increasing the carrier concentration (through doping or electrostatically) will often decrease the Seebeck coefficient of a material. This concept was illustrated in Equation 1.5 where we saw that there needs to be DOS asymmetry near the Fermi level. Therefore, highly doped semiconductors or metals have poor Seebeck coefficient due to the Fermi level shifting deep into the conduction band. Furthermore, the increase in carriers in a semiconductor would also lead to increases in the thermal conductivity due to the Wiedemann-Franz law (WFL) which will be described in the next section. These trade-

offs have created a challenge for researchers in pursuit of the most efficient thermoelectric materials.

State of the art thermoelectrics are generally narrow band gap semiconductors with heavy atoms such as Bi_2Te_3 and PbTe.[13] When doped, these materials have good electrical conductivity (σ_{Bi2Te3} ~ 500 S/cm at room temperature[16]), and due to the heavy atoms in the crystal, the thermal conductivity is almost two orders of magnitude lower than that of undoped Si (k_{Bi2Te3} ~ 1.4 W/m/K vs. k_{Si} ~ 140 W/m/K at room temperature[17,18]). Efforts to optimize *ZT* have focused on two main avenues: reducing lattice thermal conductivities and optimizing power factor through carrier doping. With the development of nanofabrication techniques, we have more and more options for improving material *ZT*s.

1.2.3 Thermal Conduction in Nanomaterials

Understanding nanoscale thermal transport has become increasingly important as we develop ways to engineer novel nanomaterials and devices. As the length scales of these materials become comparable to the mean free paths (MFP) of different energy carriers (i.e. 10 nm to 1 μm near room temperature), it becomes crucial to fundamentally understand carrier interactions. The focus of this thesis will be on nano- and micro- scale heat conduction metrology, spanning multiple length scales, directions, and materials.

In a crystal, lattice vibrations, or phonons, play a large role in heat conduction. In conductors such as metals, mainly electrons carry heat. The electronic thermal conductivity can be related to the electrical conductivity by the WFL:

$$k_e = \sigma L T \tag{1.8}$$

where σ is the electrical conductivity, L is the Lorenz number, and T is the temperature. L is approximately the same (~ 2.45×10^{-8} WΩ/K^2) for most metals.[19] In heavily doped semiconductors the WFL is often used to calculate the electron thermal conductivity. Compared to electrical conductivities which span over twenty orders of magnitude from insulators to conductors, the thermal conductivities of materials on span only about five

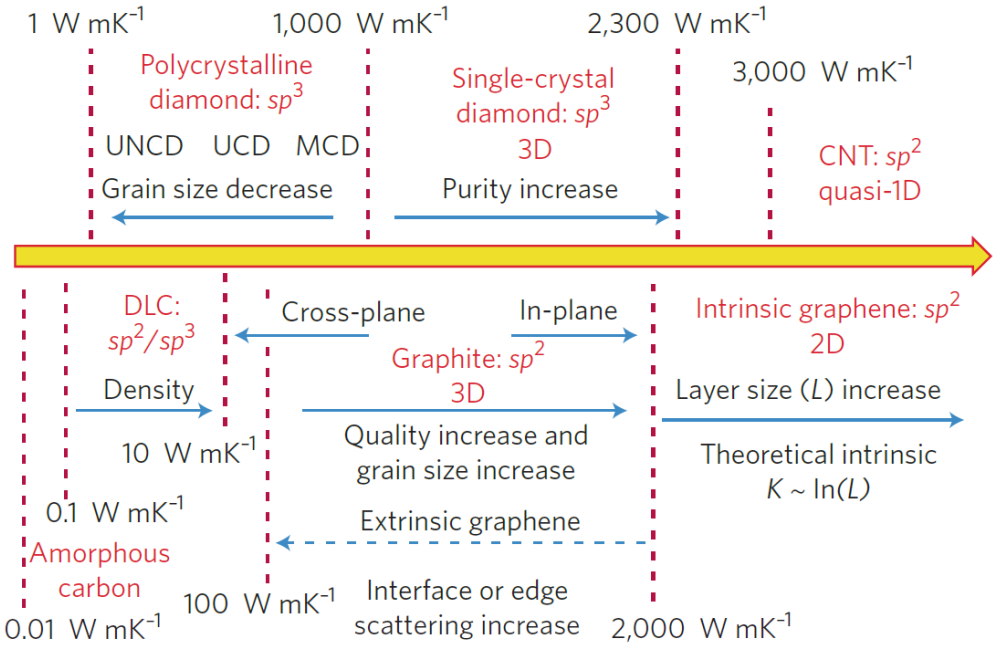

Figure 1.5. Thermal conductivities of allotropes of carbon capturing the range of thermal conductivities of materials in general. In polycrystalline diamond, thermal conductivities can by tuned by the grain size from ultrananocrystalline (UNCD) to nanocrystalline (NCD), and microcrystalline (MCD). The presence of sp^3 in amorphous carbon creates a diamond-like carbon (DLC) which has higher thermal conductivity than amorphous carbon alone due to the presence of these bonds. Figure reproduced from Ref. 20.

orders of magnitude (shown in Figure 1.5). This range can be seen among carbon allotropes. Diamond, graphene and carbon nanotubes have thermal conductivities reaching 3000 W/m/K, whereas amorphous carbon has a thermal conductivity of about 0.1 W/m/K (at room temperature).

For many 3D crystalline materials, top-down nanostructuring methods can be used to tune the thermal conductivity. One prime example is with Si, in which researchers etched bulk, single crystal Si into rough nanowires and were able to reduce the thermal conductivity by nearly two orders of magnitude (k_{SiNW} ~ 1 to 8 W/m/K) at room temperature.[21,22] Since the phonon MPF is much longer than the electron MFP, the

electrical conductivity was not greatly reduced, resulting in a *ZT* that was two orders of magnitude higher (ZT_{SiNW} ~ 0.6) than that of bulk Si.[21]

1.3 Carbon-Based Thermoelectrics

Most conventional thermoelectrics are based on bismuth, tellurium, lead, and antimony. According to the US Geological Survey, these are considered rare minerals and are some of the rarest materials based on relative abundance to Si shown in Figure 1.6.[23] Therefore, a carbon-based thermoelectric could drive down costs, due to the relative abundance of carbon. This section introduces the use of carbon nanotubes (CNTs), leveraging their unique properties for thermoelectric applications.

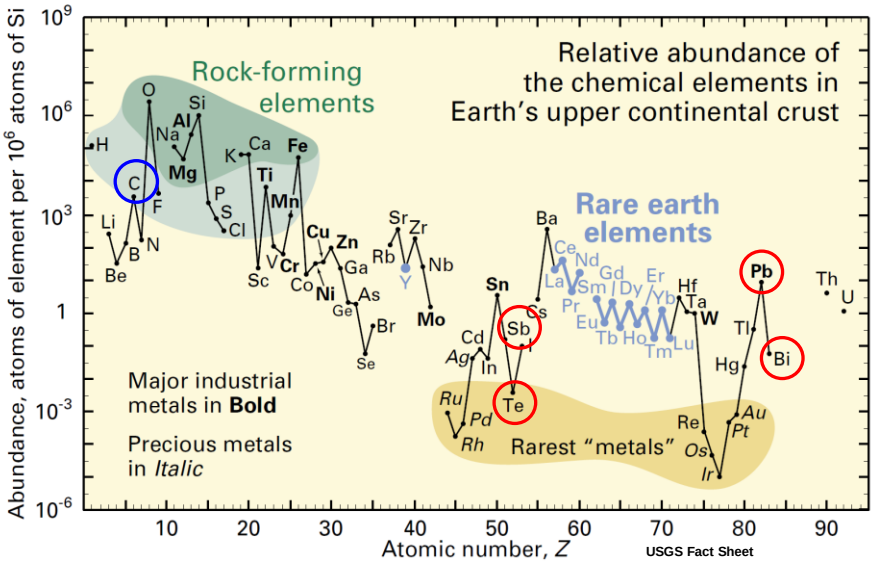

Figure 1.6. Relative abundance of elements compared to Si adapted from Ref. 23. Common thermoelectric materials are circled in red and carbon is in blue. Tellurium is commonly used in low temperature thermoelectric applications and is particularly rare.

CNTs are cylindrical 1D structures effectively made from a rolled-up sheet of sp^2-bonded carbon atoms (graphene) as shown in Figure 1.7.[24,25] CNTs are either single

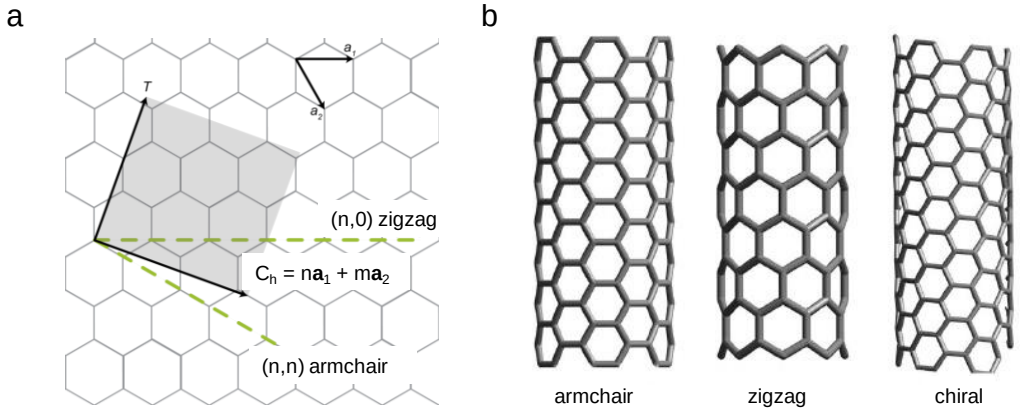

Figure 1.7. (a) Schematic of graphene adapted from Ref. 24 and (b) different chiralities of SWNTs. Armchair SWNTs are (*n*,*n*), Zig-zag SWNTs are (*0*,*m*), and the rest are called chiral nanotubes. Depending on chiral vector, the nanotube will either be metallic or semiconducting. Figure reproduced from Ref. 25.

walled (SWNT) or multiwalled (MWNT) and have diameters ranging from a sub-nanometer to hundreds of nanometers. Typical SWNT diameters range from ~0.6 nm to ~4.0 nm. SWNTs are of interest for electronic applications since SWNTs can be semiconducting depending on how they are rolled.

SWNTs are identified by a chiral vector (*n*,*m*) which can be used to describe the circumference of the SWNT ($C = n\mathbf{a}_1 + m\mathbf{a}_2$ where $\mathbf{a}_1$ and $\mathbf{a}_2$ are unit vectors of the hexagonal carbon lattice).[24] Graphene is a semimetal with no band gap, whereas SWNTs have a band gap depending on the chirality. The approximate band gap of a semiconducting SWNT is given by ~0.82/*d* (in eV),[14,26] where *d* is the diameter in nm. SWNTs can be synthesized using methods such as arc discharge, laser ablation, or chemical vapor deposition.[27] The ratio of metallic to semiconducting tubes is 1:2 by most synthesis methods.[28] Within electronics, metallic SWNTs are useful for interconnects, but they present a problem for transistors, which must be semiconducting. Therefore, sorting SWNTs by chirality or electronic type is an area of research that is of great importance for many applications which will be discussed in Section 4.3.1.

1.4 Hierarchy of Measurement Metrologies

Unlike electrical current or voltage, there are no direct ways to measure heat flow or temperature. All methods of measuring temperature rely on the use of a phenomenon that has a measurable property which changes with temperature. A simple one-dimensional Fourier law of heat conduction (Equation 1.9) gives a general idea of the parameters that need to be measured to extract material thermal conductivities.

$$Q = -k\nabla T \tag{1.9}$$

where Q is the heat flux per unit area, k is the thermal conductivity of the material, and T is the temperature. To measure thermal conductivities, we need to know the heat flux (or input power) and the temperature change across the sample. For large samples, we can use thermocouples to read temperatures on two ends of the sample, but for microscopic sample, this presents many challenges.

We can break down thermal metrologies into two general categories, probe-based and electrical methods. Figure 1.8 shows a few examples of techniques for thermal and thermoelectric measurements. There are many trade-offs between using the different techniques. Often, a complex measurement set-up such as the probe-based methods can measure easily fabricated samples. On the other hand, complex on-chip thermal platforms which require careful metal heater and thermometer designs can be used with simple multimeters and power supplies to measure thermal transport.

Figure 1.8a. shows a thermoreflectance measurement schematic. In this technique, a reflective metal (e.g. Al or Au) is used as the thermometer because the metal reflectance changes with the metal temperature, as heat dissipates from the surface. In a pump-probe version of this technique, a pump laser heats the metal surface at high frequencies and a probe laser is used to measure the changes in reflectance of the metal surface.[29] Since the laser power is known, the time-dependent temperature decay can be used to calculate the thermal conductance of the sample. However, because there is the additional metal interface with the surface of the sample, care must be taken to properly extract the thermal properties. Thermoreflectance measurements are ideal for measuring

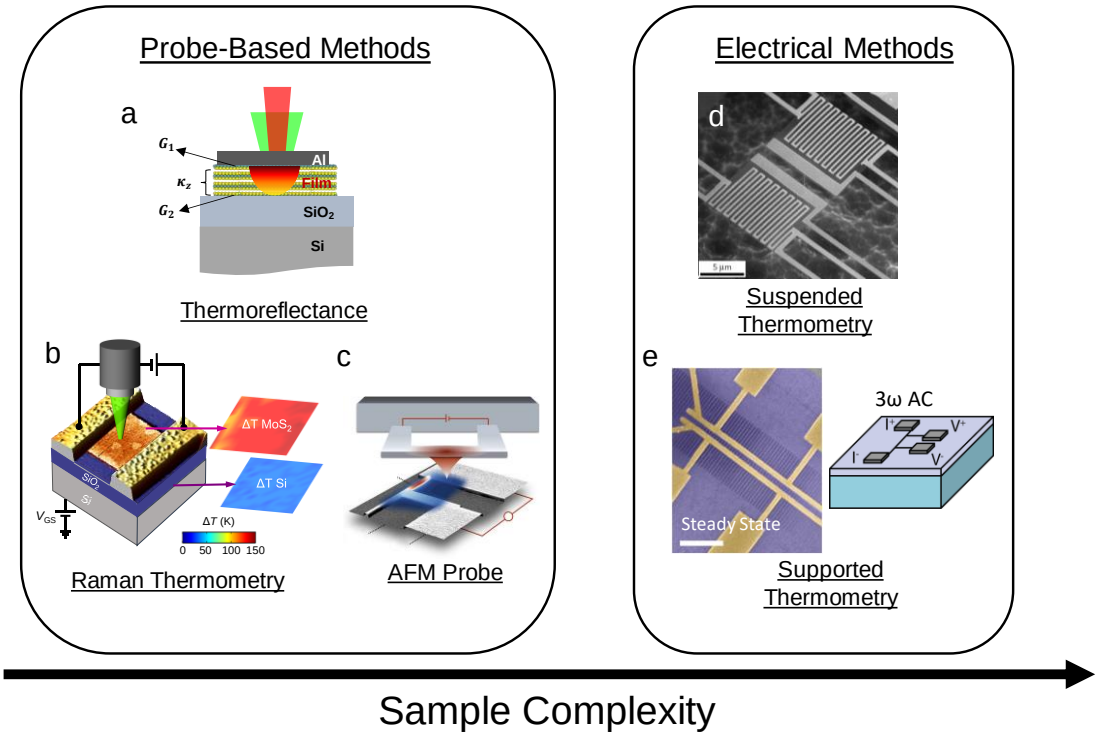

Figure 1.8. Thermal and thermoelectric measurement methods. (a) Thermoreflectance uses a laser to probe temperature changes in the cross-plane direction through changes in metal reflectance.[29] (b) Raman thermometry uses spectroscopic shifts to calculate temperature changes.[30] (c) AFM probe thermometry measures changes in temperature using AFM probe tip.[31] (d) Suspended electrical thermometry platform utilizes 1D heat conduction in the lateral direction to measure thermal properties.[32] (e) Supported thermometry can use steady-state and AC methods to probe lateral and cross-plane heat flow.[33-35]

planar samples, but the laser wavelengths can be quite large which makes the spatial resolution of this method generally on the order of ~5 – 10 μm.

Figure 1.8b depicts a Raman thermometry measurement set-up. Raman spectroscopy measures the inelastic scattering of single energy photons with lattice vibrations.[36] Generally, the Raman technique can also be used to identify materials due to their unique spectrum. As sample temperatures change, the phonon-phonon

interactions will change, resulting in peak shifts which can be calibrated to temperatures. Raman thermometry can be used to probe temperatures in samples that are self-heated or heated with the Raman laser itself. Because Raman peaks are unique to materials, it can be used to probe temperatures in encapsulated materials as well as heterostructures of many materials. However, one of the major trade-offs of this technique is that the Raman peak shifts with temperature are generally very small. In addition, most Raman systems have spectral resolutions of about 1 cm^{-1}. This results in large uncertainties for temperature measurements. Raman thermometry spatial resolution is also diffraction limited and is usually ~400 to 500 nm depending on the excitation laser wavelength. Finally, if the material of interest has no Raman signal for a given laser wavelength (metals or amorphous materials), then this technique cannot be used for thermometry.

Finally, there are many AFM-probe based methods to measure temperature changes with nanoscale spatial resolution.[31,37] In passive mode scanning thermal microscopy (SThM), a resistive probe such as a Wollaston wire probe is scanned over the sample surface while a small current is used to measure the probe tip resistance. As the tip scans over regions of sample heating, the resistance of the tip will change due to the thermal interaction between the surface and the tip. The resistance change can be correlated to temperature rise after careful calibration.[31] Alternatively, in scanning Joule expansion microscopy (SJEM), a polymer with a large coefficient of thermal expansion is used to coat a sample surface. As the sample heats through Joule heating, a probe in contact with the surface can measure the temperature changes by probing the mechanical expansion of the polymer.[37] Since probe tip diameters can be ~20 nm, the spatial resolution of these measurements is also tens of nanometers. However, sample topology such as sharp changes in height can affect measurement results, therefore extra care must be taken when interpreting nonplanar features.[38]

Electrical methods can be broken down into two main categories, suspended and supported thermometry. Electrical thermometry methods rely on changes in electrical resistance with temperature to measure thermal properties. Generally, a more complex platform will result in a more straightforward analysis due to less unknown sources of

heat loss.[39] Electrically-based thermal measurements are usually done under vacuum which means the main source of parasitic heat loss is through conduction. In a suspended thermal platform (Figure 1.8d),[21,32] the sample will be suspended across two metal thermometers that can heat and measure temperature changes. Since the sample is not in contact with any substrate, there is no additional heat loss into the substrate that needs to be considered. On the other hand, a supported platform[33,34] (Figure 1.8e) would require additional finite element modeling to extract thermal conductivities since the substrate (often a silicon wafer) is a massive heat sink compared to the nanomaterial that is being measured. The large heat sinking substrate can be helpful for cross-plane thermal measurements in methods such as the 3ω method.[35,40] Electrical methods do not require highly specialized measurement equipment, but the sample calibration and sensitivities are very important. Compared to probe-based methods, electrical methods cannot measure spatially varying changes in temperatures or thermal conductivities.

Each measurement method has its advantages and disadvantages. Therefore, understanding how to select proper metrology is extremely important for studying material thermal and thermoelectric properties.

1.5 Organization and Scope of Work

Chapter 1 motivated the need to study thermal and thermoelectric transport in carbon-based nanomaterials as well as the different thermal metrologies that can be used. This thesis will highlight three different measurement techniques applied to different material systems. Figure 1.9 shows the tradeoff between measurement methods and physical understanding. This thesis focuses on the construction and utilization of three different thermal and thermoelectric metrologies to study material transport from fundamental to applied device physics.

Chapter 2 discusses the design and construction of a 1D steady-state thermal measurement tool (Figure 1.9). We design and build a tool to rapidly characterize macroscopic samples. We use it to decouple thermal contributions from interfaces in a Cu nanowire-based thermal interface material.

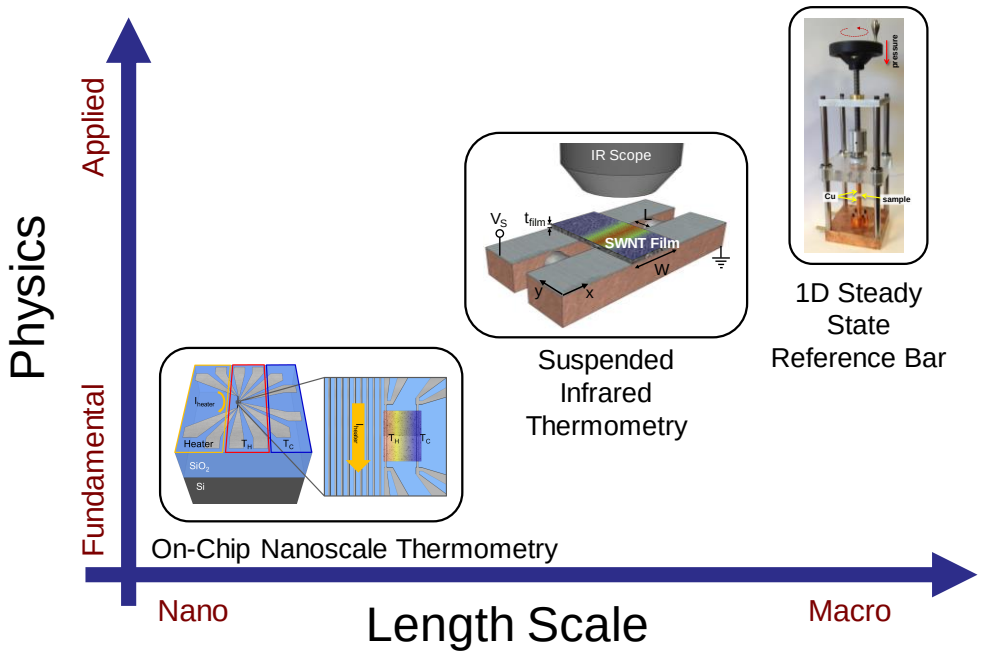

Figure 1.9. Trade-offs between different measurement methods. Different length scales of materials require unique measurement set-ups to study the transport physics. Nanoscale thermometry methods can be used to study fundamental physics in materials, whereas a macroscopic bulk measurement would be used to extract material properties useful for applied physics.

Chapter 3 examines thermal transport in chirality-sorted CNT networks. To accomplish this, we design and build a suspended infrared thermometry technique (also shown in Figure 1.9). We discover that thermal conductivities in CNT networks are highly tunable and mainly dependent on mass and CNT junction densities. The samples measured turn out to have thermal conductivities on the order of metals while having 10x lower mass density.

Chapter 4 discusses the fundamental thermoelectric transport in sorted semiconducting SWNT networks. We design and build an on-chip nanoscale thermometry platform as shown in Figure 1.9 to measure ultra-high purity networks. We measure record high Seebeck coefficients and study the fundamental thermoelectric

and electrical transport in these networks over a temperature range of 80 – 600 K. We uncover that junctions in thermoelectrics are beneficial and can be leveraged to design high performance CNT-based thermoelectrics.

Chapter 5 summarizes the main contributions of this thesis and places the results in a greater context. We discuss the limitations of TE harvesting technologies for power generation and the use of flexible, low cost CNT-based thermoelectrics for niche applications.

Chapter 2
One-Dimensional Steady State Thermometry

This chapter presents a one-dimensional (1D) steady state thermometry platform built to rapidly characterize bulk samples that range from hundreds of microns up to millimeters thick. This section will discuss measurement technique, sample limitations, and applications of this tool.

2.1 Bulk Thermal Conductivity Measurements

For macroscopic samples, we can use a standardized method to measure thermal conductivity. Commercially available systems are built following the ASTM International standard. The ASTM D-5470 is the test standard for measuring thermal properties of a variety of materials ranging from liquids to solids.[41] This measurement method is a one-dimensional, steady-state measurement method which means it cannot measure spatial variations in thermal conductivity or material heat capacity. The advantage of this technique is that it can rapidly characterize thermal conductivities of samples, making it useful for material property optimization. In this chapter, we explore different applications and limitations of this tool.

One common commercial application of this measurement set up is to measure thermal interface materials (TIMs). Typically, the thermal interface between two macroscopic surfaces has poor thermal transmission (large thermal boundary

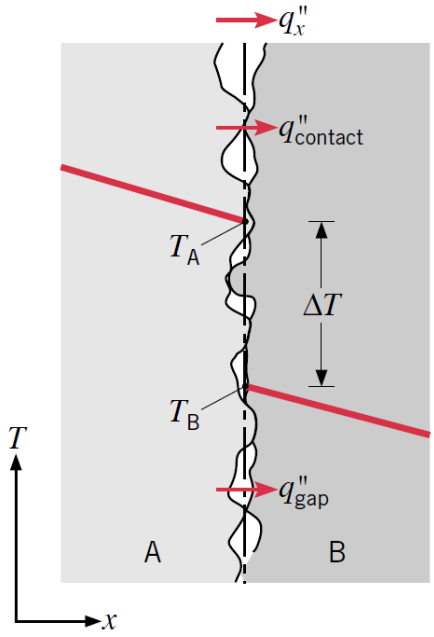

Figure 2.1. Diagram showing the effect of surface roughness on temperature profile (red line) across an interface. Figure reproduced from Ref. 42. Thermal boundary resistance between surfaces in contact generally arises from the roughness and lack of surface conformity. This results in a finite temperature drop at the contacts which is detrimental for heat conduction.

resistances) due to surface non-conformity as shown in Figure 2.1. TIMs are designed to fill in gaps between surfaces to enhance conduction.

In addition, interfacial heat conduction is dependent on the contact pressure of two surfaces. As pressure increases, the surface contact area increases which improves thermal conduction. We discuss later how to extract intrinsic thermal conductivities in these measurements. Figure 2.2 shows a custom-built measurement rig. The sample is placed between two copper blocks and compressed. A heater located in the top contact generates a heat flux that flows down across the sample to the bottom Cu block. The heater in the top contact establishes a temperature gradient along the top Cu contact which is measured using thermocouples placed along the bar. As discussed in Section

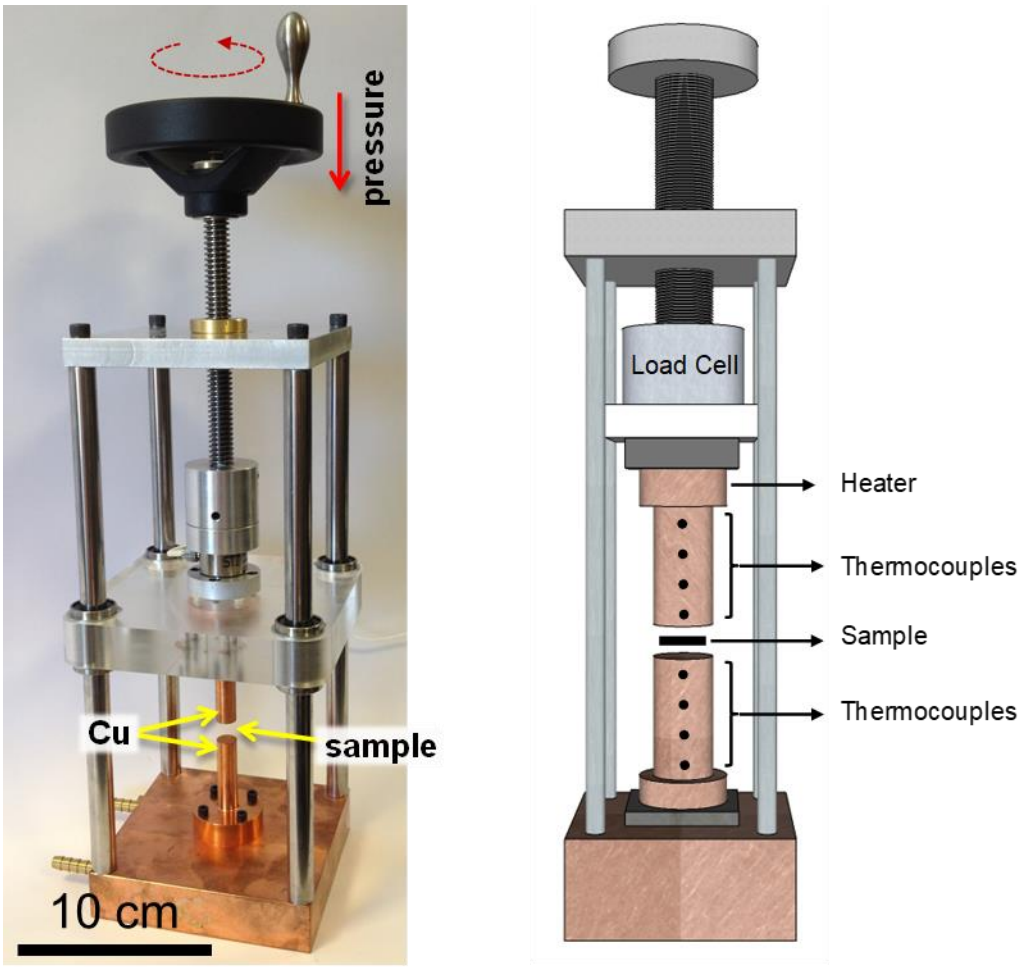

Figure 2.2. Custom-built ASTM thermal conductivity tool and 3D design schematic. Sample is placed between two Cu blocks and compressed while heat is generated at the top meter bar.

1.4, the important factors in measuring thermal conductivity are the input power, thermal conductivity, and temperature gradient. This technique uses an external heat source to apply a heat flux across the sample, allowing us to measure thermal conductance. Later, we will discuss applications for this method.

2.2 Experimental Methodology

2.2.1 1D Steady State Thermal Measurements

The thermal conductivity measurement tool has two reference bars made of copper. The reference bars are 1 cm diameter cylindrical rods with four thermocouple (TC) holes positioned along the rode in equidistant spacing in each rod. The TC closest to the

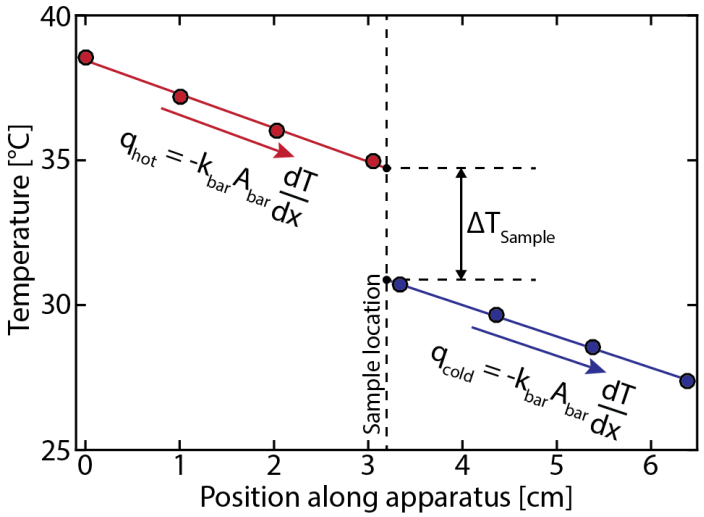

Figure 2.3. Temperature profile along the reference bars. The measured temperatures of the top and bottom reference bars are depicted in red and blue respectively. Figure reproduced from Ref. 43.

sample surface sits at approximately 1.5 mm from the surface of the Cu contact which allows precise measurement of the temperature difference across the sample without significant loss in the Cu contact. We choose Cu for the reference bars due to its high and well-known thermal conductivity. A ceramic cartridge heater inside the upper Cu bar is controlled using a proportional-integral-derivative (PID) controller. The bottom Cu bar is connected to a large Cu block with channels drilled through the block for water cooling. The heater is placed in the upper meter bar such that the heat flow from the top to the bottom contact is due to conduction and not convection. A load cell is placed

above the upper meter bar to measure the pressure applied on the sample. Figure 2.3 shows the linear temperature gradient along the reference bars. The slopes (which is the thermal conductivity) should be identical for both reference bars. Once we know the heat flux, we can apply the same calculation to extracting thermal conductivity from the sample. However, one source of parasitic heat loss is the thermal contact/boundary resistance discussed above.

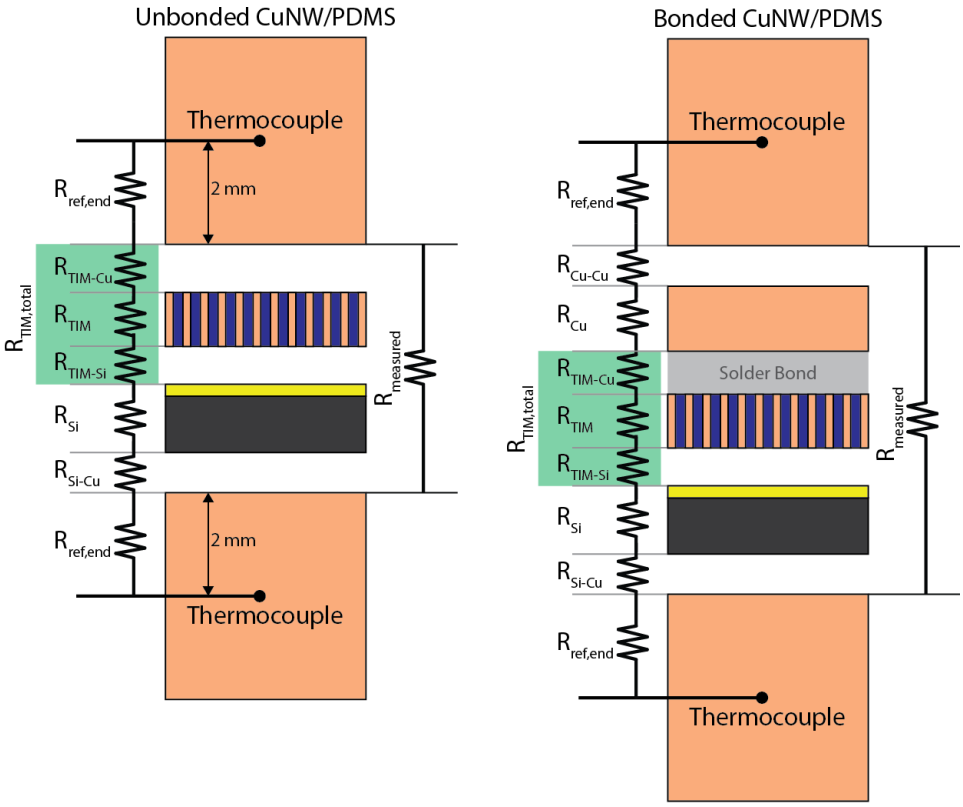

Figure 2.4. Thermal resistance schematic to showcase the complexity of different samples. In this case, the vertically aligned Cu nanowires are directly deposited on a layer of gold on top of a Si substrate. Therefore, there are interfaces between substrate, gold layer, Cu nanowires that are within the lumped resistance measurement. Figure reproduced from Ref. 43.

From Figure 2.4, we can see that the thermal resistance sensed by the measurement is a lumped resistance that includes the sample interfaces as well as the contact resistance between the reference bar and the sample. The intrinsic thermal resistance (R_s) of the sample is:

$$R_s = \frac{t}{kA} \tag{2.1}$$

where t is the sample thickness, k is the sample thermal conductivity, and A is the sample cross-sectional area. However, the presence of many interfaces makes intrinsic thermal conductivity extractions complicated because the tool measures $R_t = R_s + R_c$. (where R_t is the total resistance, R_s is the sample resistance, and R_c is the contact resistance). We can account for R_c using two methods. We can measure samples of various lengths and estimate the thermal contact resistance using a thermal transfer length method (TLM) measurement as shown in Figure 2.5. As the thickness of the sample increases, the thermal resistances will scale linearly assuming a uniform sample thermal conductivity and the same contact resistances.

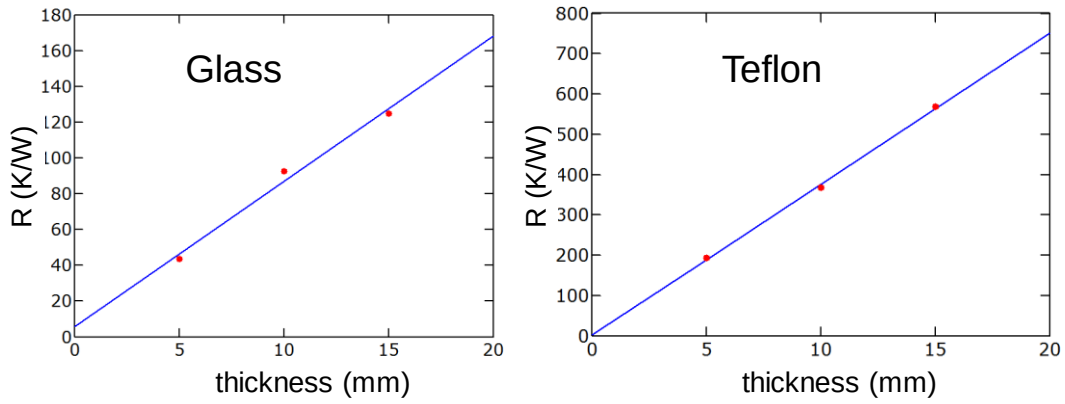

Figure 2.5. Thermal TLM measurement where the linear fit of the resistance vs. thickness of glass and Teflon sample is used to extract thermal conductivities. The contact resistance is extracted from the y-intercept of the linear fit (blue line). The sample thermal conductivity is extract from the slope of the fit.

The contact resistance can be extracted using the y-intercept of a thermal resistance versus sample length linear fit (like an electrical TLM). The y-intercept point, which will be a finite positive value, represents the resistance in the limit of a sample with zero thickness. Once we know the contact resistance, we can calculate the sample thermal conductivity directly using Equation 2.1 or by using the slope of the linear fit which is $1/(kA)$. In most cases we cannot measure many samples of different thickness. Therefore, we must use a pressure-dependent measurement to extract the thermal contact resistance.

The contact pressure plays an important role on thermal contact resistances. Increasing contact pressure (P) will decrease the measured resistance of a sample. Assuming a rigid sample, this will mainly be due to the microscopic increases in contact area at high pressures. This means that we can extract thermal contact contributions by plotting the thermal resistances of a sample versus the inverse of the applied pressure (R vs. $1/P$). In this case, the fit should be linear, and the y-intercept resistance ($R_{\text{y-int}}$) will give the thermal resistance in the limit of infinite pressure (zero contact resistance). The sample thermal conductivity can be extracted from the y-intercept value (using Equation 2.1) since this is the intrinsic sample resistance. It is important to note that sample thickness changes during pressure-dependent measurements will create errors in the thermal conductivity extraction.

It is also important to note that for the thermal TLM measurement, the applied pressure must be very large and around the sample pressure for all the samples. For our measurement rig, we use several materials with known thermal conductivities to test the system for accuracy (shown in Figure 2.5). We measure glass, Teflon and stainless steel that are identical in cross-section to the metal rods. The samples are 5, 10, and 15 mm thick. We extract a thermal conductivity of 1.01 W/m/K for the glass, 0.23 W/m/K for the Teflon, and 16.2 W/m/K for the stainless steel. The error for the calibration samples ranged from ~4 to 8%. In the next section, we will discuss some possible sources for these errors.

2.2.2 Sensitivity and Sample Limitations

There are limitations for sample dimensions for this measurement tool and technique. In this section, we discuss the limitations on sample thickness, which is dependent on the sample thermal conductivity. The first scenario is for samples that are thermally resistive such as aerogels which ultra-porous (~97% air). In this case, there is a maximum thickness for the sample before losses from the sides of the sample become significant. A sample that is resistive and thick will have such a large thermal resistance that conduction through the sample cannot be measurable by the tool. Figure 2.6a presents the thermal circuit that illustrates the heat loss mechanisms at play. We assume that the temperature of the cold contact (T_C) is the temperature of the ambient environment (T_0). We set a percentage heat loss that we are willing to tolerate as ϵ. The thermal resistances for conduction would need to balance with radiation and convection in the following equation:

$$\epsilon \frac{R_{conv} R_{rad}}{R_{conv} + R_{rad}} = R_{cond} \tag{2.2}$$

where R_{rad} and R_{conv} are the thermal resistances due to radiation and convection respectively. The thermal boundary/contact resistance (R_{TBR}) is ignored in this case since the sample thermal resistance is much greater. The final expression for maximum sample thickness is:

$$t_{max} = \sqrt{\frac{\epsilon k_{sample} WL}{2(W+L)\left(h_{conv} + 4\sigma_B \varepsilon T_0^3\right)}} \tag{2.3}$$

where k_{sample}, W, and L are the thermal conductivity, width, and length of the sample respectively. The expression includes the convective heat loss (h_{conv}) and radiative heat loss ($4\sigma_B \varepsilon T_0^3$) contributions as well. Figure 2.6b shows the range of thicknesses that are measurable by the tool. The upper and lower bound of the ranges are 10 and 20% loss respectively through the sides of the sample. If we consider both convective and radiative heat loss, the sample will have to be around 1 mm thick for something as

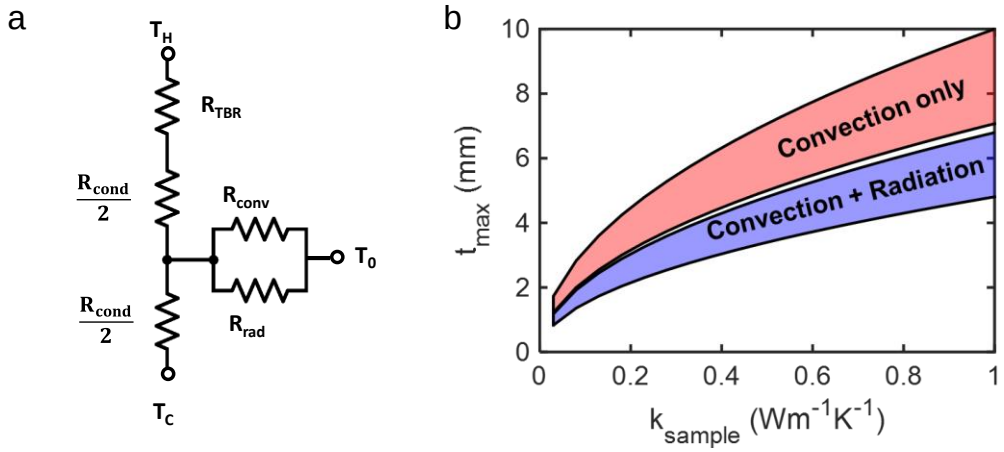

Figure 2.6. (a) Thermal circuit for heat flow from a thermally resistive sample. (b) Sample thicknesses must fall in the range of the upper and lower limits for error tolerance. In the blue region, both convection and radiation are heat loss mechanisms. The red region signifies convective heat loss only.

resistive as aerogel. However, if the sample is ~ 0.2 – 0.5 W/m/K (such as polymers or papers), then we can have samples that are few millimeters thick.

There are a few ways to reduce losses through the sides of the sample. Around room temperature, the radiation and convection heat loss coefficients are about equal (~ 5 $W/m^2/K$). Therefore, reducing radiation would increase sample thickness tolerance significantly. To reduce radiative heat losses, we can use a passive radiation shield which is typically made of highly polished metals with low emissivities.[44] Convective loss can be reduced by putting the entire system under some amount of vacuum.

For a highly conductive sample, we have a minimum sample thickness requirement. If the sample is highly conductive and thin (i.e. an undoped silicon chip or Cu metal), then thermal boundary resistances will be large enough to dominate the measurement. The minimum measurable thermal resistance also depends on the thermocouple sensitivity to small fluctuations in temperatures. Figure 2.7a is the thermal circuit for a highly conductive sample. In this case, convection and radiation do not contribute

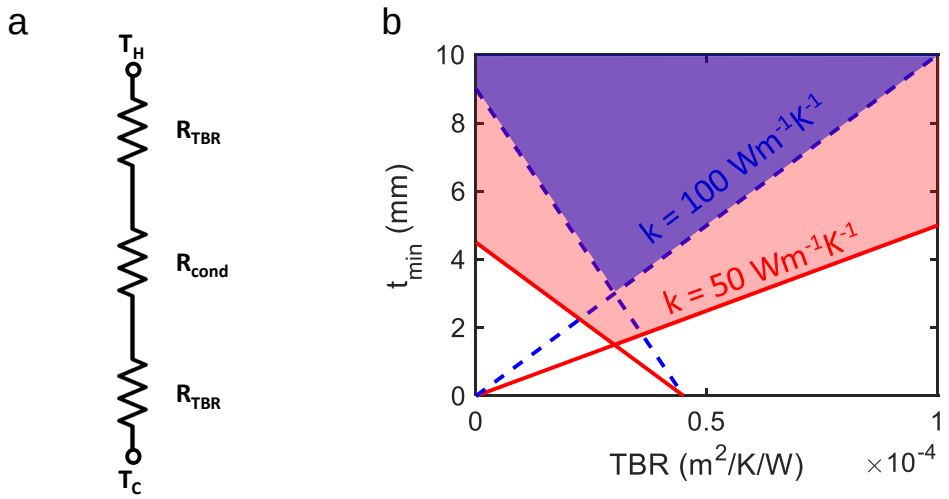

Figure 2.7. (a) Thermal circuit for heat flow from a thermally conductive sample. (b) Sample thickness requirements depend strongly on the thermal boundary resistances between the sample of the Cu reference bars. For different sample thermal conductivities, the ranges of minimum thicknesses will differ and must fall in the shaded region.

significantly to loss from the sides of the sample since the sample thermal resistance will be negligible.

There are two sets of conditions that are used to estimate the minimum thickness requirements. First, the thermal boundary resistance (R_{TBR}) must be at least equal to the sample thermal resistance (R_{cond}) which gives us the expression $R_{TBR}/A_{cross} = R_{cond}$ where A_{cross} is the cross-sectional area of the sample. Solving this expression gives the first thickness expression:

$$t \geq k_{sample} R_{TBR} \tag{2.4}$$

where k_{sample} is the sample thermal conductivity. The second condition is that the sample thermal resistance must be greater than the minimum measurable thermal resistance (R_{min}) of the system (limited by the equipment). This gives the expression:

$$R_{min} \leq 2\frac{R_{TBR}}{A_{cross}} + \frac{t}{kA_{cross}} \tag{2.5}$$

Solving for the thickness, we get an expression:

$$t \geq k\left(A_{cross}R_{min} - 2R_{TBR}\right) \tag{2.6}$$

The TBR plays a large role in how thin the samples can be. There are a few ways to reduce the contact resistances such as increasing sample pressure or using a thermal interface material. Estimates shown in Figure 2.7b are based on the thermal boundary resistances for a dry contact.[42] For a sample like Si (k_{Si} ~ 140 W/m/K [18]), the sample would need to be more than 5 mm thick which is order of magnitude greater than the thickness of a standard wafer (~500 μm).

We have now established the sample and measurement limitations of this system. The next few sections will discuss some materials that can be rapidly characterized by this technique.

2.3 Vertically Aligned Cu Nanowire Forests

Experimental results in this section were published in M.T. Barako, S.G. Isaacson, F. Lian, *et al.*, "Dense Vertically Aligned Copper Nanowire Composites as High Performance Thermal Interface Materials", *ACS Applied Materials and Interfaces,* **9**, (48), 42067, 2017. All thermal measurements were done using the 1D steady state thermal conductivity tool described above.

2.3.1 Sample Fabrication and Material Characterization

Commercial TIMs are generally greases with some nanoparticles. In 2009, DARPA created a program to address thermal interfaces with the goal of achieving a low thermal resistance TIM (< 1 mm^2K/W).[45] TIMs have two main requirements: mechanically compliant and thermally conductive. To accomplish this, nanostructures such as Cu nanowires (CuNW) were studied for this application.[35,43] In this work, we use vertically-

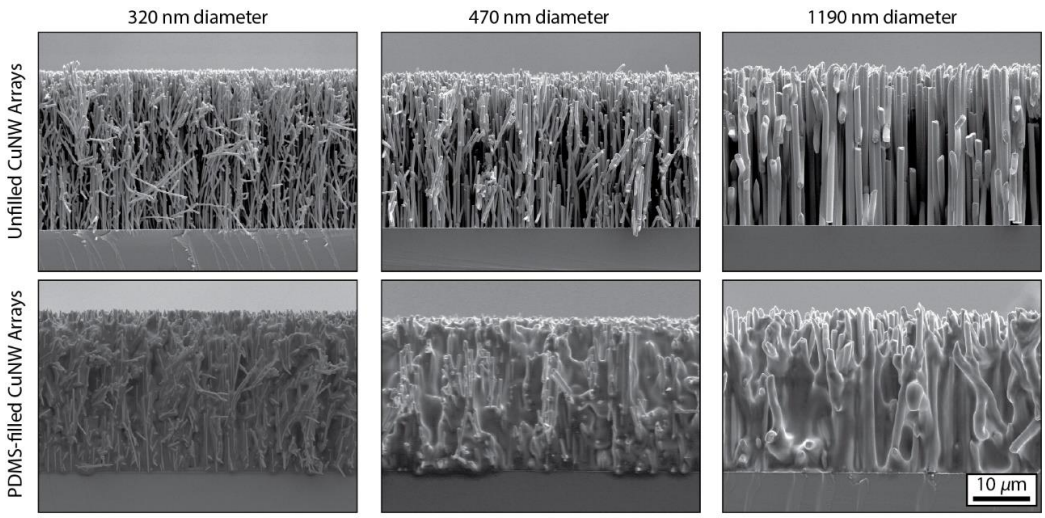

Figure 2.8. SEM images of CuNW arrays before (top) and after PDMS (bottom) infiltration. The NW diameters can be controlled by the membrane pore sizes. Figure reproduced from Ref. 43.

aligned, dense CuNW arrays embedded in a polymer matrix to combine the high thermal conductivity of Cu with the mechanical elasticity of polymers.

CuNWs were deposited in arrays using a templated electroplating method.[43] A gold seed layer is deposited onto the desired substrate. A porous polycarbonate membrane is attached to the seed layer. Cu is deposited into the membrane until a Cu overplating layer is formed on top of the NW and template membrane. The overplating layer can be removed by mechanically peeling off the Cu film. The template membrane can be dissolved using solvents leaving a standalone forest of NWs. This method of CuNW deposition is scalable to large areas. Polydimethylsiloxane (PDMS) is drop-cast around the nanowire arrays. After a while, the PMDS will wick into the array as shown in Figure 2.8. To demonstrate these forests as viable TIMs, we bond the CuNWs directly to Cu target substrates using a flip-chip bonding method.[43]

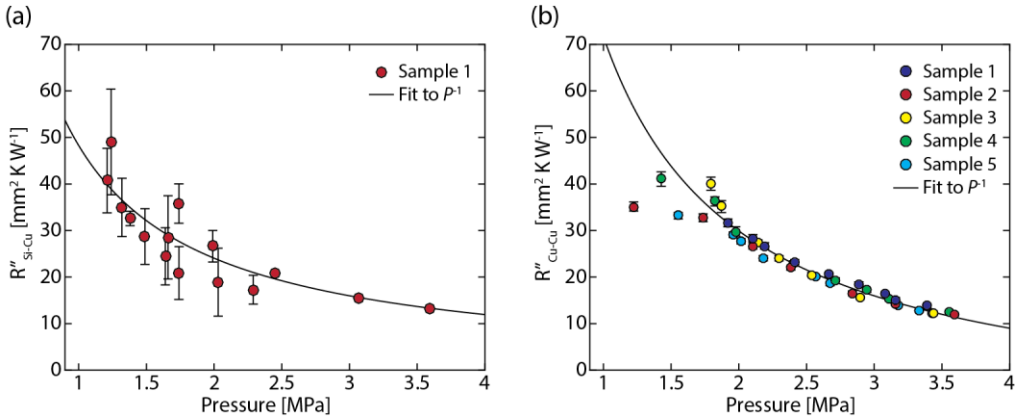

Figure 2.9. (a) Thermal contact resistance of the Si-Cu and (b) Cu-Cu interfaces as a function of pressure. Five Cu samples were measured with consistent results across all samples. Figures reproduced from Ref. 43.

2.3.2 Results and Discussion

To study the thermal performance of these samples, we use a pressure dependence study. Since the sample is grown on a Si substrate, a measurement of the as-grown CuNWs on Si would have two interfaces: Cu-Si interface at the cold meter bar and the Cu-Cu interface between the NWs and the hot meter bar (Figure 2.4). To account for parasitic resistances, we conduct a series of pressure dependent measurements on control samples (Figure 2.9). The Si-Cu interfacial resistance is estimated by using different thickness of PDMS coatings on Si substrates. Assuming the PDMS is thermally resistive (therefore TBR between PDMS and hot meter bar is negligible), the Si-Cu resistance can be estimated. The Cu-Cu interface is estimated by measuring a 0.3 mm-thick Cu substrate. Cu is thermally conductive (k ~ 385 W/m/K), therefore, the measurements would be contact resistance dominated. Since we are trying to estimate the TBR and not measure the thermal resistance of the Cu itself, this sample thickness is valid.

We estimate the uncertainty for the sample resistance (CuNW array) to be < 5% for all samples based on the difference between the heat flux of the top and bottom Cu meter

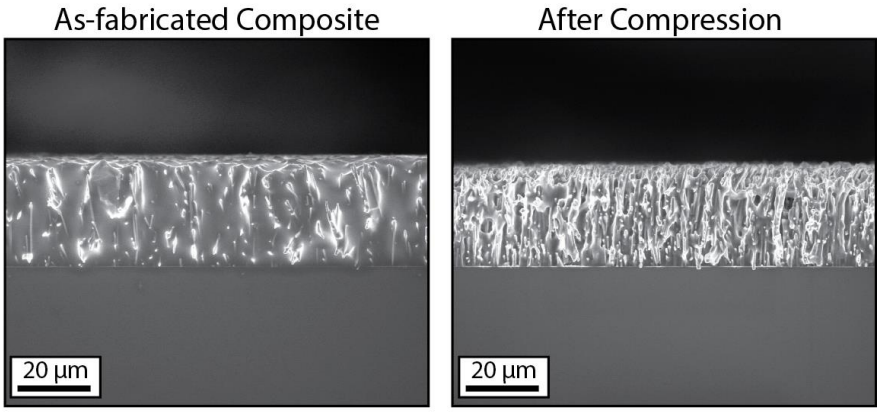

Figure 2.10. SEM image of the composite before and after about 3.5 MPa compression. The NWs are still intact despite large forces due to the PDMS matrix. Images reproduced from Ref. 43.

bars. However, the contact resistance is still the dominant source of uncertainty since the CuNWs are intrinsically thermally conductive. In this study, the measurement relies on the resolution of the tool which is limited by the thermocouple placement and sensitivity. Figure 2.10 shows the post compression scanning electron microscope (SEM) images. The PDMS array dissipates the compressive strain on the NWs and keeps them from collapsing. Finally, we measure the bonded samples (shown in Figure 2.11) and compare them to the commercially available TIMs. We were able to demonstrate scalable CuNWs-based TIMs with ten times better performance than commercial TIM materials.

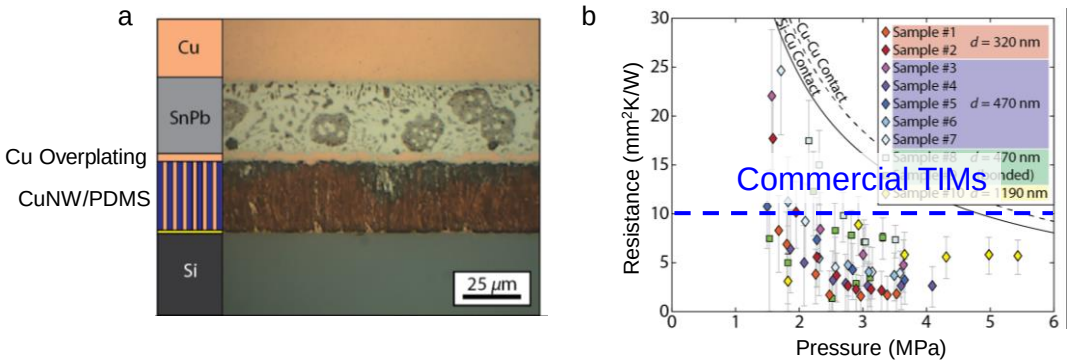

Figure 2.11 Figures adapted from Ref. 43. (a) Optical image of the cross-section of a bonded sample. The polymer embedded CuNWs are bonded to a Cu substrate using a SnPb solder. (b) Thermal resistances of the measured samples compared as a function of pressure.

2.4 Concurrent Seebeck Measurements

As discussed in Chapter 1, a Seebeck coefficient is the electrical potential across a material in the presence of a temperature gradient. In the 1D measurement method, a temperature gradient must be established to measure thermal conductivity. If the sample also has a Seebeck coefficient, we can measure this by connecting the top and bottom meter bars to a voltmeter. Therefore, we can simultaneously measure the Seebeck coefficient and thermal conductivity of a sample. Figure 2.12 shows the rapid characterization of the Seebeck coefficient and the thermal conductivity of metal organic frameworks (MOFs).

MOFs are made by joining inorganic metal ions/clusters with organic linkers. MOFs are highly porous and can be designed at the molecular level. These materials are chemically synthesized, allowing a bottom-up approach to engineering macroscopic materials for different applications. One application of interest is to use MOFs for thermoelectrics. The as-synthesized MOFs can be compressed into macroscopic pellets that are ~100 μm thick. Compared to bulk metals, MOFs have two orders of magnitude higher Seebeck coefficient (S_{ZnHAB} ~ 230 μV/K, S_{Zn} ~ 2.4 μV/K [46]) (Figure 2.11b).

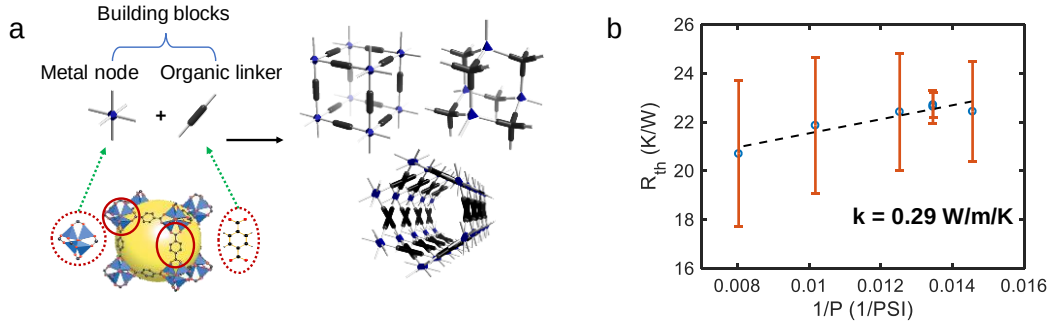

Figure 2.12. (a) MOF structure.[47] (b) Thermal resistance and concurrent Seebeck coefficient measurements.

However, more work needs to be done to improve the electrical conductivities of these materials. Due to the porous natures of these materials, the thermal conductivity is naturally low making them a promising candidate for thermoelectrics assuming the improvements in electrical conductivity can be achieved.

Another material system that is of interest for thermoelectrics are polymer-based thermoelectrics. Poly(3,4-ethylenedioxythiophene) poly(styrenesulfonate) (PEDOT:PSS) is a popular polymer for thermoelectrics due to its high electrical conductivity and Seebeck coefficient. Many researchers have studied the use of PEDOT as a polymer matrix for other nanomaterials such as CNTs.[48] Two existing issues PEDOT are costs and mechanical strength. Cellulose fibers, which are based on plant cell walls, can be introduced into PEDOT to provide additional mechanical strength for flexible thermoelectric applications. Figure 2.13a shows the PEDOT:PSS and cellulose composite. In this case, we can use a concurrent Seebeck measurement (Figure 2.13b) to rapidly characterize the performance of the PEDOT:PSS-cellulose (PPC) composites. Since these materials are polymer-based, we expect the thermal conductivity to stay relatively low. Therefore, the focus should be on optimizing the thermoelectric and electrical performance.

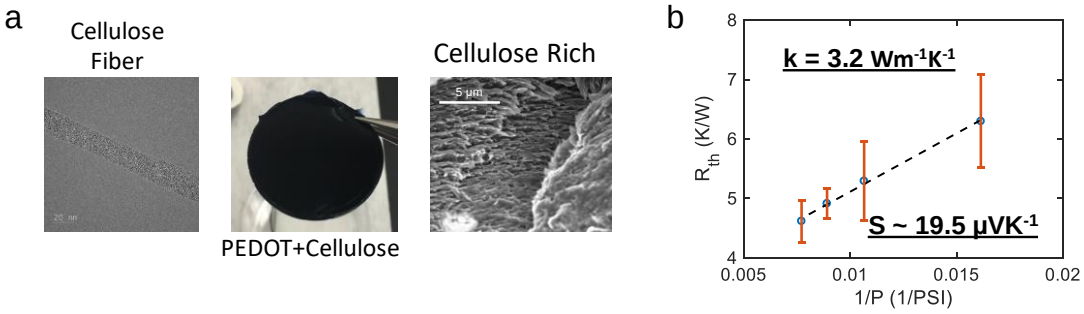

Figure 2.13. (a) Left panel shows a transmission electron microscope image of a cellulose fiber, middle panel shows a PPC composite, and right panel shows an SEM image of the cellulose wrapped with PEDOT:PSS. (b) Thermal resistance and Seebeck measurement of the PPC composite.

2.5 Conclusions

The 1D steady-state thermal measurement system allows us study bulk material thermal and thermoelectric properties. The tool has certain limitations for extremely thermally resistive or conductive samples but can also be applied to measure novel materials such as polymers and MOFs. Improvements can be made in the design and implementation of the tool such as adding radiation shielding or reducing convective heat losses. This tool allows us to rapidly characterize sample properties. However, decoupling physical transport mechanisms would require additional modeling and/or samples.

Chapter 3
Suspended Infrared Thermometry of Chirality-Sorted Single-Walled Carbon Nanotubes

In this chapter, we present a study on thermal transport in chirality-sorted SWNT networks. We discuss the design of an infrared suspended thermal platform and thermometry technique for rapid thermal characterization of conductive materials. This chapter is adapted from F. Lian *et al.*, "Thermal Conductivity of Chirality Sorted Carbon Nanotube Networks", *Applied Physics Letters* **108**, 103101 (2016).

3.1 Thermal Conductivity in Carbon Nanotube Networks

Carbon-based nanomaterials have a wide range of thermal conductivities due to its various allotropes and atomic structures. In sp^2- and sp^3-hybridized carbon lattices (e.g. graphene and diamond), thermal conductivities (k) can exceed 3000 W/m/K. Amorphous carbon, which is consists mainly of air, has $k \sim 0.01$ W/m/K (Figure 3.1).[20] Individual CNTs have excellent thermal and electrical conductivities. However, how morphology plays a role in thermal transport in CNT networks is not well understood. Tuning the thermal properties of CNT-based materials would allow us to engineer materials for applications ranging from heat spreading to thermoelectrics or thermal insulators. With the use of sorting to separate metallic (m-) and semiconducting (s-) SWNTs, it is unclear if the electronic type of a SWNT would play a role on thermal transport.

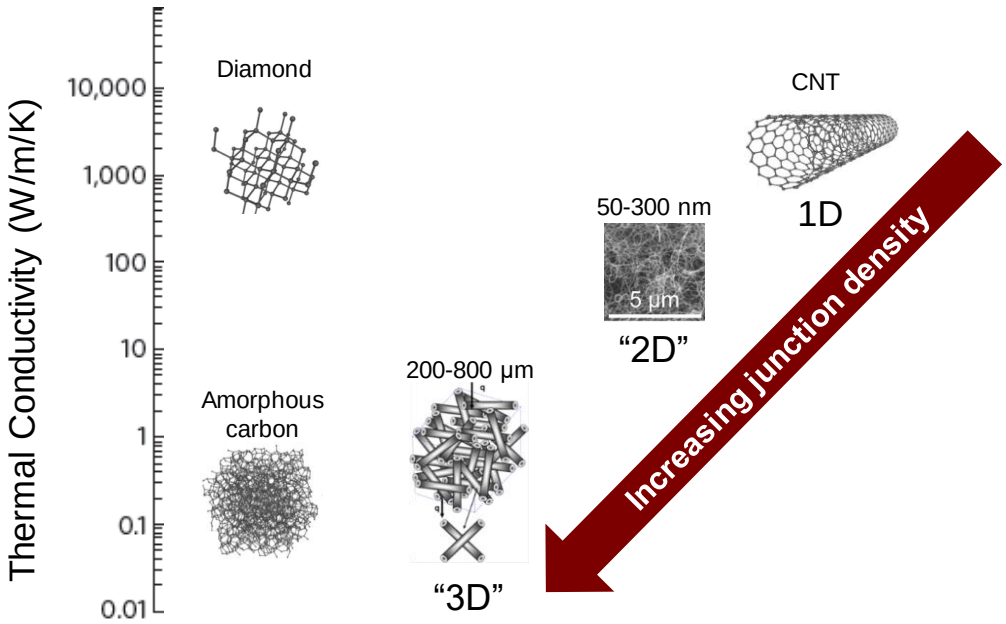

Figure 3.1. Thermal conductivities of carbon materials. Diamond and CNTs have the highest intrinsic thermal conductivities. Amorphous carbon has extremely low thermal conductivity due to its porosity and lack of crystallinity. CNT-based materials have highly tunable thermal conductivities based on their morphology and junction density.

In CNT networks and films, the effective thermal conductivity of the network is much lower than the thermal conductivity of individual CNTs. This is due to the high inter-tube junction thermal resistance.[49,50] Previous studies on thermal conductivity in CNT networks have found k to reduce by almost three orders of magnitude depending on the CNT junction density in the network.[51] Prasher *et al*. estimated the thermal conductivity of dense beds of SWNTs to be a function of the volume fraction ϕ:

$$k_{\text{bed}} = 1/3 k_{\text{CNT}} \phi \tag{3.1}$$

Volume fraction can be altered by mechanical pressure or by using solvents to densify the network [51].

Previous work shows that electrical conductivity scales as a function of the average nanotube bundle length, $L_{av}^{1.46}$, since longer tubes will have fewer junctions in order to cross a surface.[52] For thermal conductivity scaling with nanotube morphology, Volkov *et al*. explored the thermal transport of networks and the effect of nanotube density and average length using a combination of theoretical analysis and mesoscopic simulations.[53-55] Assuming that nanotube chirality is the same throughout the network and the mass density is 0.2 g/cm^3, the thermal conductivity scales as $k \sim L^2$ for 3D bulk films and for quasi-2D films where L is the nanotube length. Zhong and Lukes have shown through molecular dynamics simulations that the thermal interfacial resistance of CNT junctions decreases as nanotube overlap area increases.[49] However, although previous works have shown that junction type, e.g. between metallic (M) and semiconducting (S) CNTs, affect electrical transport, no study has explored the thermal transport in networks with controlled junction type, bundle diameter, and bundle length.[56,57]

Furthermore, with the advancement of sorting SWNTs, building unique bulk materials from nanotubes requires some form of solution processing in which the nanotubes are first dispersed in a solution and later deposited either directly onto a substrate or filter to form free standing films. Previous measurements on low thermal conductivity carbon nanotube 'mats' were based on dry nanotube samples which were mostly air and very low density.[51] This study looks at creating free standing films from solution processed, sorted SWNTs and studying the thermal and electrical properties of these macroscopic materials.

3.2 Experimental Methodology

3.2.1 Sample Preparation and Suspension

We use 90% semiconducting (IsoNanotubes-S), 90% metallic (IsoNanotubes-M), unsorted and purified (PureTubes), and unsorted HiPco SWNTs purchased from NanoIntegris.[58] The IsoNanotubes and PureTubes have SWNT diameters ranging from 1.2–1.7 nm with a mean of 1.4 nm. The metallic tubes have a mean length of 0.5 μm.

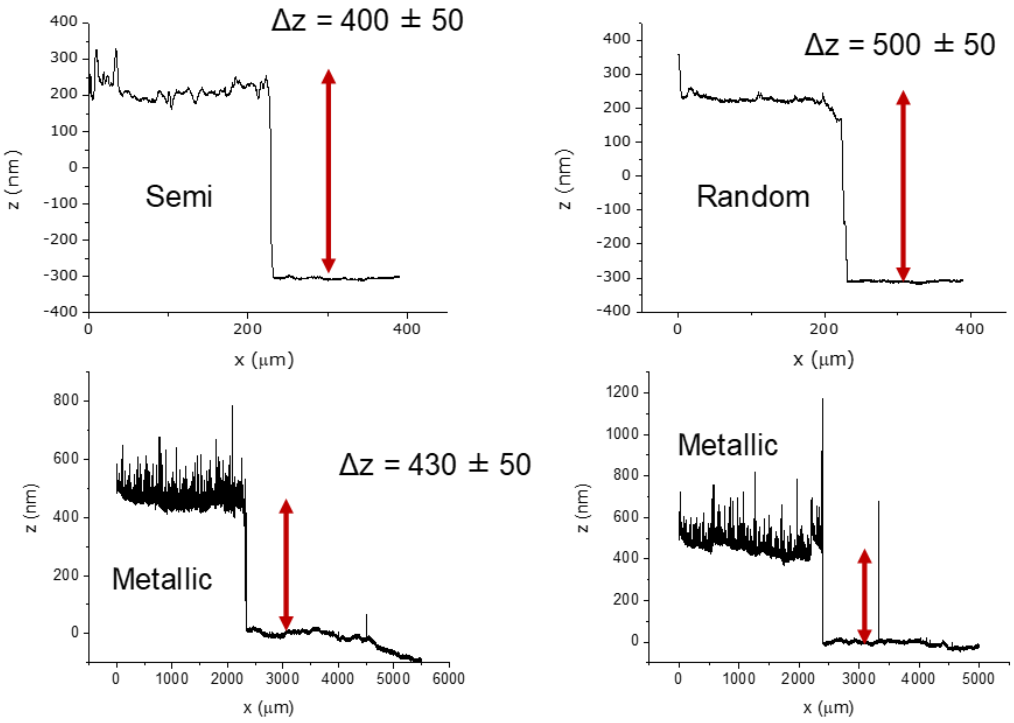

Figure 3.2. Profilometer measurements of the SWNT films on Si substrates. Thicknesses (t_{film}) were used for extracting thermal conductivity in the model. Metallic films had more surface roughness, but their overall film thickness is estimated to be 400-500 nm. The mass density of the film is also calculated from the thickness and the mass of the SWNTs used in the film assembly.

The semiconducting and purified tubes have a mean length of 1 μm. The HiPco SWNTs have diameters ranging from 0.8–1.2 nm with lengths ranging from 0.1–1 μm. The unsorted HiPco and purified tubes have a semiconducting to metallic ratio of 2:1, i.e. ~33% metallic. We assemble the SWNTs into films on nitrocellulose membranes (MCE MF-Millipore 47 mm diameter, 0.025 μm pores) using vacuum filtration. The filters are dissolved using two 30-minute, heated acetone baths, leaving only the freestanding films.

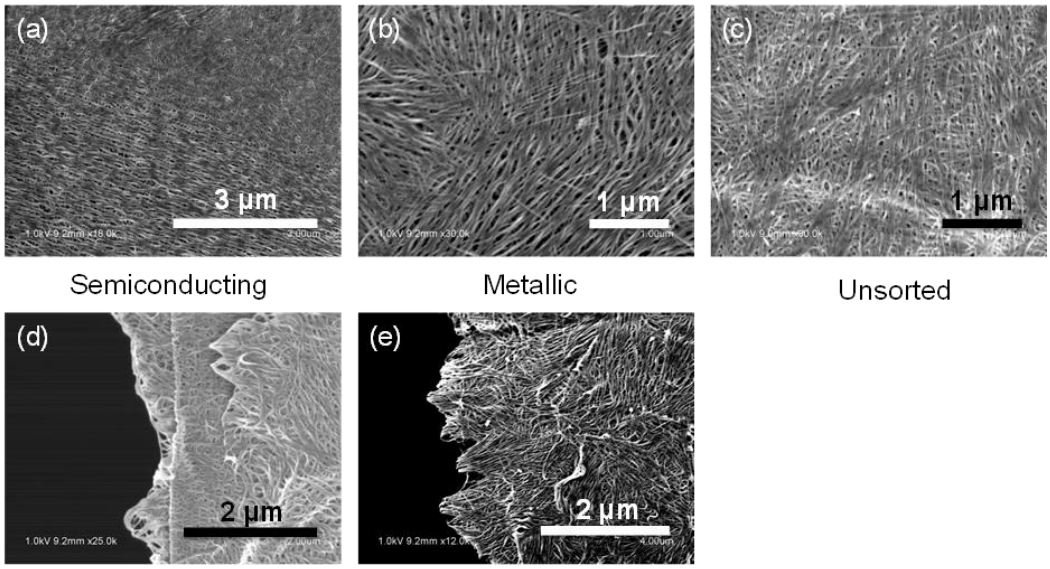

Figure 3.3. SEM images of our solution-assembled SWNT networks. (a) – (c) show SEMs of the center of the film for semiconducting, metallic, and unsorted networks, respectively. Figures (d) and (e) show the edge of the film for the semiconducting and metallic networks respectively. The edge roughness of the film is due to the cutting of the film following the vacuum filtration assembly.

The SWNT films are then suspended across the thermometry platform by directly removing them from the acetone using the measurement platform. Film thickness measurements were done using profilometry on SWNT films transferred onto Si substrates as shown in Figure 3.2. We found the metallic films to have much higher surface roughness and overall film thicknesses for all samples to be around 400-500 nm. We use the thickness for the thermal conductivity and mass density extractions which will be discussed below.

Scanning electron microscope images of the solution-assembled films reveal bundling in the networks and quasi-alignment laterally as shown in Figure 3.3. The nanotube bundles lay randomly in-plane. Due to solution processing, the bundles are very large in these films. Figure 3.3d and e show the edges of the film after the network

was cut for measurements. The edge roughness of the films is less than the spatial resolution of the infrared microscope and therefore does not affect the measurements.

3.2.2 Suspended Infrared Thermal Microscopy

We use the Quantum Focus Instruments (QFI) InfraScope to measure the temperature of suspended SWNT films at slightly elevated background temperature, T_0 = 80 °C, which improves the signal-to-noise ratio.[59-61] Suspending the samples across the thermometry platform enables 1D heat flow and sufficient mechanical support for the suspended film.[62,63] (This is in contrast to our earlier work[60,61] that used much thinner samples on SiO_2/Si substrates, where the parasitic heat flow path into the substrate could not be avoided, preventing an analysis of the in-plane thermal conductivity.) The large contacts are electrochemically polished Cu blocks coated with 200 nm/150 nm electron-beam evaporated Ti/Pd, Pd being in contact with the SWNTs. Thin ceramic washers electrically isolate the contacts and control the gap distance (L) between the Cu blocks.

To calibrate our samples, we begin by taking an unpowered reference radiance measurement of the film. Emissivity values are calculated by the scope and later used to calculate the radiative heat loss from the SWNT films. Once a reference image is taken, a background temperature map is captured where there is no heat flow (shown in Figure 3.4b). We apply a voltage bias to flow current (in the y-direction) through the suspended sample, to induce Joule heating and map the temperature in real time, as shown in Figure 3.5a,c. The SEM image in Figure 3.5b reveals some local alignment and bundling of SWNTs in the network, which we attribute to the vacuum filtration assembly method of the films. Otherwise, the SWNTs are randomly oriented in the (x-y) plane of the filter, with fewer SWNTs crossing over in the z direction.

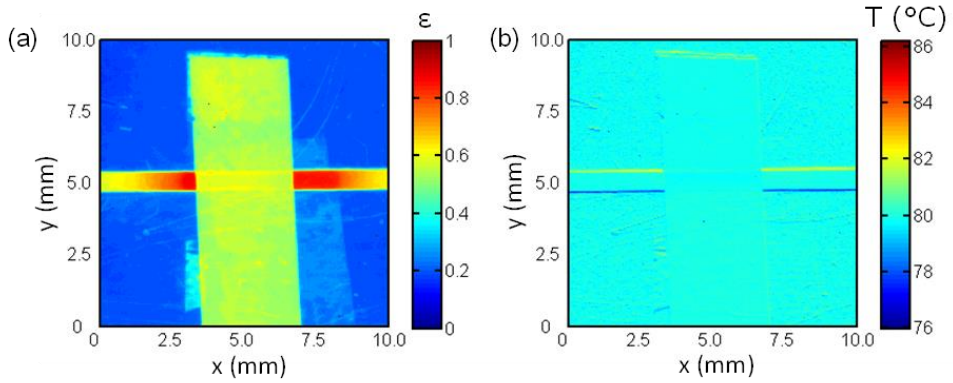

Figure 3.4. (a) Reference radiance measurement of unsorted film from IR scope. Values for emissivity (ε) are used to calculate the radiative heat loss from the SWNT film. The average emissivity of the SWNT films are listed in Table 3.2. We directly measured the emissivity of the Pd coated Cu contacts to be $\varepsilon \approx 0.16$, as expected. (b) Background temperature measurement performed without any applied bias across the SWNT film. Slight color difference at edges of metal contacts are due to reflection from the edges of the contacts.

Temperature maps like the one in Figure 3.5c are taken while the device is biased as shown in Figure 3.5a. The temperature is averaged over a range of pixels in the *x*-direction, across the inner rectangle in Figure 3.5c. As shown in Figure 3.5d, the temperature profile peaks in the center of the suspended film with negligible heating at the contacts, indicating good heat sinking by the Pd-coated Cu blocks. We simultaneously obtain electrical measurements of the samples, including the electrical contact resistance using the transfer length method (TLM), by measuring samples with varying suspended separations (L = 0.7–2.0 mm) between the Cu blocks. We combine the thermal imaging maps with a computational model to simultaneously extract the thermal contact resistance and the thermal conductivity from the measured temperature profile. As it turns out, accounting for both electrical and thermal contact resistance is

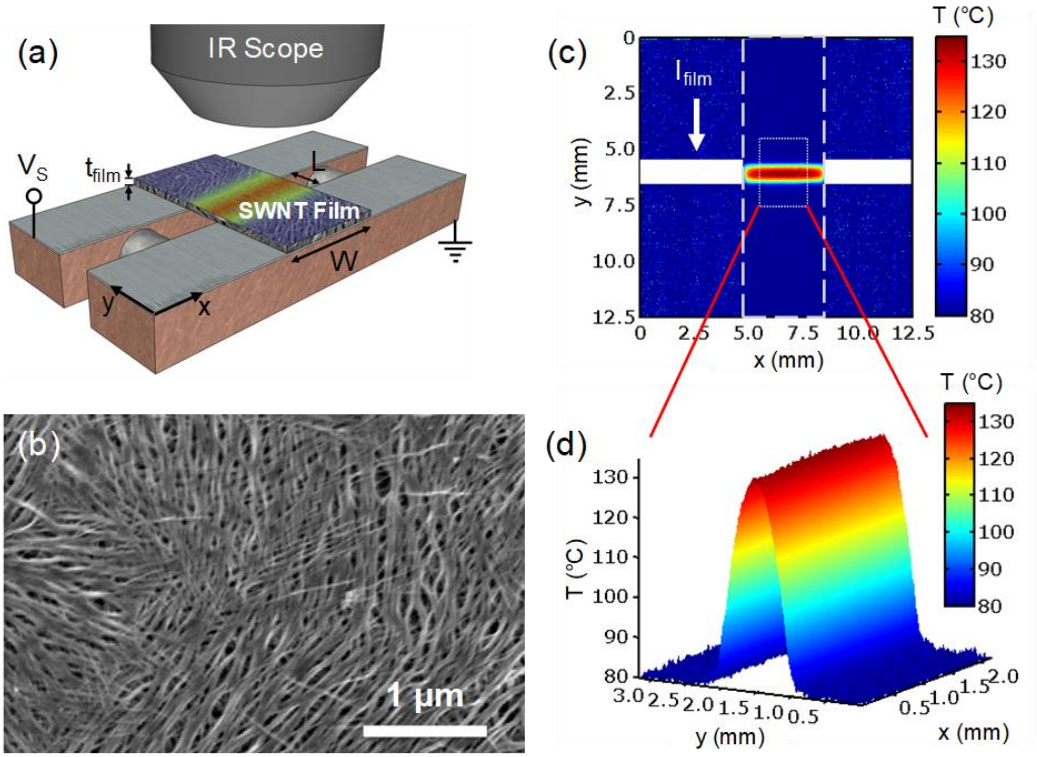

Figure 3.5. (a) Schematic of the thermometry platform and the experimental set up. SWNT films are suspended across two Pd-coated Cu blocks that are electrically isolated by ceramic washers. (b) SEM image of the SWNT film after vacuum filtration. The SWNTs are bundled and randomly in-plane oriented. (c)Temperature map of the SWNT film across the metal contacts. White dashed lines show the edges of the SWNT film, and current flows in the direction of the arrow. (d) The zoomed-in temperature profile of the suspended SWNT film across the gap. The 1D temperature profiles in Figure 3.9 are averaged along the *x*-direction of such maps.

important for obtaining the intrinsic thermal conductivity of the suspended SWNT films. Figure 3.6 shows the temperature profiles and SEM images of the (a) semiconducting, (b) unsorted, and (c) metallic films. The top and middle rows show two different biases and dissipated power, respectively, as labeled in the figure insets. The direction of current flow in Figure 3.6a is from the top to the bottom contact (shown by

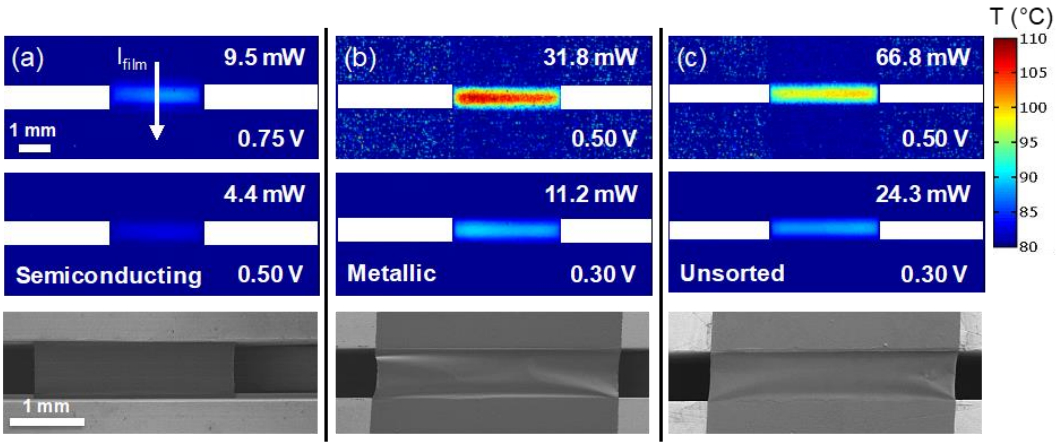

Figure 3.6. Temperature profiles and SEMs of (a) semiconducting, (b) unsorted, and (c) metallic SWNT. Top and middle panels correspond to higher and lower power applied to the networks, respectively. The insets list the applied voltages and the power dissipated in the suspended portion of the films, excluding contact resistance, $(V/R)^2(R - 2R_C)$. The vertical arrow shows the current flow direction. Some bowing in the films from the transfer process can be seen in the SEMs for the metallic and unsorted networks.

the arrow), with no measurable change in the temperature profile when reversing the current flow direction. The semiconducting film was the most resistive and therefore had the least heating, largely due to its contact resistance (Figure 3.7). This is not unexpected, because the films are suspended and cannot be gated. Given the voltage biasing scheme, the Joule heating in this film ($\propto V^2/R$) is mainly in the percolation paths that include the less resistive, ~10% metallic SWNTs.[60] The metallic networks have lower electrical resistance and a higher temperature rise for the same applied potential. For the unsorted SWNT films, the temperature rise is in between the metallic and semiconducting films, which is expected since the metallic-semiconducting nanotube junctions have higher electrical resistance and there are an "intermediate" number of

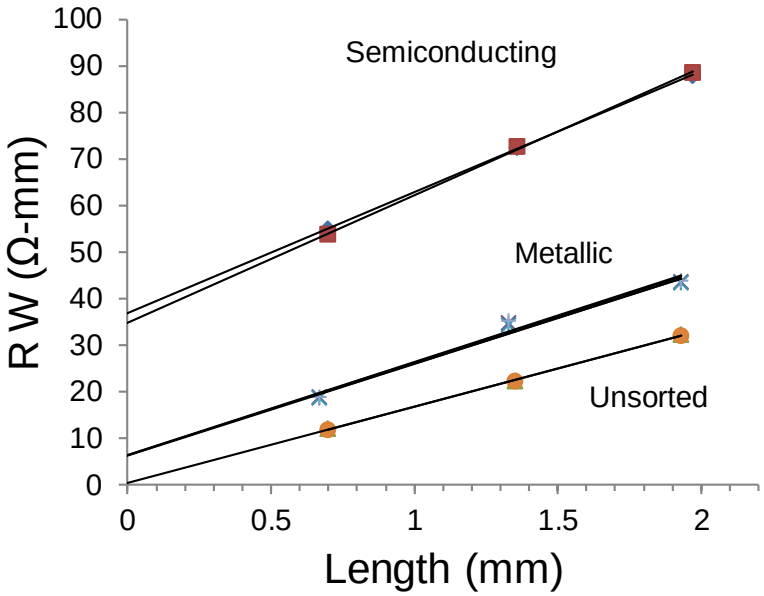

Figure 3.7. Transfer length method (TLM) plot of electrical resistances of the films (multiplied by their width) as a function of suspended film length. Symbols are experimental data and lines are linear fits. The vertical intercept represents twice the electrical contact resistance ($2R_C W$), the slope represents the SWNT film sheet resistance (R_{sh}), and the horizontal intercept represents an estimate of the transfer length ($2L_T$). Multiple measurements were taken at several voltage biases, and the equation of the linear fit to each is given in the inset. The unsorted samples were biased at 0.5 V and 0.3 V, and the metallic samples were biased at 0.75 V, 0.5 V, and 0.3 V with no noticeable change in resistance of either sample. The semiconducting sample was biased at 0.75 V and 0.5 V and a slight decrease in resistance was observed at the higher bias.

metallic percolation paths in this film.[57,64] Contact resistance is most significant for the semiconducting network and varies depending on the surface roughness of the contacts, as well as the presence of residue between the SWNT film and the metal surface. (We measured the RMS roughness of the metal contacts to be ~165 nm.) We believe the unsorted networks have lower contact resistance since they have much less damage (no

sorting) and much less residue. Importantly, the electrical contact resistance was always considered in all power input calculations for the extraction of thermal conductivity.

To extract the thermal conductivity of the sample, we use a finite element analysis of the 1D heat transfer equation:[65]

$$A\frac{\partial}{\partial y}\left(k\frac{\partial T}{\partial y}\right)+p'-g\left[T(y)-T_0\right]=0 \tag{3.2}$$

where $A = Wt_{\text{film}}$ is the cross-sectional area of the film, k is its in-plane thermal conductivity, p' is the Joule heating power per unit length, g is the heat loss coefficient per unit length to the air or to the contacts (discussed below), T_0 = 80 °C is the background temperature of the device, and $T(y)$ is the temperature at location y along the film. This approach implies uniform thermal conductivity and power distribution along the film, which are found to be reasonable assumptions given the uniform density of SWNTs (Figure 3.5b) and the good fit to the measured data, as we will see below. Since the thermal measurements are done in air, we account for heat loss due to convection and radiation using the heat loss coefficient g_s for one surface of the SWNT film exposed to air:

$$g_s = Wh_{\text{conv}} + W\varepsilon\sigma_{\text{B}}\left[T(y)^2+T_0^2\right]\left[T(y)+T_0\right] \tag{3.3}$$

where h_{conv} is the heat convection coefficient per unit area[66], ε is the emissivity of the film as measured by the IR scope (Figure 3.4a), and σ_{B} is the Stefan-Boltzmann constant. h_{conv} is taken between 5 to 10 W/m^2/K for natural convection in air[66] and the uncertainty to k introduced by this range is small, less than 2% as shown in Table 3.1. Because the IR scope captures a spatial temperature map of heating in the film, we can use the measured temperature values to calculate g_s at each point "y" along the sample to directly calculate the heat loss due to radiation. For the suspended portion of the film, $g = 2g_s$ since both top and bottom surfaces should be taken into account; $p' = (V/R)^2(R - 2R_C)/L$, where R is the measured total electrical resistance of the film and R_C is the electrical contact resistance (Table 3.2).

	k (W/m/K)	parameter	t_{film} (nm)	W (mm)	$2R_c$ (Ω)	h_{conv} (W/m^2/K)	ε
90%-S	174 – 220	input error	400±50	2.5±0.1	35.9±1.0	5±5 (i.e. 0–10)	0.58±0.01
		k uncertainty	~12%	~4%	~3%	~2%	~0.1%
90%-M	107 – 137	input error	430±50	3.6±0.05	6.35±0.1	5±5 (i.e. 0–10)	0.37±0.01
		k uncertainty	~25%	~1%	~1%	~2%	~0.1%
Unsorted	286 – 368	input error	500±50	3.3±0.03	0.34±0.005	5±5 (i.e. 0–10)	0.57±0.01
		k uncertainty	~10%	~1%	~1%	~2%	~0.1%

Table 3.1. Calculated uncertainty analysis for the extracted SWNT film thermal conductivity (k) in our measurements. We consider the errors from the film thickness, contact resistance, and convection and radiation losses. The main uncertainty resulted from the thickness of the film which can be seen from Figure 3.2. We note that the true cross-sectional area of the SWNT film is *not* Wt_{film} because the SWNTs are not fully packing the rectangular parallelepiped with volume WLt_{film} (see Figure 3.5). We can estimate the fill factor by two means: 1) the estimated mass density is ~1.1 g/cm^3 which is approximately 50% that of graphite, indicating about 45% fill factor in the network. 2) the estimated thermal k is approximately 10% that of graphite. We regard the former estimate as more accurate for the fill factor, and attribute the thermal k being lower than $0.45k_{graphite}$ to the effects of intertube junctions and misalignment.

We find that accounting for R_C is essential in such Joule self-heating studies, because excluding it would lead to an overestimation of the power input and corresponding overestimation of the extracted k, which may have been the case in a previous study.[63]

In this work, neglecting R_C would result in an estimated 60% higher k for the metallic networks.

For the portion of the film supported by the contacts, $p' = 0$ and $g = g_s + Wh_C \approx Wh_C$, where h_C is the thermal contact conductance per unit area between the film and the Pd/Ti/Cu contact. To extract the thermal conductivity of the SWNT film, Eq. (1) is solved by using k and h_C as fitting parameters for the best fit to the average temperature profile of the film obtained by the IR scope. We verify our results by comparing the 1D model with a three-dimensional (3D) COMSOL thermal model of the SWNT film, shown in Figure 3.8.

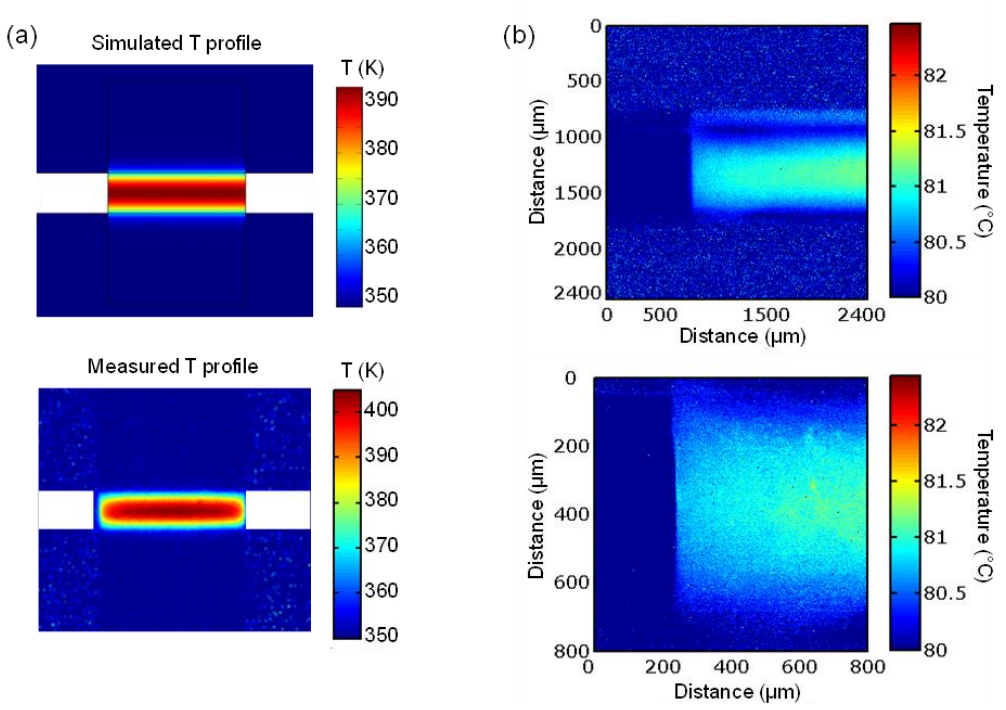

Figure 3.8. (a) Shows a comparison of a 3D finite-element (COMSOL) model (top) with the measured temperature profile at 5× magnification (bottom). Non-uniformities in the measured profile are an artifact of the IR scope due to the spatial resolution of the objective. (b) Temperature profile of the films at 10× and 15× magnification.

The uncertainty in the extracted k due to assumptions about radiation and convection is less than 2%, as discussed in Table 3.1. These are smaller than the uncertainty in film thickness due to surface roughness (Figure 3.2), which has between 10-25% effect on the extracted k values.

Figure 3.9 shows the thermal model fitted to the temperature profiles of the different SWNT films [averaged along the x-direction of the rectangular region in Figure 3.5(c)]. For the semiconducting, unsorted, and unsorted HiPco films, the model shows excellent agreement with the measurements, validating our assumptions of uniform thermal conductivity and uniform heat generation. For the metallic film, we noticed discrepancies between the model and the experimental data near the contacts. For a better fit, we can slightly increase the gap distance L in the model because the physical length of the suspended SWNT film may be larger than the contact separation (the buckling of metallic films was greater during transfer and suspension, as seen in Figure 2c). Thus, we extract a range of thermal contact conductance $h_C = 2\times10^3$ to 3.5×10^4 W/m^2/K for all films, recalling that the contacts are at the ambient temperature $T_0 = 80$ °C. These values are nearly four orders of magnitude lower than those between individual SWNTs[67] or graphene[68] and SiO_2, ostensibly due to partial contact between the SWNT network with Pd, due to process and transfer residues, and due to some surface roughness of the metal contacts. The thermal contact conductance of the unsorted films is also at least a factor of two larger than those of the sorted films, which are expected to have some residue from the sorting process (Table 3.2).

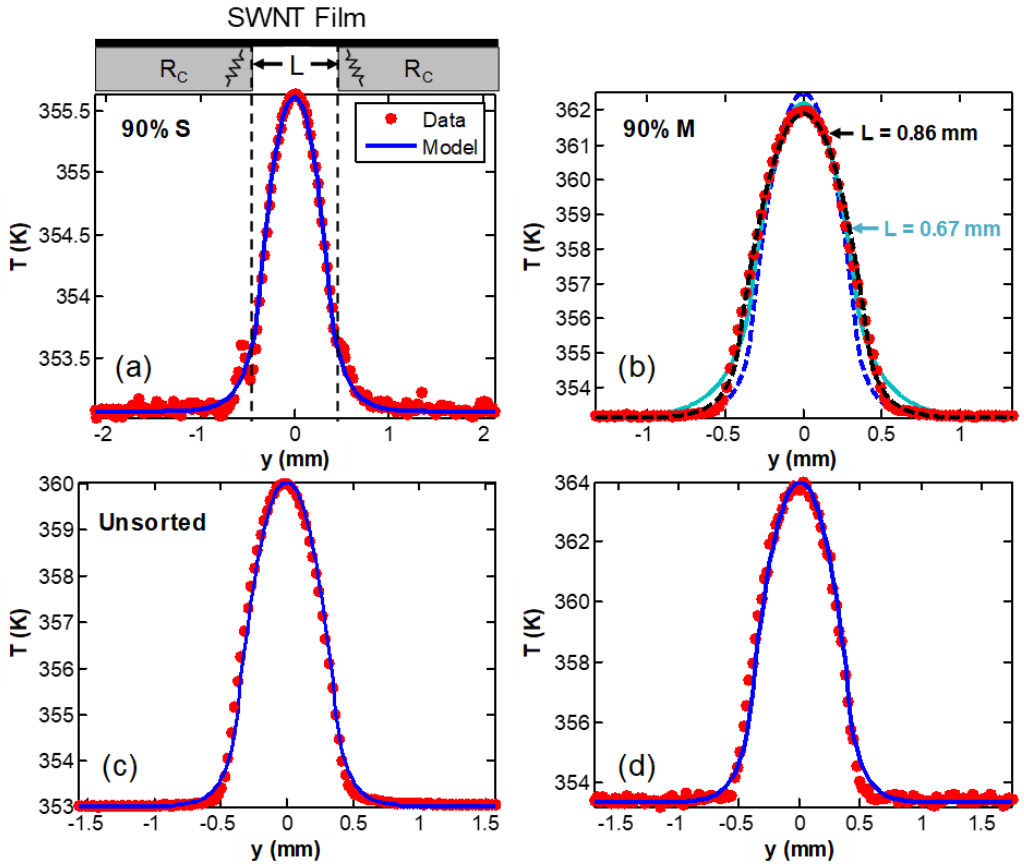

Figure 3.9. Averaged temperature profiles (symbols) fitted by the model (lines) for (a) the semiconducting film, (b) metallic film, (c) purified unsorted film, and (d) as-grown HiPco film. The upper panel in (a) illustrates the role of the electrical and thermal contact resistance. In (b), there is a slight discrepancy between the model and the measured temperature profile for the metallic film. The light blue dashed line shows the model using the measured gap distance (L = 0.67 mm) as the length of the suspended portion of the film. The black dashed line denotes the model adjusted using a larger gap distance (L = 0.86 mm). The blue dashed line shows the effect of fixing the thermal contact conductance while using the physical gap distance.

Film Type	σ (S/m)	R_{sh} (Ω/□)	$2R_CW$ (Ω·mm)	L_T (mm)	k_e (W/m/K)	t_{film} (nm)	Mass (μg)	ρ (g/cm^3)	h_c (m^2K/W)
90%-S	~ 8.34×10^4	~26	~35.0	~0.65	~0.74	450 ± 50	400	~0.51	3.0×10^3 – 1.6×10^4
90%-M	~ 1.17×10^5	~20	~6.35	~0.16	~1.07	430 ± 50	800	~1.07	6.0×10^3 – 8.0×10^3
Unsorted	~ 1.22×10^5	~16	~0.34	~0.10	~1.10	500 ± 50	500	~0.58	1.5×10^4 – 2.0×10^4

Table 3.2. Electrical and physical properties for the 90% semiconducting, 90% metallic, and purified unsorted films. Electronic contribution to thermal conductivity is estimated using the Wiedemann-Franz Law, $k_e = \sigma L_0 T$ where σ is the electrical conductivity extracted from the TLM measurements, L_0 is the Lorenz constant and T is the temperature. The unsorted, purified tubes are higher quality than the sorted semiconducting and metallic networks, leading to the higher electrical conductivity. The mass density of the metallic network is also twice as high as the semiconducting and the unsorted networks, which leads to higher junction density. We believe the higher junction density and shorter SWNT lengths (also indicative of more damage) are responsible for the thermal conductivity of the metallic networks being somewhat lower.

3.3 Experimental Results

In Figure 3.10, we compare our measured thermal conductivity values with literature values of different carbon nanotube materials, at or near 300 K. Suspended, individual SWNTs[68-70] have a very high thermal conductivity near room temperature, ~3000 W/m/K. A study of aligned multi-wall nanotube (MWNT) films[63] reported the highest in-plane thermal conductivity of such composites to date, ranging from 472–766

W/m/K. (However, this study[63] did not account for the effects of electrical contact resistance, potentially overestimating the thermal conductivity of the films, as we discussed above.

The SWNT films in this work have thermal conductivities ranging from approximately 80–370 W/m/K when both electrical and thermal contact resistances were carefully considered. The highest thermal conductivities were achieved in our purified, unsorted SWNT films, from 117–368 W/m/K. Our metallic SWNT films have extracted thermal conductivities ranging from 106–137 W/m/K, which is lower than the sorted semiconducting and the purified, unsorted solution processed films. We attribute the differences to SWNT length (metallic ones being shorter, as stated earlier), possible damage from the sorting process, and the presence of surfactants on the metallic SWNTs. The as-grown HiPco SWNT films have the lowest thermal conductivities ranging from 81–97 W/m/K. The semiconducting SWNT film thermal conductivities range from 174–220 W/m/K. The ranges of these measurements correspond to values measured across multiple samples.

Using the Wiedemann-Franz Law, we estimate the electronic contribution to thermal conductivity to be $k_e < 1.1$ W/m/K in all our SWNT films (Table 3.1). Thus, we find that the thermal conductivity has essentially no dependence on the chirality or electronic type of the SWNTs, confirming that heat flow is predominantly carried by lattice vibrations (phonons) rather than electrons and that the phonon dispersion changes very little between SWNTs of different chirality.[71, 72] Instead, our results are consistent with the view that the thermal conductivity of SWNT films depends more strongly on the SWNT junctions and the mass density of the films (which also controls the junctions and the SWNT segment lengths between junctions[73]). Previously reported solution-processed SWNTs[74,75] found cross-plane thermal conductivity around 1.68 W/m/K for millimeter-thick SWNT films[74] and 2.24 W/m/K for MWNT films[75] with mass densities around 0.47 g/cm^3. (The cross-plane thermal conductivity is expected to be lower due to the layering of SWNTs during the assembly process.) The mass densities of the quasi-aligned MWNT film study[63] were greater than 1 g/cm^3. Our SWNT films had mass

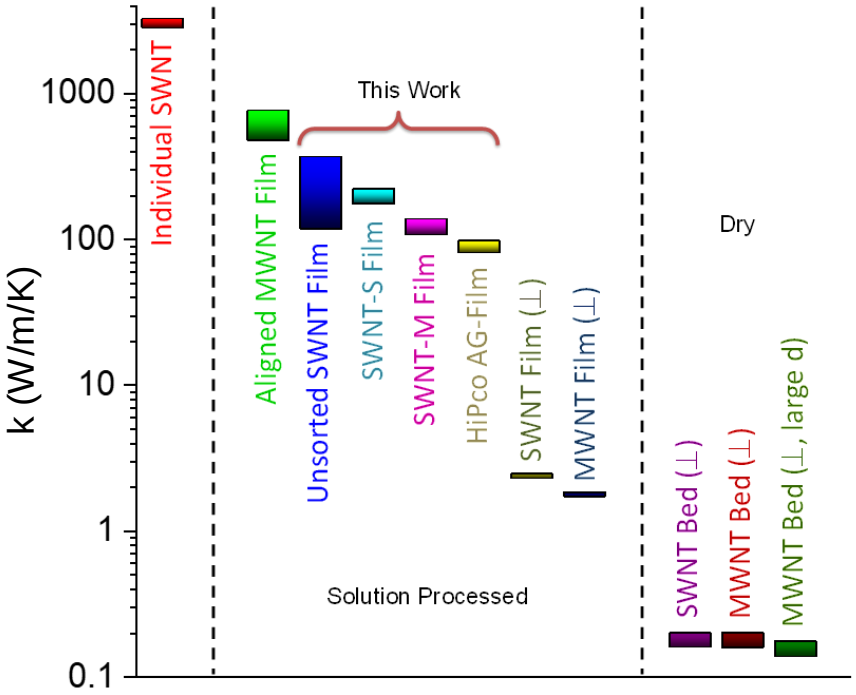

Figure 3.10. Summary of thermal conductivities of carbon nanotube films and composites near room temperature, including the results of this work: unsorted SWNT films, 90% semiconducting (SWNT-S) films, 90% metallic (SWNT-M) films, and HiPco as-grown (AG) films. The thermal conductivities of aligned MWNT films,[63] thick SWNT[74] and MWNT films,[35,75] and SWNT and MWNT dry beds[35,51] are also shown for comparison. (⊥) denotes cross-plane thermal conductivity from their respective references. The SWNT composites are separated into solution-processed films and dry-assembled mats; large diameter (*d*) mats have diameters ranging from 60-100 nm.

densities ranging from 0.5 – 1.1 g/cm^3 (Table 3.1). In comparison with the thermal conductivities of dry SWNT beds[51] that have thermal conductivities ranging from 0.13 to 0.19 W/m/K (with mass density 0.2 to 0.45 g/cm^3), the solution-processed films studied here are more thermally conductive in the in-plane direction. This can be attributed to many factors such as the higher mass density of our films, the length of the

SWNTs, bundling of the SWNTs, and the intrinsic thermal conductivity of individual nanotubes within the network.

Our experimental findings are consistent with theoretical values predicted by Volkov and Zhigilei,[53,54] who explored the strong influence of the mass density, length and thermal conductivity of individual SWNTs on the network thermal conductivity. In this context, part of the difference in thermal conductivities between the various nanotube films in our study may be due to different intrinsic *k* of the SWNTs in the films. For example, it is known that the effective *k* for both SWNTs and graphene depends on their length when it is comparable to the phonon mean free path.[34,70,76] The metallic SWNTs are shorter (~0.5 μm) and potentially more damaged than the semiconducting or purified SWNTs (~1 μm) after the sorting process, which is consistent with the observed lower overall *k* for the metallic SWNTs films.

3.4 Conclusions

In summary, we used a combination of IR thermometry and electrical measurements to characterize solution-processed films with controlled density of metallic and semiconducting SWNTs. Metallic films have higher electrical conductivity than semiconducting films (as expected) but lower thermal conductivity due to shorter tube lengths, which also leads to greater SWNT junction density. More importantly, the thermal conductivity of solution-processed SWNT networks is higher than that of dry-assembled SWNT beds[51] due to the vacuum filtration assembly process. Overall, we find that chirality plays essentially no role on thermal, which are controlled by the individual SWNT lengths, and overall junction and mass density of the SWNTs.

From a metrology standpoint, this study highlights the importance of adjusting for electrical and thermal contact resistance in measurements on such self-heated suspended films before intrinsic thermal parameters can be the deduced accurately. From a practical standpoint, these are important findings for lightweight heat spreaders and for thermoelectric energy harvesters. In particular, for thermoelectric applications[77] our results underscore that the figure of merit (*ZT*) of a SWNT sample cannot be estimated

based on previously measured results on different samples.[51] Rather, the thermal conductivity of SWNT thermoelectrics must be measured independently, because these quantities are sensitive to the morphology of the sample.

Chapter 4

Nanoscale On-Chip Thermoelectric Measurement of Sorted Semiconducting Carbon Nanotube Networks.

This chapter presents a comprehensive study on the thermoelectric properties of ultra-high purity sorted semiconducting single-walled carbon nanotube networks using an on-chip nanoscale thermometry platform. Sections of this chapter were taken from F. Lian *et al.*, "High Electron and Hole Thermopower in Ultra-Pure Carbon Nanotube Networks" (manuscript in preparation).

4.1 Thermoelectric Properties of Sorted Carbon Nanotube Networks

The unique physical and electronic structure of carbon nanotubes makes them a particularly interesting material to study for thermoelectric transport due to the enhancement of the Seebeck coefficient (*S*) from quantum confinement.[12] Recent calculations show the *S* of individual semiconducting single-walled carbon nanotubes (s-SWNTs) to have a strong dependence on the tube diameter as shown in Figure 4.1a. Hung *et al.*[78] predict that the *S* of a single nanotube can be as high as 2 mV/K which is an order of magnitude higher than Bi_2Te_3.[79] However, in a SWNT network, the *S* have been measured to be almost an order of magnitude lower than the predicted values.[48,77,80-84]

The National Renewable Energy Lab has published several comprehensive studies on thermoelectric transport in various s-SWNT networks.[83,84] Their first study on polymer wrapped, polymer sorted s-SWNTs compared a variety of nanotube diameters

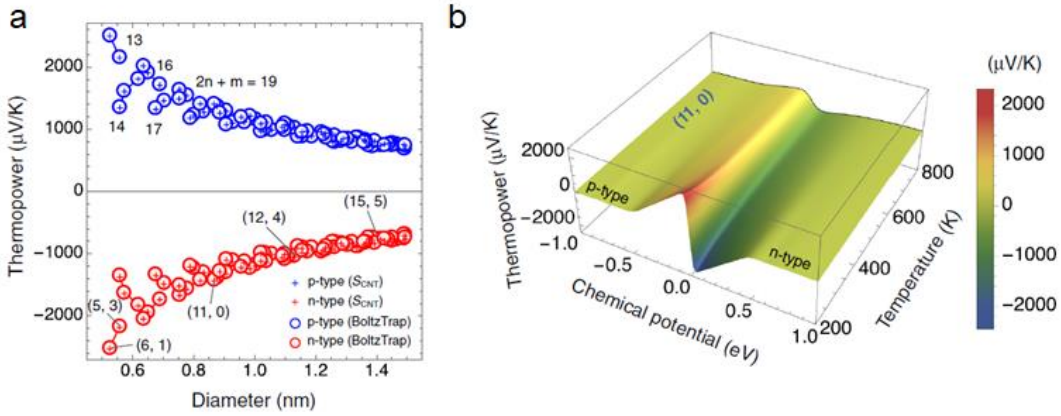

Figure 4.1. (a) Diameter dependence of Seebeck coefficient for an s-SWNT (b) temperature and Fermi energy (chemical potential) dependence of Seebeck coefficient. The Seebeck coefficient shows both electron and hole behavior since s-SWNTs have ambipolar transport characteristics. Figures adapted from Ref. 78.

and used triethyloxonium hexachloroantimonate (OA) to charge transfer dope sorted networks. They were able to achieve power factors greater than 340 μW/m/K^2.[83] In follow-up studies, polymer-free s-SWNT networks were studied with OA doping[85] as well as various n- and p- type dopants[84] to achieve up to 700 μW/m/K^2 with a material ZT ~ 0.12. Through the course of these studies, it was noted that the nanotube network morphology may play an important role in the transport properties.

Another study examined the role of junction type on Seebeck coefficients by varying concentration of metallic to semiconducting nanotubes in 300 nm filtration-assembled networks.[86] It was found that the network thermoelectric transport was junction dominated and that experimentally extracted $S_{junction}$ ~ 1 mV/K. A simple model was developed to calculate the Seebeck coefficient based on the fraction of s-SWNTs for a

mixed thin film. However, the s-SWNT network Seebeck coefficient was $S_{s\text{-}SWNT} \sim 88$ μV/K which is much lower than the predicted values for a single s-SWNT.

Experimentally studying fundamental thermoelectric transport in s-SWNT networks proves to be difficult due to a few key technical challenges. As synthesized, carbon nanotubes are either semiconducting or metallic, which leads to challenges for carbon nanotube-based materials where electronic type is crucial for material performance. Ultra-high purity (> 99%) sorting of semiconducting from metallic SWNTs and other impurities such as amorphous carbon requires a process that allows the removal of sorting polymers post separation in addition to preserving the excellent electrical properties of the tubes. Subsequently, uniform, dense deposition of s-SWNTs is also required for good electrical conduction and repeatable measurements. Finally, to study dependence of TE transport on both temperature and Fermi energy, measurements must take extra care due to the resistive nature of the s-SWNT networks which will be discussed later.

4.2 Nanoscale Electrothermal Platform

4.2.1 Platform Design and Calibration

There are many techniques to measure Seebeck coefficient. However, for samples that are a few nanometers thick, an electrothermal measurement technique can be used. By utilizing an on-chip method, we can tune the Fermi level of the material while conducting the measurement. There are a few main technical challenges to accurately measuring the Seebeck coefficient of a nanoscale material: accurate temperature measurements and reliable low voltage measurements.

We use a differential electrical resistance thermometry technique in which the change in electrical resistance is calibrated to temperature changes and used to measure on chip temperature gradients.[87,88] We use three metal lines, a heater and two thermometers, to perform thermometry as shown in Figure 4.2. The metal lines can be placed on top or under the sample of interest. The heater is electrically isolated from the sample and placement from thermometers depends on the heat spreading of the

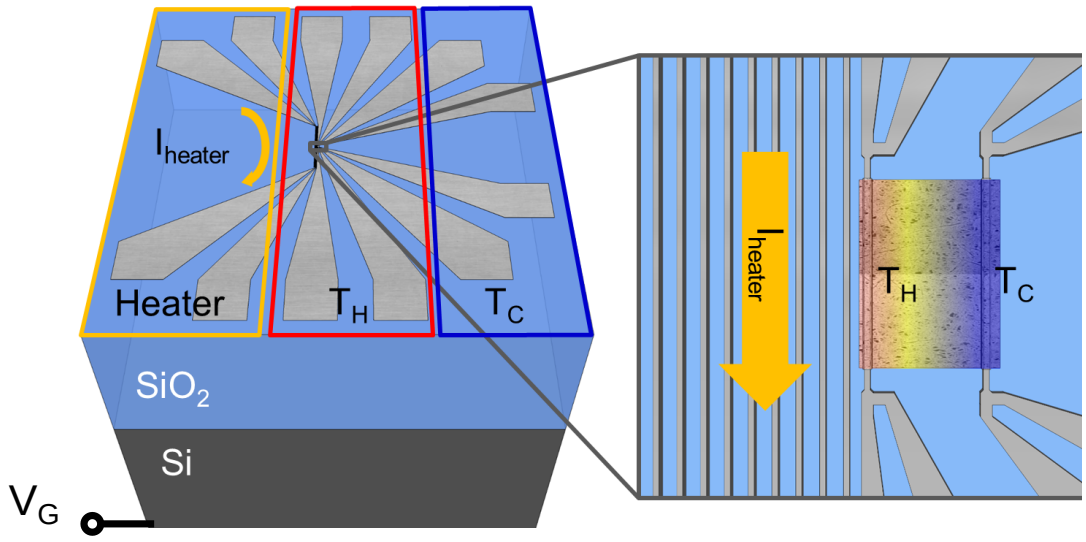

Figure 4.2. Thermometry platform layout. Each metal line uses a four-probe design to account for metal contact access resistances. Current is sourced through the heater and temperature is measured by the two thermometers. Thermometry platform is patterned on a thick oxide to provide large lateral heat flow.

substrate. In this case, there is a tradeoff between lateral heat spreading and electrostatic gate control. Thinner oxide would provide better gate control (carrier doping) at lower voltages. If the oxide is too thick, there will be a larger temperature drop ($\Delta T = T_H - T_C$) but, the voltages required for gating the semiconducting sample into the ON-state will be too high. We tested two oxide thicknesses: 300 nm and 550 nm. For the 550 nm thick oxide, gate voltages (V_G) needed to turn the sample ON were on the order of ±60 V. For 300 nm thick oxide, we were able to gate the material ON within a range of ±40 V. This becomes especially important when the threshold voltage (V_T) shifts during measurements due to hysteresis which will be discussed later in this chapter.

For the thermal gradient, we need a uniform temperature profile across the width of the sample. To achieve this, the heater to thermometer ratio needs to be greater than 10:1.[89] This is often not utilized in thermometry design for many 1D and 2D material measurements which may result in some errors since the measurement assumes a 1D

uniform temperature profile. In the case of our thermometers, we use a serpentine heater design to increase the electrical resistance of the heater. This allows us to achieve higher Joule heater power input ($Q = I^2R$) to increase sensitivity of the platform. The heaters in our platform are effectively 400 μm long (actual metal length is longer due to serpentine structure) while the thermometers are 20 μm and placed at the center of the heater. We use a four-probe design for the heater to bypass the resistance of the metal access lines which can be used to calculate the input power across the sample. The thermometer closest to the heater is located 1 μm away and measure the hot side temperature (T_H). The second thermometer is placed at distances of 10, 20, 30, 40, and 50 μm and measure the cold side temperature (T_C). There are no general limitations for the spacing between the thermometers if the T_H thermometer is close enough to the heater to sense a temperature rise. If the second thermometer is many thermal healing lengths away from the first, it can often be ignored in the measurement, but careful calibrations are required to verify the thermometer sensitivities. A variety of metals are generally used for differential thermometry such as Au, Pt, Pd, or other relatively inert metals. Since the thermometers are also electrical contacts to the sample, it is important to select a metal that would provide good electrical contact to the material.

Temperature calibrations are done in a Janis ST-100 Optical Cryostat. The chip is mounted to a dual in-line package (DIP) carrier and a Si diode is placed in contact with the carrier to measure temperatures during calibration. The sample is held under vacuum (~3×10^{-5} Torr) while the sample was cooled or heated. For each temperature, we collect 4 to 5 calibration sweeps. We use two SR 850 Lock-in Amplifiers to source and measure the thermometers. The circuit schematic for connecting the equipment to the device is shown in Figure 4.3a. We source a DC current I_h ~10 – 50 μA to the heater to measure the intrinsic resistance of the heater. The voltage is measured using a Keithley 2000 which can be connected at the same pad as the current source and ground pad or in the center voltage pads. Each thermometer is measured using a lock-in amplifier. The lock-in can source a sinusoidal voltage signal which is dropped across a large series resistor. Using the series resistor, we can change the current dropped across the device and resistor. We want the current to be on the order of microamps, so a resistor must be

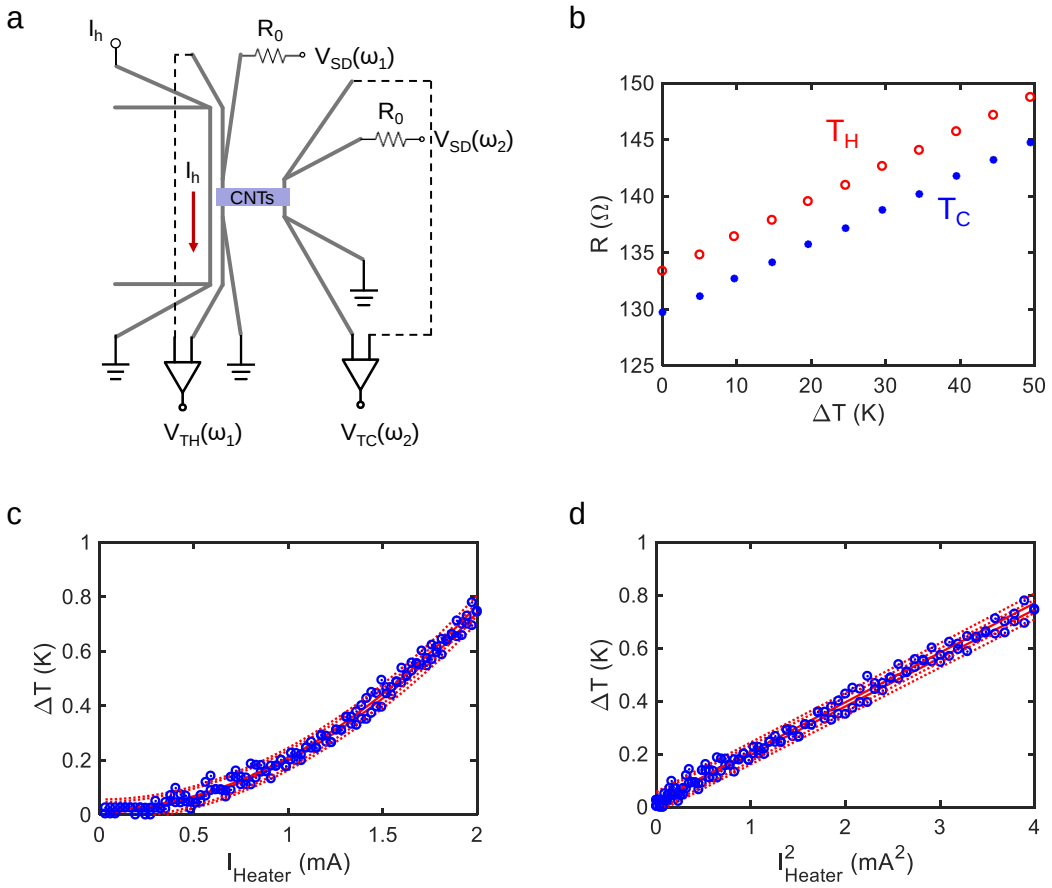

Figure 4.3. Thermometer calibration set-up. (a) Diagram to show measurement scheme for DC calibrations. (b) Temperature dependence of resistance for thermometers. (c) ΔT between thermometers located 10 μm apart for different heater currents. Since input power is Joule heating (I^2R), we expect and parabolic temperature rise. (d) ΔT for same device as a function of the square of the heater current. This should exhibit linear temperature dependence. Blue circles are experimentally measured points, red lines are fits with 95% confidence.

chosen accordingly. The voltage response signal is measured across the inner electrodes of the thermometers. The output signal is first fed into an SR 560 Low Noise Preamplifier in DC mode. We amplify the differential signal by about 100 times and then send it into the lock-in. Since the calibration is done simultaneously across both

thermometers, we choose frequencies carefully to minimize crosstalk between lines. The preamplifier is especially important in our set up for measuring high impedance samples which will be discussed later.

For the low power sweep, we measure resistances of all metal lines at low currents to prevent Joule heating in the lines. This measurement is used to calculate the temperature coefficient of resistance (TCR) and the resistance response to temperature (R vs. T) for the metals as shown in Figure 4.3b. We expect the metal resistance to have a linear response with temperature increase. The TCR that we measure varies depending on metal deposition method, tool, and conditions. Therefore, it is critical to calibrate all devices to ensure accurate thermal characteristics. We perform a batch of current sweeps where we increase the power in the heater line to induce Joule heating and measure the resistances of the two thermometer lines (with low currents) to calculate the temperature gradient across the two thermometers. Figures 4.3c and 4.3d shows the ΔT measured from the two thermometers for given heater excitation currents. Figure 4.3d shows the general ΔT vs. I^2 linear trend which confirms the temperature rise is due to Joule heating. These calibrations must be performed for all temperatures at which the sample will be measured to improve accuracy.

Generally, the largest source of error for Seebeck voltage measurements will result from the calibration measurements. These include metal resistance changes, cryostat stage temperature drifts, or thermal grease changes depending on vacuum conditions. First, the metal lines (especially heater lines) may experience current anneal effects depending on how much power is pushed through them. If this does happen, the resistance of the lines will change which would lead to issues with TCR measurements. Therefore, it is important to monitor the resistances of the metal lines before and after pushing large amounts of current through them. We generally take a low current measurement before and after two or three high current sweeps to get a large set of data. The second issue is the temperature inside the cryostat may drift. The temperature controller (Lakeshore 335) for the cryostat relies on Si diodes located in the heating element and on the DIP carrier. The PID controller tunes the heating power by

monitoring the fluctuations in the sensor of the heating element. This results in a lag for temperature stability in the sample. The thermal resistance of the ceramic DIP carrier is large enough to result in about 20-30 K temperature drop across the top and bottom of the sample carrier. This results in a large time constant for the temperature to stabilize. It usually takes about 15 – 20 minutes for the temperature to stabilize if there is no liquid helium flow through the system. To make sure temperatures are stable, we use a LabView script to monitor the fluctuations in the temperature at the DIP carrier sensor. We set the stabilization conditions by making sure the standard deviation of 10 temperature readings (taken 10-30 seconds apart) are less than a certain threshold (~0.1%).

The final source of error can result from how the chip and temperature sensors are mounted onto the DIP carrier. The chip can be mounted onto the carrier by thermal grease or silver paint. There are several kinds of thermal grease that can be used. However, depending on operating temperature, the thermal properties of the grease can change greatly. A cryogenic grease (Apiezon N) can remain viscous even at 4 K. At high temperatures, the grease becomes too viscous and can leak from between the carrier and the stage. The Janis ST-100 Cryostat has an operating temperature range of 4 K – 500 K. The low temperature limit is determined by the DIP carrier as mentioned earlier. There is no single thermal grease that can operate within these temperature limits. Furthermore, we found that high temperature thermal grease (Apiezon H) cannot go up to temperatures above 350 K in our vacuum system due to the vapor pressure limits. At high temperatures and low pressures, the grease begins to evaporate and coat the chamber and samples. We found that silver paint (PELCO High Performance Silver Paste) was best for mounting the same onto the DIP carrier.

4.2.2 DC vs. AC Seebeck Voltage Measurement

A Seebeck voltage is the open circuit voltage of a material in the presence of a temperature gradient. For this measurement, there are two approaches, a DC and an AC measurement. Figure 4.4 shows the circuit diagram for the DC measurement. We can do this measurement by sourcing a DC current using the Keithley 6221 while measuring

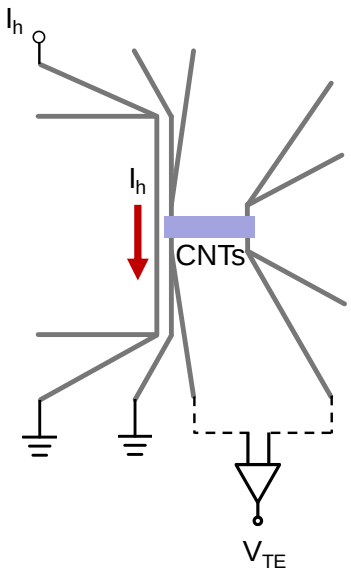

Figure 4.4. The DC measurement technique circuit diagram. DC current is sourced across the heater line while an open circuit voltage is measured across the two thermometer probes.

an open circuit voltage across the sample. There are a few choices for voltmeters to measure the voltage across the sample of interest. The Keithley 2000 that is used to measure the heater line resistance may seem like an obvious choice. However, the voltage resolution is quite poor. When the sample impedance is on the order of MΩs, the Keithley 2000 voltage readings become too noisy. To increase the measurement set-up impedance, we use can use an SR 560 Low Noise Preamplifier in series with the voltmeter. While doing the DC Seebeck measurement, it is important to sweep the current to make sure the measured voltage is induced by the temperature gradient. In this case, the change in voltage versus the heater current should be parabolic due Joule heating. The DC Seebeck voltage is expressed as

$$S_{DC} = -\frac{V_{TE}}{\Delta T} \tag{4.1}$$

where ΔT is the calibrated temperature gradient from the previous measurement and V_{TE} is the open-circuit voltage measurement across the sample (as shown in Figure 4.4).

DC Seebeck measurements are relatively simple to set up, but if there is an additional need to measure Seebeck voltage while varying electrostatic potential (gate voltage), then this measurement becomes too slow. This is because for every gate voltage, a DC Seebeck versus I_h measurement must be taken. Additionally, the sample may experience some hysteresis where the threshold voltage drifts as the Seebeck measurement is being taken. This would result in inaccurate results for the electrostatic potential during the measurement. One way to get around these issues is to use an AC measurement method.

For the AC measurement method, we apply an ω_1 frequency signal to the heater and measure the $2\omega_1$ signal which results from the temperature rise in the substrate. Figure 4.5a shows the circuit diagram for the AC measurement. In this case, we use a Keithley 6221 to source an AC current at frequency ω_1 across the heater lines. We can also measure the AC voltage at the inner electrodes to estimate the power dropped across the serpentine portion of the heater. This heating current can be expressed as

$$I_h = I_o \cos(\omega_1 t) \tag{4.2}$$

where I_o is the amplitude of the sinusoidal signal. The temperature rise form this heating current would be given as

$$\Delta T = \alpha \left(\frac{I_o^2}{2} \right) \tag{4.3}$$

where α is the proportional increase in temperature for a given I_o^2. The temperature rise results in a second harmonic voltage which can be expressed as

$$V_{2\omega_{LIA}} = \frac{\alpha I_o^2}{2} S \tag{4.4}$$

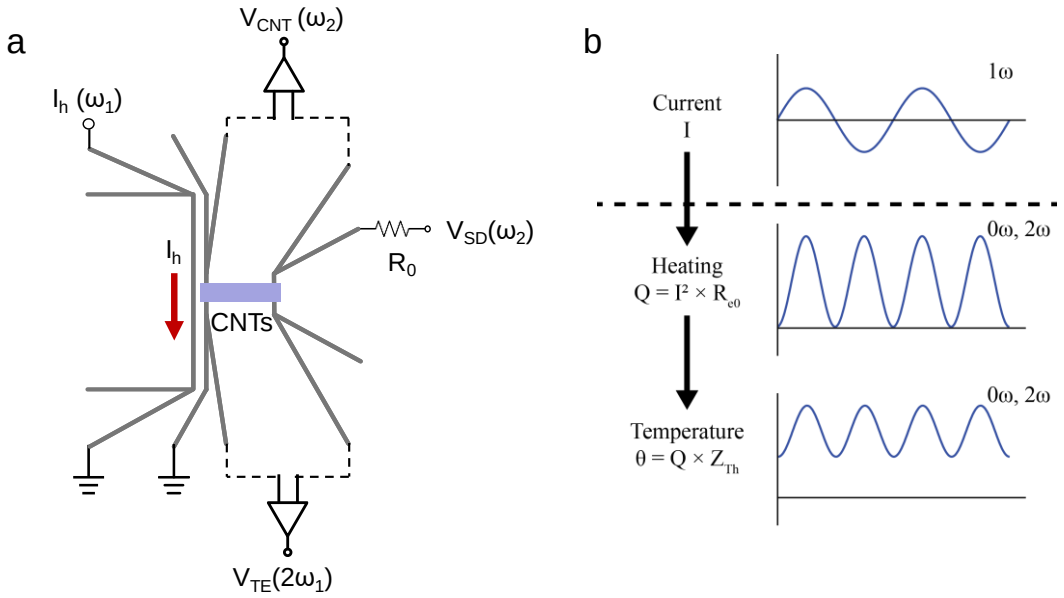

Figure 4.5. (a) AC measurement circuit diagram. An AC current at ω_1 frequency is sourced at the heater line. The $2\omega_1$ voltage is measured at the across the sample. A simultaneous conductance signal at ω_2 can be measured across the sample. (b) Signals diagram[90] showing a 1ω current signal inducing a 2ω heating power which results in a 2ω temperature signal that is a direct result of the Joule heating from the heating current.

where S is the Seebeck voltage of the material. To measure the AC Seebeck voltage, we use an SR 850 triggered by the current source. The Seebeck voltage is then given by

$$S = \frac{2\sqrt{2}V_{LI}}{\Delta T} \tag{4.5}$$

where V_{LI} is the root-mean-squared voltage measured by the lock-in amplifier. In our set-up, we feed the signal from the sample to a voltage preamplifier to amplify the signal that is measured by the lock-in (signals shown in Figure 4.5b). One important note is that the Seebeck voltage is measured by the lock-in at a 90° phase shift from the current signal. If the heater current phase is 0°, then the Y signal is the thermoelectrically induced voltage. If the ratio of Y/X is large (phase differs greatly from 90°), then there

are errors in the measurement the voltages cannot be trusted. This will be discussed more in Section 4.2.3.

For the sample conductance, a second lock-in can be used in parallel. A sinusoidal voltage signal at ω_2 frequency is sourced across a large resistor in series. The voltage signal from the sample is connected to an SR 560 preamplifier, amplified by 100x and then sent back into the lock-in. Since the second lock-in amplifier is operating at a different frequency (it is important to select a fundamental frequency that prevents crosstalk), these two measurements can be done simultaneously. In this case, the heater would be held at a constant AC current and only the gate voltage would be swept while the Seebeck and conductance voltage would be measured. Compared to the DC method, the AC technique is much faster for measuring gate voltage dependent Seebeck voltage which can take only a few minutes for the AC method. This helps reduce errors from sample hysteresis that would otherwise occur during a slow sweep. Since both the conductance and Seebeck voltage can be measured at the same time, this is a more reliable way to study any thermoelectric transport dependence on carrier densities.

4.2.3 High Impedance Samples and Measurement Validation

The nanoscale electrothermal platform has become a popular choice for measuring different low-dimensional materials such as MoS_2, phosphorene, and other novel nanomaterials. However, there are a few weaknesses to this measurement technique will be addressed in this section.

For samples that are resistive, great care must be taken to ensure accurate open circuit voltage measurements. In general, most multimeters such as the Keysight 34460 digital multimeter (DMM) or a Keithley 2000 has an input impedance of about 10 MΩ. If you are measuring a semiconducting sample in the off state, the sample resistance can be on the order of GΩ. In this case, the DMM would be unable to measure the sample accurately as the equipment would be lower resistance and provide a leakage path. Therefore thermoelectric measurements of low-dimensional semiconductors that are not gated ON may result in errors due to the high sample impedance.[91]

In the case of DC thermoelectric measurements of high resistance samples, it is difficult to check when the measurement is accurate. Two pieces of equipment can be used: a nanovoltmeter (Keithley 2182) or a high impedance semiconductor parameter analyzer (SPA) such as a Keithley 4200. The nanovoltmeter has an impedance of 50 GΩ and an SPA has input impedances on the order of TΩ. However, some samples with very high resistance have unstable DC open circuit voltage readings.

The lock-in amplifier for the AC method has an input impedance of 10 MΩ, but by sending the differential voltage through a voltage preamplifier (whose input impedance is 100 MΩ), we can boost the entire system impedance by an order of magnitude. In addition, the AC measurement method has a built-in validation parameter that was mentioned earlier. The thermally induced Seebeck voltage should be 90° out of phase with the heating current (signal should only have a Y component). This allows us to monitor the ratio between the Y and X component of the voltage to measure the error of the measurement. We can see a dependence of the error on the gate voltage because the gating turns on the network and induces more carriers which would decrease the sample resistance. Figure 4.6a shows the gate dependence of the Seebeck voltage and the error signal. In the case of our measurement, we define the error as the ratio X/Y. When taking AC Seebeck measurements, it is crucial to monitor errors to make sure they are within reasonable range. When the error is ≥ 20%, the measurement is most likely inaccurate. In Figure 4.6b., we can see that the error signal shows noise for regions where the semiconductor is turned off. We can use the error signal and the Seebeck voltage measurements to estimate the threshold voltage of the device.

To validate our platform and measurement method, we check our set up using both the DC and AC technique. We use $Ge_2Sb_2Te_5$ (GST) which is a phase change material commonly used in memory applications.[92] We sputtered a 45 nm film of GST onto prepatterned electrodes. We baked the sample at 150 °C for 10 minutes to ensure the film is in the face-centered cubic phase. In the FCC crystalline phase, the resistance was on the order of kΩs which is lower within the range of the equipment impedances. We

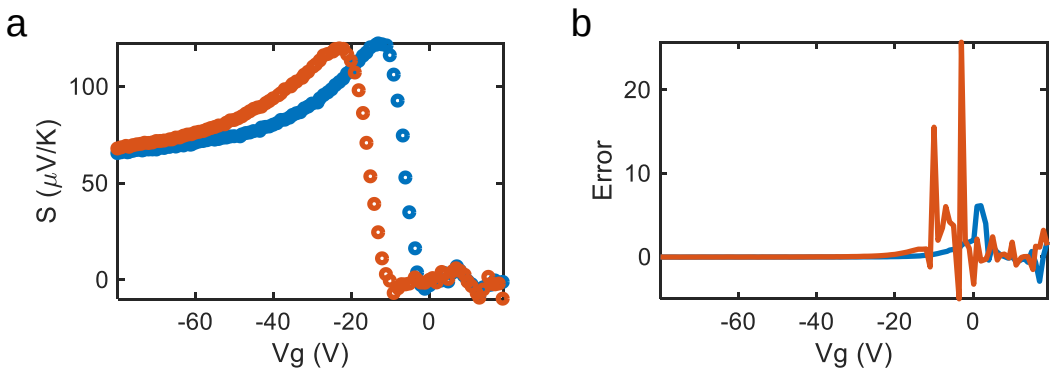

Figure 4.6. (a) Seebeck voltage measurement as a function of applied gate voltage (V_G) for a p-type semiconducting SWNT network. (b) Measurement error as defined by the ratio of the X- and Y-component of the voltage signal. When the semiconducting material is in the OFF state, the sample impedance is too high for the system to reliably measure the open circuit voltage resulting in a large error. As the sample is turned ON, the error becomes reduced. Once the sample resistance is within the measurable range of the equipment, the error becomes close to zero.

use a Keithley 2182 Nanovoltmeter to measure the DC Seebeck coefficient while sweeping the heater current. Figure 4.7 shows the linear dependence of Seebeck coefficient on the square of the heater current. This is due to the linear increase of ΔT with heater power. The calibration measurement in DC and AC gives a Seebeck coefficient of ~570 μV/K for the FCC GST. This falls within the range of measured values for GST of this resistivity.[89]

Once the test platform and measurement set-ups are validated, we can measure the Seebeck coefficient of other low-dimensional nanomaterials such as s-SWNT networks.

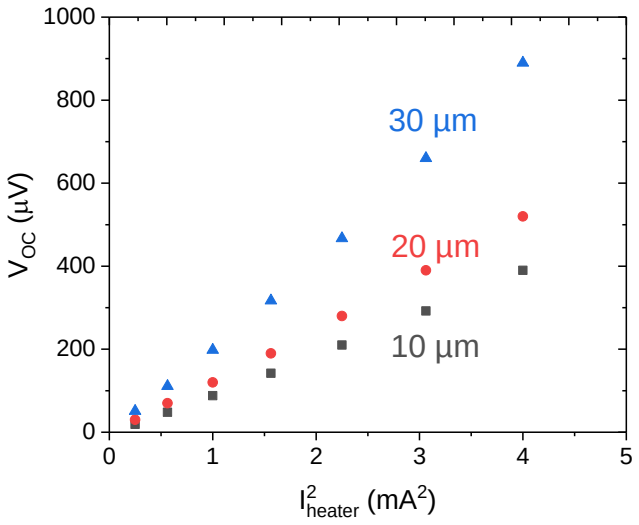

Figure 4.7. Open circuit thermoelectric voltage (V_{OC}) measured by the nanovoltmeter for a 45 nm GST film. As the heater current increases, V_{OC} increases linearly with the square of the heater current. For larger sample lengths the temperature gradients across the sample increase which leads to a length dependence for V_{OC}.

4.3 Sample Preparation

4.3.1 Sorting Carbon Nanotubes

To use SWNTs for any electronic or thermal electric applications, electronic-type purity is crucial. For transistors and thermoelectrics, any metallic tubes will cause a short between the contacts which would lead to poor performance. Therefore, SWNT sorting quality is extremely crucial for studying fundamental transport in s-SWNT networks. There are a few methods that have been explored for sorting SWNTs such as density gradient ultracentrifugation,[93] DNA wrapping,[94] chromatography,[95] and polymer wrapping.[96] The most scalable method for sorting SWNTs is polymer wrapping since it can be done relatively quickly and has high selectivity. However, a few main issues are sorting purity, sorting polymer removal, and overall cost for sorting.

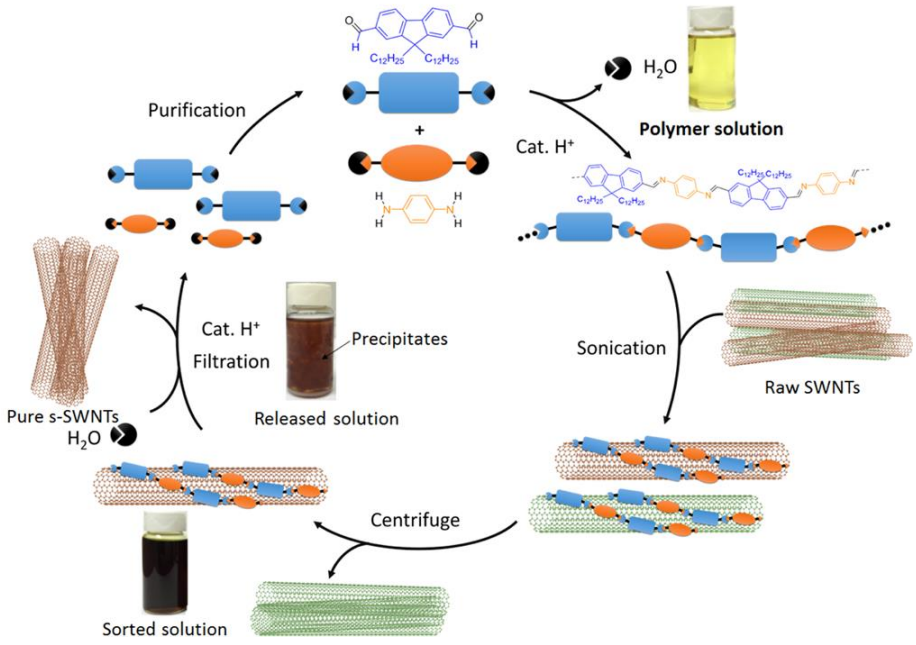

Figure 4.8. Semiconducting SWNT sorting process from Lei *et al.*[96] Starting from the top panel, a conjugated polymer is synthesized and sonicated with raw SWNTs. Sonication wraps the polymers around the SWNTs which can then be sonicated to separate the semiconducting SWNTs from the unwanted metallic SWNTs and other carbon impurities (with an overall yield of about 20%). After sorting, the s-SWNTs are deposited onto substrates and the polymer can be decomposed with acid and reused.

For the SWNTs in this work, we begin with plasma torch synthesized SWNTs. Plasma torch SWNTs are generally 1.1 – 1.5 nm diameter and have mobilities ranging from about 20 – 40 $cm^2/V/s$.[27] 5 mg of PF-PD and 15 mg of raw SWNTs (RN-020, Raymor Industries) were mixed in 25 mL of toluene and ultrasonicated for 30 min at an amplitude level of 45% (Cole Parmer ultrasonicator 750 W) while externally cooled with a dry ice bath (-78 °C). The mixture was centrifuged at 8000 rpm for 5 mins at 16 °C to remove most of the un-dispersed residues. Then the supernatant was centrifuged again at 17 000 rpm (22 000 g) for 25 min at 16 °C. 90 % of the supernatant

was collected and stored at 4 ºC to induce further aggregation of the residual metallic SWNTs. After SWNTs were slightly aggregated, the solution was sonicated in a bath sonicator for 10 mins and then centrifuged at 17 000 rpm (22 000 g) for 30 min at 16 ℃ to further remove the race amount of metallic tubes. 80 % of the supernatant was collected for later deposition and device fabrication. Figure 4.8 shows the process for sorting and separating the nanotubes.

4.3.2 Platform and Sample Fabrication

Thermometry platforms were fabricated at Northrop Grumman. Patterns were defined using wafer-scale photolithography. 5 nm/40 nm of Ti/Pt were deposited on 300 nm SiO_2/p++ Si using physical vapor deposition. Before s-SWNT deposition, prepatterned chips are H_2 passivated to improve hysteresis during measurements. The chips were placed on a quartz boat and annealed in a planarTECH 2'' diameter furnace. The temperature was ramped up to 400C from room temperature in 15 min and then annealed under vacuum for 60 min. 100 sccm H2 was flowed and tube pressure was around 0.964 Torr. After annealing, the furnace was cooled under vacuum to room temperature before venting to atmosphere.

Following s-SWNT deposition, electron beam lithography was used to define channels. Chips were first coated with a bilayer of PMMA (495 A2 and 950 A4). Channels were patterned over the thermometers using the JEOL JBX-6300 FS. We use a Cu hard mask to protect the s-SWNTs in the channel during O_2 plasma etching. In this case, the Cu mask step is crucial for preventing polymer residue. When resists are exposed to plasma during etching steps, they are often crosslinked and hard to remove using solvents. For O_2 sensitive materials such as carbon nanotubes, post-etching polymer resist residue can degrade device performance. Chips were etched in an Oxford PlasmaPro 80 for 2 minutes to remove unwanted s-SWNTs. The Cu hard mask was subsequently removed using Cu 49-1 Etchant from Transene. Following the Cu Etch, the s-SWNTs were soaked in acetone to remove acid dopants. Finally, before measuring, s-SWNTs are baked in air at 200 ˚C for 10 minutes.

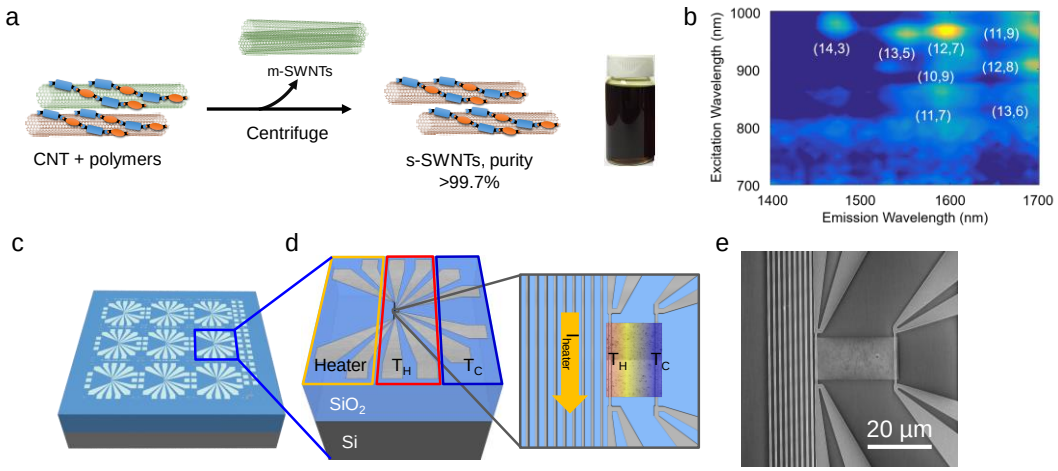

Figure 4.9. (a) Plasma discharged SWNTs are sorted using PF-PD. Unwanted tubes and amorphous carbon are centrifuged, separated and removed leaving a solution of > 99.9% s-SWNTs. (b) Photoluminescence excitation maps of the chiralities of SWNTs in the sorted solution. (c) Optical lithographically to pre-pattern thermometry platforms on 300 nm SiO_2/p++ Si wafers. (d) On-chip thermometry platform schematic shows the metal heater lines and thermometers design. An s-SWNT network is blanket deposited on the entire chip and then etched into channels across the thermometers (T_H and T_C). (e) SEM image of the final device with s-SWNTs channel.

4.4 Results and Interpretation

For the s-SWNT networks in this study, we measure the temperature and gate voltage dependence of the Seebeck coefficient under vacuum. Figure 4.10a. shows the measured Seebeck coefficient while varying over drive (V_G – V_T) voltage for 80 – 450 K. At 300 K, the Seebeck coefficient peaks at ~260 µV/K which is comparable to a previously measured single s-SWNT.[87] We measure 2-terminal electrical conductance (G) of the s-SWNT networks as shown in Figure 4.10b and show ON/OFF ratios $\geq 10^6$, which decreases with increasing temperature. From 80 K to 450 K, the s-SWNT

networks exhibit p-type transport which we attribute to atmospheric dopants on the s-SWNTs.[28,97] Calculations predict that the Seebeck coefficient would decrease with increasing temperatures (as shown in Figure 4.1b).

However, if the semiconductor is degenerate, we begin to see Mott-like thermoelectric transport which is characteristic of a metal.[88,91] Figure 4.10c shows the temperature dependence of the Seebeck coefficient for different overdrive ($V_G - V_T$)

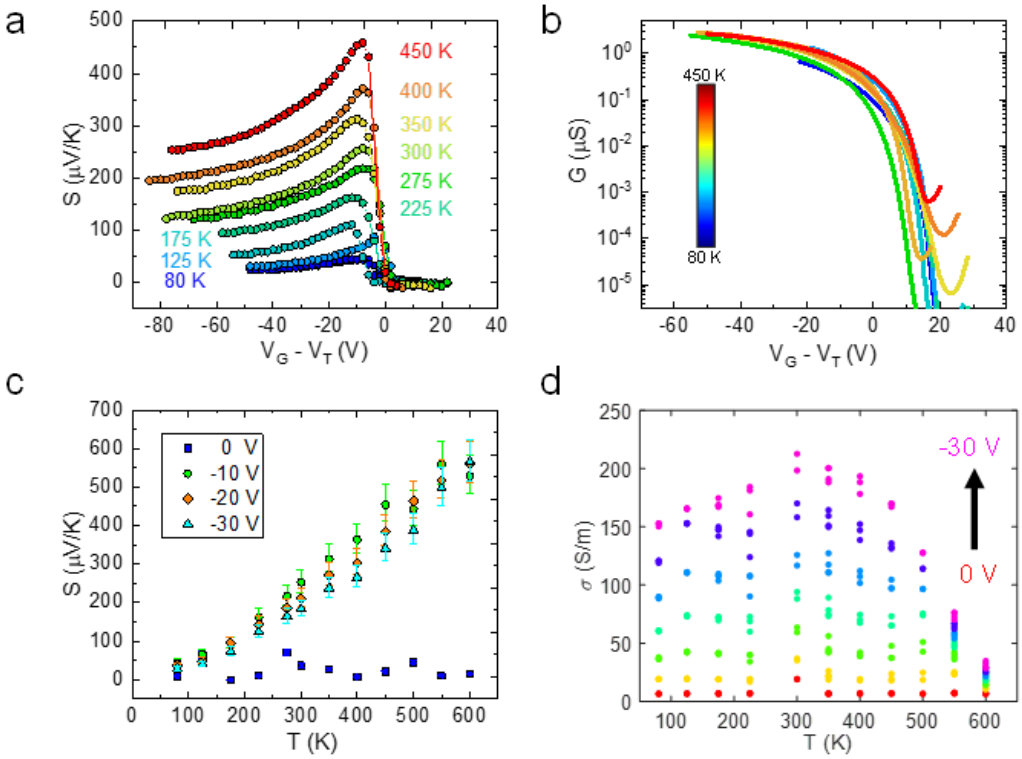

Figure 4.10. (a) Seebeck coefficient. (b) Electrical conductance as a function of gate overdrive ($V_{OD} = V_G - V_T$) for 80 – 450 K. (c) Seebeck coefficient as a function of temperature for fixed overdrive voltages of V_{OD} = 0, -10, -20, -30 V. (d) Temperature dependence of the electrical conductivity is consistent with hopping transport from 80 – 300 K. Above 300 K, de-doping of the s-SWNT networks cause conductivity to decrease while Seebeck coefficient continues to increase.

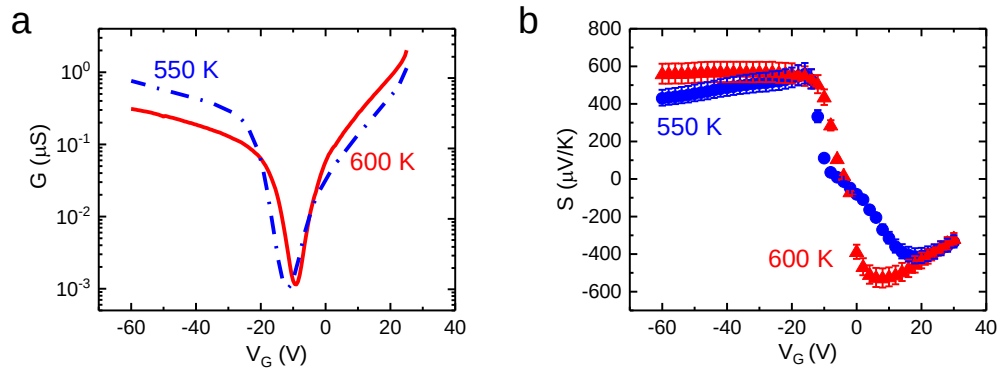

Figure 4.11. (a) Electrical conductance and (b) Seebeck coefficient versus gate voltage at 550 K and 600 K. As p-type dopants are driven off the s-SWNT network, we see the p-type conduction decreasing and n-type conduction increasing from 550 K to 600 K. The asymmetry in the Seebeck coefficient at 550 K stems from the presence of impurity charges in the channel.

voltages. *S* increases with temperature for overdrive voltages lower than the threshold voltage indicating Mott-like transport. We observe that at temperatures above 300 K, the network electrical conductivity begins to decrease (Figure 4.10d). We attribute this decrease to the de-doping of the network in vacuum which further enhances the Seebeck coefficient at high temperatures.

At above 450 K, enough of the p-type dopants are driven from the network surface such that ambipolar behavior can be observed electrically. In this measurement set-up ambipolar transport is not measurable thermoelectrically until enough electrons are conducting in the network at positive gate bias. Figure 4.11a shows the electrical conductance as a function of gate voltage at 550 K and 600 K. Conduction at the contacts are expected to be asymmetrical due to contact metal type since Pt contacts generally favor hole conduction. In our devices, we see improved electron conduction which can be explained by the H_2 passivation of the platforms before s-SWNT deposition which leads to a decrease in the metal work function.

From the Seebeck coefficient measurements, we clearly see the dopants being driven off the channel allowing ambipolar conduction (Figure 4.11b). In the low bias state, the s-SWNT network has a broad minimum conductivity around the Dirac-point at 550 K. Similar conduction behavior has been seen in graphene and can be attributed to the presence of charge impurities.[98] At 600 K, the Seebeck coefficient transitions sharply from maximum to minimum around the charge neutrality point which indicates a decrease in charge impurities or dopants. This is also shown in the conductance measurement (Figure 4.11a) where the electron current increases and hole current decreases relative to 550 K.

Despite our high measured Seebeck coefficients, our results are still not as high as individual s-SWNTs. To understand reasons for the discrepancy between measurements and theory, we look at morphology and junctions in the networks. Previous experiments and models on thermoelectric transport in SWNT networks have shown that similar to electrical and thermal conduction, Seebeck coefficient is also junction dominated.[86] Our first hypothesis is the role of SWNT bundling in solution processed networks. Previously reported s-SWNT networks had bundle diameters ranging from ~15 – 40 nm. Calculations have shown bundling to decrease the effective band gap of the s-SWNT bundle[99] which would result in a lower Seebeck coefficient. Using AFM (Figure 4.12a), we estimate the bundle diameters of our network to be approximately 2 – 2.4 nm (Figure 4.12b) in diameter suggesting the network bundles consist of only ~ 1 – 2 s-SWNTs. We propose this bundling effect to be an important contributing factor for the high Seebeck coefficients in these networks.

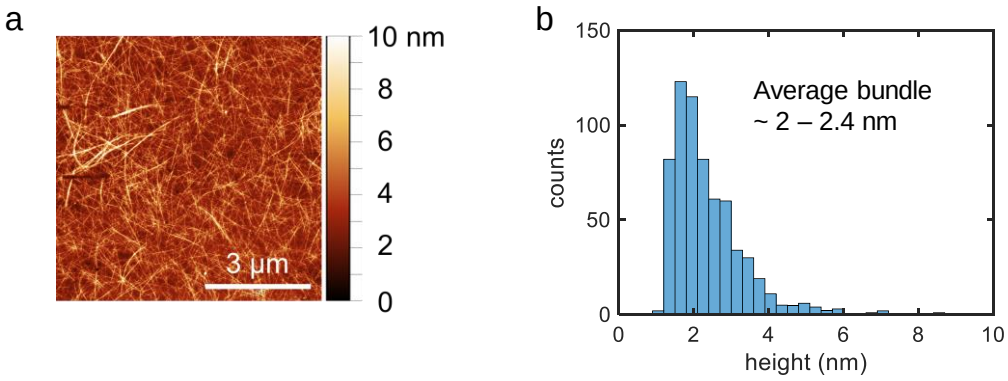

Figure 4.12. (a) AFM scan of s-SWNT network. (b) Bundle diameter distribution taken from AFM scans. The bundle diameters were calculated by averaging over 400 bundles across the AFM images, using the measured peak heights as the bundle diameter values.

4.5 Compact Model for Junction and s-SWNT ZT

Compact physical models allow us to study different transport mechanisms without relying on computationally expensive simulations such as molecular dynamics or density functional theory calculations. In electrical and thermal transport, junctions limit conduction, but their role in thermoelectric transport is still unknown. Here we present a compact model for thermoelectric transport including electrical conductance, Seebeck coefficient, and thermal conductance for individual s-SWNTs and a single junction between two s-SWNTs. We calibrate our model with experimental results and use it to compare the *ZT* of a single s-SWNT and a junction. Using our models, we find that junctions play an important role in s-SWNT network thermoelectrics and can be leveraged to improve thermoelectric performance. Figure 4.13 shows the s-SWNT junction schematic and physical parameters considered in our models. In the following sections, we will discuss the model for the transport across a junction and along a single tube.

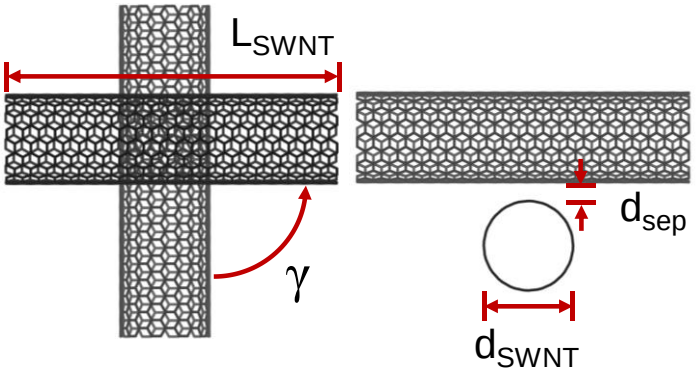

Figure 4.13. Schematic of a junction between two 1.3 nm diameter SWNTs. γ is the angle between the tubes, d_{sep} is the spacing between two tubes, and d_{SWNT} is the diameter of a single tube.

4.5.1 Electrical Conductance

Semiconducting single-walled carbon nanotubes (s-SWNTs) can have a range of electronic band-gaps based mainly on the diameter of the nanotube. The model for calculating the electrical conductance of an s-SWNT was previously published in the Pop group.[14] It is important to understand how the model works and since the conductance plays an important role in the Seebeck coefficient calculations. Furthermore, we develop junction electrical conductance model.

To calculate the electrical conductance, we can use the expression:[14]

$$G(T) = \frac{4q^2}{h} \sum_i \int_0^\infty \frac{\lambda(E,T)}{L + \lambda(E,T)} \left(-\frac{\partial f_0}{\partial E} \right) dE \tag{4.6}$$

where q is the elementary charge, h is the Planck constant, λ is the mean free path, E is energy, and f_0 is the equilibrium Fermi-Dirac distribution function. This model includes multiple bands, so the summation is over all the sub bands. In our model, the charge carrier density is given by

$$n = \int g_S(E)\, f_0(E) dE \tag{4.7}$$

where g_S is the density of states for a s-SWNT. The density of states can be written as:

$$g_S(E) = g_M \sum_i \left(1 - \frac{\Delta_i}{E}\right)^{-1/2} u\left(E - \Delta_i\right) \tag{4.8}$$

where $g_M = 4/(\pi\hbar v_F)$ is the single-band density of states for a metallic nanotube and v_F is the Fermi velocity. The band gap is calculated using:

$$E_G = \frac{4}{3}\frac{\hbar v_F}{d} \approx \frac{0.82}{d} \text{ eV} \tag{4.9}$$

where d is the diameter of the nanotube in nanometers. The model shows good agreement with experimental data and other simulations for carrier density dependent mobility. Figure 4.14 (a) shows the electrical conductance of a single-SWNT as a function of Fermi energy.

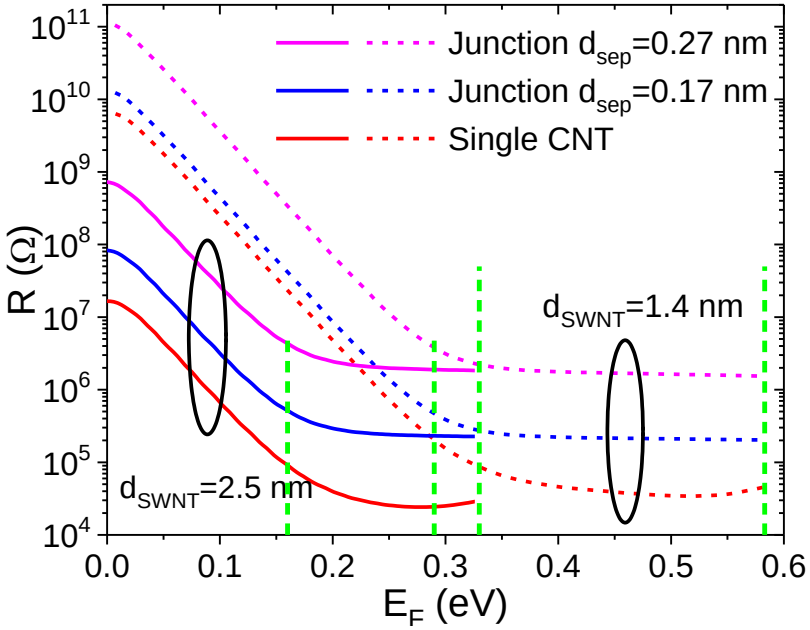

Figure 4.14. Electrical resistance (1/*G*) for a single s-SWNT (red) and junctions of 1.4 nm (dashed) and 2.5 nm (solid) as a function of Fermi energy relative to the middle of the band gap. The magenta lines are for junction separation distances of 0.27 nm and the blue lines are for separation spacings of 0.17 nm. The vertical green dashed lines show the edges of the first and second sub-bands (longer lines are for the 2.4 nm diameter tube)

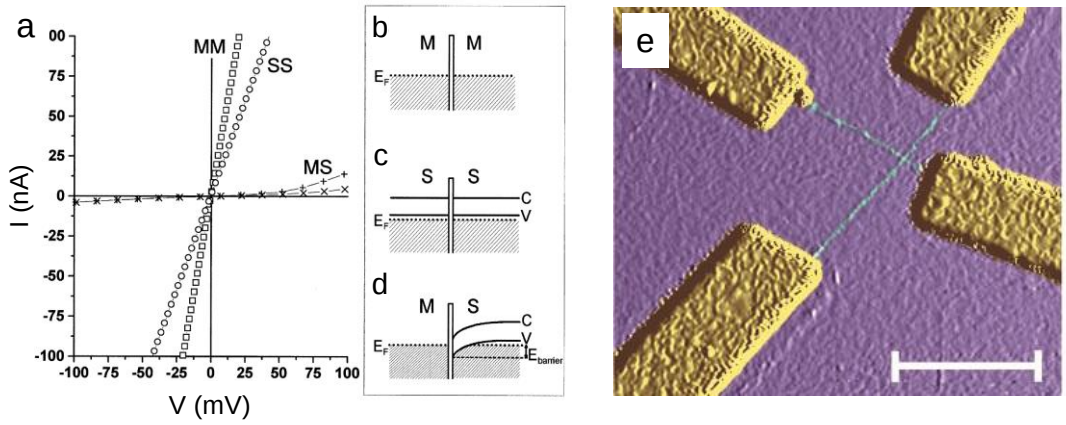

Figure 4.15. Figure recreated from Fuhrer *et al.*[57] (a) The current-voltage characteristics of MM, MS, and SS junctions at 200 K. The MS junctions exhibit a rectifying behavior due to the Schottky barrier (shown by the band diagrams in the (b) – (d)). (e) AFM scan of the junction.

For electrical resistance in a network of carbon nanotubes, junctions dominate the conduction due to its high resistance. Previous studies for a single junction between two different tubes have found that depending on the junction type. SWNT junctions are essentially tunnel barriers for electrons, but the resistance between metallic-metallic (MM), metallic-semiconducting (MS), and semiconducting-semiconducting (SS) vary due to the presence of an additional Schottky barrier between at an MS junction. MM and SS junctions both exhibit high conductances (Figure 4.15). For tunneling, we use a Wentzel-Kramers-Brillouin (WKB) approximation to calculate transmission probabilities for electrons. We assume that the spacing between two nanotubes forms a junction with a potential height equal to the nanotube work-function (ϕ_{SWNT}). The transmission probability (T_j) can be written as:

$$T_j(E) = \exp\left(-2d_{sep}\sqrt{2m_{e0}\left(\phi_{SWNT} - E\right)}/\hbar\right) \tag{4.10}$$

where d_{sep} is the junction spacing, m_{e0} is the effective mass of the electron. Based on Landauer formula for 1D conduction, the conductance across the junction is given by:

$$G = \frac{4q^2}{h}\int T(E)\left(-\frac{\partial f}{\partial E}\right)dE \tag{4.11}$$

where the coefficient outside of the integral is the quantized conductance. Experimental results found that MM junctions have conductances ranging from 0.086 – 0.26 q^2/h. SS junctions also exhibited relatively high junction conductances (0.01 – 0.06 q^2/h) which is likely a lower bound from measurements. However, when we find that our model overestimates the junction resistance when we use junction separation spacing on the order of 0.27 – 0.34 nm. We would expect the equilibrium spacing between two tubes to be the same as the interlayer spacing in graphite (~0.34 nm). Figure 4.16 shows the transmissions for different junction spacings. Fuhrer et al. also found that their models estimated transmission to be around $T_j \sim 2\times10^{-4}$ for the 0.34 nm spacing, but when they increased the contact pressure at the junction, $T_j \sim 0.04$ (which matched experimental results). This increase in contact pressure is likely due to substrate interactions with the SWNTs. In our model, we use the junction spacing to tune the transmission to match experimental results.

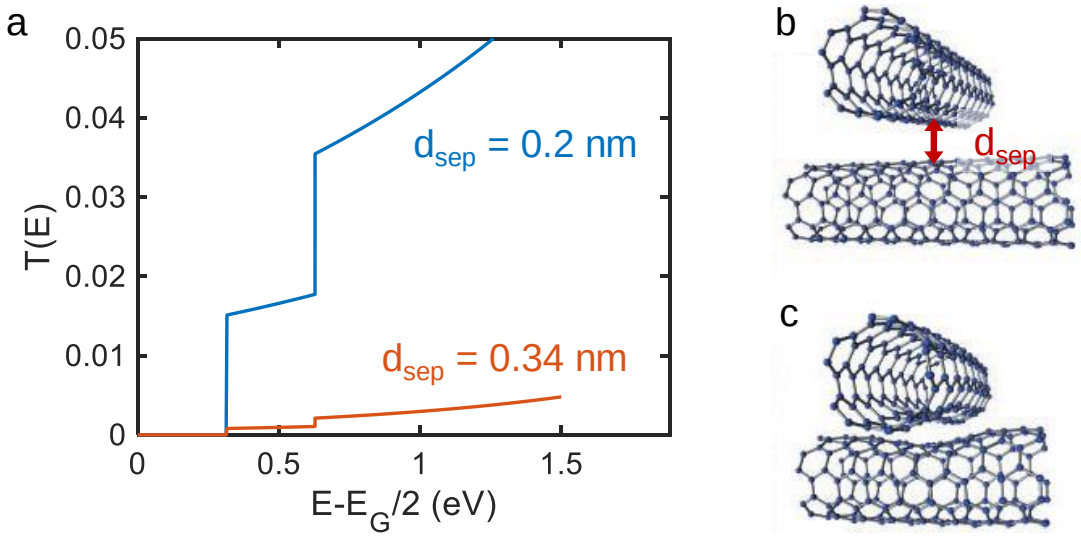

Figure 4.16. (a) Transmission probability as a function of energy for junctions of 0.34 nm and 0.2 nm. (b) Schematic of ideal model for the junction (0.34 nm).[57] (c) Schematic of junction with increased pressure at contacts.[57]

4.5.2 Seebeck Coefficient

In Section 1.2.1, we derived the equation for Seebeck coefficient from Boltzmann transport which is given by[11]:

$$S = \frac{k_B}{q} \frac{\int \sigma(E) \frac{(E - E_F)}{k_B T} \left(-\frac{\partial f}{\partial E} \right) dE}{\int \sigma(E) \left(-\frac{\partial f}{\partial E} \right) dE} \tag{4.12}$$

where k_B is the Boltzmann constant, $\sigma(E)$ is the differential conductivity, $f(E)$ is the Fermi function, and E is energy. We can calculate the Seebeck coefficient from the conductances calculated in the above section. Our model agrees well with previous calculations[78] as shown in Figure 4.17. Unlike the analytical expression in Hung et al., our model correctly calculates the Seebeck coefficient approaching zero as the Fermi level moves deep into the subbands.

For the junction Seebeck coefficient, we use the expression:

$$S_{junc} = \frac{1}{qT} \frac{\int T(E)(E - E_F) \left(-\frac{\partial f}{\partial E} \right) dE}{\int T(E) \left(-\frac{\partial f}{\partial E} \right) dE} \tag{4.13}$$

We find that the Seebeck coefficient for a junction between two s-SWNTs is comparable to that of the tube itself. Using our model, we calculate the Seebeck coefficients for s-SWNTs and junctions of 1.3 and 2.1 nm diameters (which is the common range of diameters in a sorted s-SWNT solution). As the diameter of the tube increases, the band gap decreases which leads to a decrease in the Seebeck coefficient.

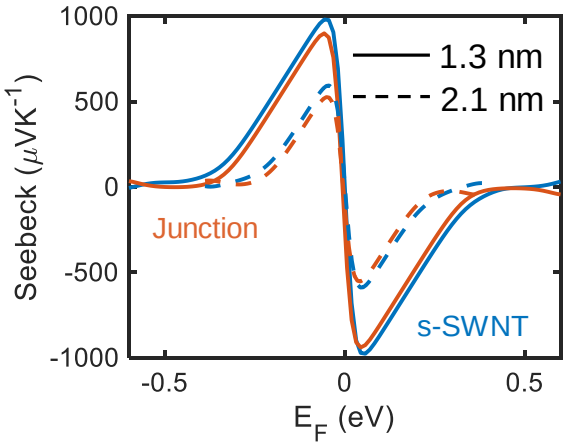

Figure 4.17. Seebeck coefficient versus Fermi energy for a 1.3 and 2.1 nm diameter tubes and their respective junctions. The peak of the 2.1 nm diameter Seebeck coefficient is about 50% of the 1.3 nm diameter tube.

4.5.3 Thermal Conductance

There have been many MD simulations[49,50] for SWNT junction conductances and a few experimental measurements for a multi-walled carbon nanotube junction.[100,101] Here we develop a compact thermal model to calculate the thermal conductance of a junction between two SWNTs.

To calculate the thermal resistance between two SWNTs, we begin with a Lennard-Jones (LJ) potential for carbon atoms in a graphene-graphene structure that has been approximated for two SWNTs.[102] The LJ potential is given as:

$$\varphi(r) = -\frac{A}{r^6} + \frac{B}{r^{12}} \tag{4.14}$$

where r is the center-to-center inter-tube spacing, A = 15.2 ev·Å^6 and B = 24100 eV·Å^{12}. Using the potential, we calculate the force $F(r,t)$ and potential $\varphi_{tt}(r,t)$ between to equivalent SWNTs with radius (t). The potential is given by:

$$\varphi_{tt}(r,t) = \frac{v^2}{\sin\gamma}\left(-\frac{Ag_A^*}{r^2} + \frac{Bg_B^*}{r^8}\right) \tag{4.15}$$

where $v \approx 0.393$ is the mean surface density of carbon atoms (atoms per Å^2). The additional terms can be found in the reference Zhbanov *et al.*[102] The force between two SWNTs is given as:

$$F(t,r) = \frac{v^2}{\sin\gamma}\left(-\frac{Af_A^*}{r^3} + \frac{Bf_B^*}{r^9}\right) \tag{4.16}$$

Using this model, we can estimate the equilibrium spacing (where the force is zero) between two SWNTs as shown in Figure 4.19a. The model estimates the equilibrium spacing between two crossed SWNTs to be around 2.92 – 2.93 Å. Interestingly, two parallel tubes have separation distances of ranging from 3.11 – 3.17 Å and the spacing between two fullerenes is about 2.95 Å. We find that the equilibrium spacing does not depend heavily on angle between the SWNTs (Figure 4.19b).

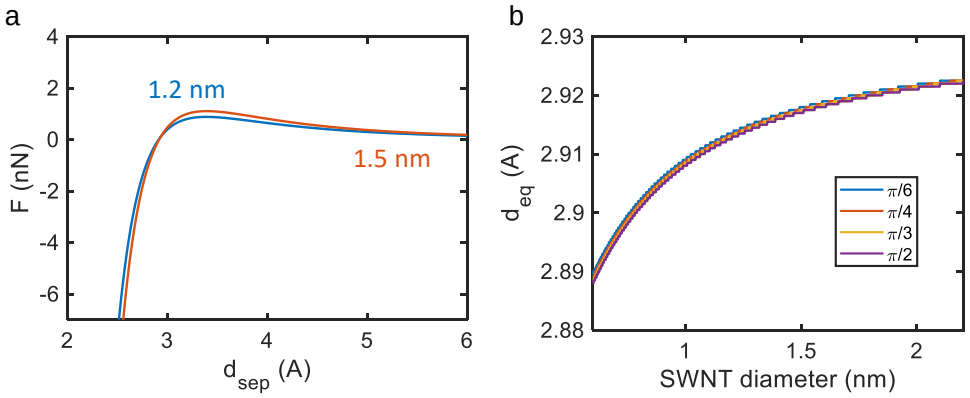

Figure 4.18. (a) Force vs. separation distance between two tubes. (b) Equilibrium spacing dependence on diameter for different angles between two tubes.

We calculate the spring constant between two SWNTs from the force calculations by using $k = dF/dr$. We find our spring constant calculations are in good agreement with experimentally estimated spring constant of a vdW junction between two boron

nitride nanoribbons.[103] We use a modified Acoustic Mismatch Model[104] (AMM) for phonon transmission ($\tau_{v\text{-}AMM}$):

$$\tau_{v-AMM} = \frac{1}{1+\frac{\omega^2}{4K_A^2}\left(\rho v_p\right)^2} \tag{4.17}$$

where ω is the phonon frequency, K_A is the spring constant, ρ is the mass density, and v_p is the phonon velocity. We assume the transverse acoustic phonon to be the main mode of transmission. The junction thermal conductance can be calculated the expression:

$$G_{junc} = \frac{1}{2}\int_0^{\omega_m} c_\omega v_\omega \tau_\omega d\omega \tag{4.18}$$

where c_ω is the phonon heat capacity, v_ω is the velocity, and τ_ω is the phonon transmission probability. The junction conductance is calculated by integrating over all the phonon frequencies. Figure 4.19a shows the spring constant and Figure 4.19b shows the junction thermal conductance dependence on SWNT junction separation. The lowest thermal conductance is for an angle of 90° since the contact area and transmission would be lowest between the two. We find there is a very small change (~120 – 140 pW/K) in thermal conductance for different diameter SWNTs. As the spacing between two SWNTs decrease, the junction thermal conductance saturates and reaches a "welded limit". MD simulations estimate a junction thermal conductance of about 130 pW/K which is in good agreement with our model.[50] Experimentally, only junctions between

MWNTs thermal conductances have been measured. From these measurements, SWNT junction thermal conduction was estimated to be around 20 pW/K.[100]

4.5 Implications for s-SWNT Thermoelectrics

To create bulk carbon-based thermoelectrics, we will likely rely on s-SWNT networks in which junctions will dominate transport. Therefore, it will be important to look at the figure of merit of a s-SWNT junction. Our model can help us estimate the *ZT* of a junction compared to an individual SWNT. We calibrate our models with experimental results for the junction electrical and thermal conductances. Figure 4.20 shows the junction *ZT* for a 1.3 and 2.1 nm diameter SWNT. In this calculation, we assume a junction spacing of 0.17 nm to match the junction electrical conductance to published studies.[57] For the thermal junction resistance, we take our calculated values and scale them to match experimental results. Remarkably, the *ZT* of a junction is over twenty times larger than a single SWNT. Despite a lower electrical conductance through the junction, the thermal conductance is many orders of magnitude lower across junction that it leads to an enhanced *ZT*. This is incredibly promising for SWNT-based thermoelectrics since junction dominated transport will play a major role.

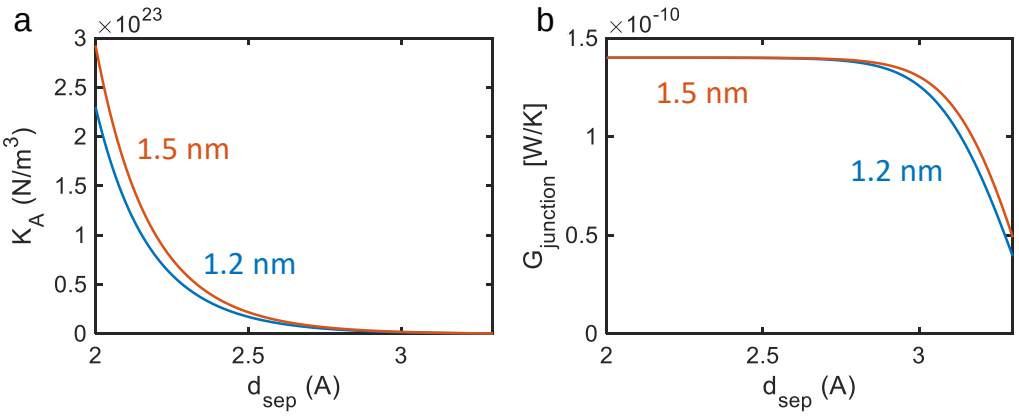

Figure 4.19. (a) Spring constant and (b) Junction thermal conductance as a function of separation distance between SWNTs. (c) Junction thermal conductance dependence on SWNT diameter and junction angle.

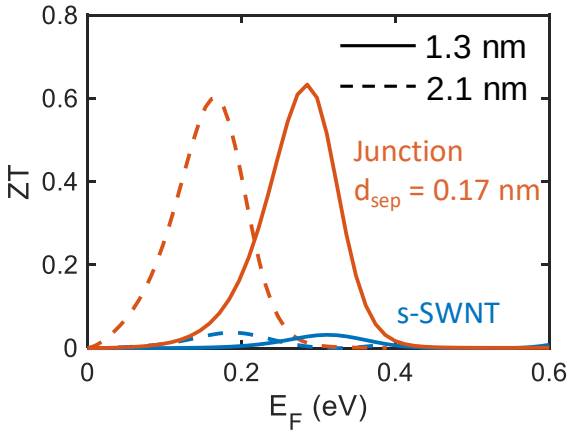

Figure 4.20. *ZT* of a single s-SWNT compared to a junction for 1.3 and 2.1 nm diameter tubes. The 0D junction has orders larger *ZT* because the thermal resistance of the junction compared to the s-SWNT is orders lower.

Engineering thermoelectric materials is a challenge due to the interdependent nature of Seebeck coefficient, thermal conductivity, and electrical conductivity. However, in a macroscopic material made up of 1D semiconductors such as an s-SWNT network this can be overcome due to the presence of junctions. Future work can use this to tune electrical transport across junctions while decreasing thermal conductance using methods such as junction functionalization. This work provides valuable insight towards engineering low cost, flexible, carbon-based thermoelectrics for Earth-based applications.

4.5 Conclusions

In summary, we utilized a nanoscale thermometry platform to study fundamental thermoelectric transport in high purity semiconducting single-walled carbon nanotube networks. We measured record high Seebeck coefficients and uncovered the importance of junctions through a comprehensive compact model. We learned that network morphology (bundle diameter, tube diameter, junction density) will play a crucial role for optimizing carbon-based thermoelectric design.

Chapter 5
Conclusion and Perspectives

This chapter summarizes the contributions of this thesis and discusses future research ideas. We discuss the use of carbon-based thermoelectrics beyond for applications beyond wearable energy harvesting.

5.1 s-SWNT-Based Thermoelectrics

Fundamentally, carbon nanotubes and carbon nanotube networks have the potential of changing the future of thermoelectrics. We discovered that nanotube composites have highly tunable thermal properties by leveraging the junction and mass density. We also uncovered the importance of junctions in a semiconducting carbon nanotube network. Since junctions and morphology (bundle and nanotube diameters) play such a large role in transport, we can tune the properties of these materials for a range of applications that extend beyond thermoelectrics such as sensors and passive heat spreaders. There are still quite a few technical challenges for working with carbon nanotubes for thermoelectrics. One of the topics that was briefly covered in this thesis is the need for both n- and p-type materials to make a thermoelectric generator. SWNTs are naturally doped p-type by water and oxygen. However, air stable n-type dopants still need additional research.

As we develop ways to control these material properties, it is important to understand various metrology limitations for studying thermal or thermoelectrical characteristics in low-dimensional nanomaterials. We discussed the different thermal metrologies that can probe properties on various length-scales ranging from nano- to macroscale. Each metrology has its trade-offs and sensitivity limitations, therefore carefully designing measurement rigs and samples is required for future work on

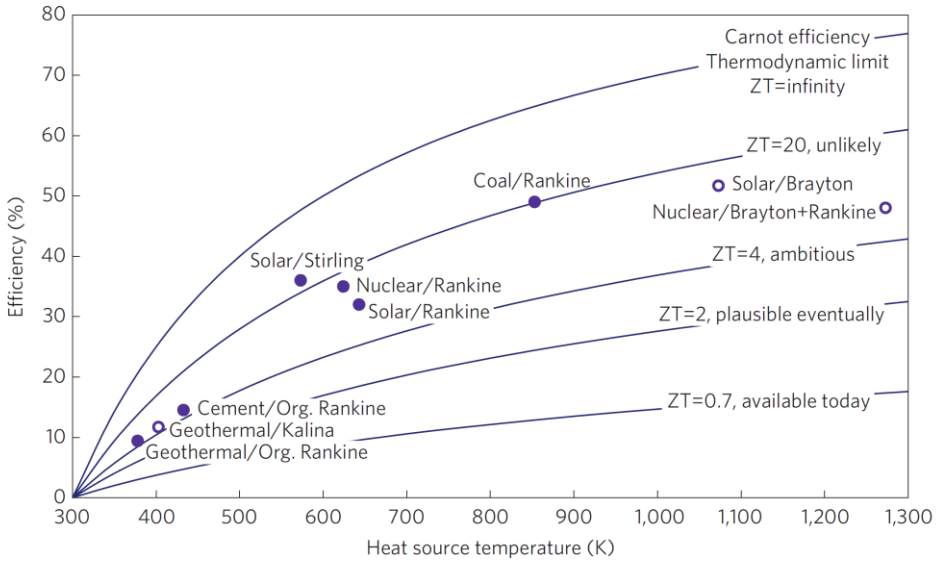

Figure 5.1. Efficiencies of current power generation technologies compared to the *ZT* required for a comparable thermoelectric generator. Figure reproduced from Ref. 8.

nanomaterials that push the limits of measurement resolutions (spatial, temperature, or temporal).

5.2 An Inconvenient Truth About Thermoelectrics

In 2009, Cronin Vining wrote a Nature Materials commentary[8] titled "An inconvenient truth about thermoelectrics." He pointed out that it was highly unlikely that thermoelectrics would ever make a large impact on climate change (reducing carbon emissions). Figure 5.1 shows the *ZT* required for efficiencies to reach other power generation technologies. For thermoelectrics to be competitive with current carbon emitting technologies such as coal power plants, we would need a $ZT \sim 20$.

Even though thermoelectrics cannot replace power plants, the amount of heat loss due to power generation inefficiencies is ~60 %. Every year, the US consumes ~100 quadrillion BTUs of energy. Low temperature waste heat (< 230 °C) is particularly

challenging to recover for electricity generation due to inefficiencies of heat engines at these temperatures.[105] Currently, we are looking at ~400 trillion BTUs of low temperature waste heat from combustion systems (boilers) alone.[106] If we can harvest a small fraction of that, the energy savings in terms of dollars and fuel would be substantial. One trillion BTUs is the equivalent of about five hundred 100-ton train cars of coal or one thousand 8000-gallon tankers of gasoline. At 1% waste heat recovery, we could potentially save > $200 million of refined gasoline. However, for widespread adoption of TEG for waste heat recovery, we would need to develop flexible, low cost materials that can be inserted into existing waste heat sources.

5.3 Flexible Thermoelectrics

For low-cost, flexible TEGs, we can use polymers as a support matrix for embedded nanoparticles.[48,107,108] There has been extensive research on the use of polymers both as a framework for embedding nanoparticles and as the active thermoelectric material. The polymers can be broken down into insulating and conductive polymers. Polymers have intrinsically low thermal conductivity due to its lack of a crystal structure. Therefore, nanoparticle doping has mainly been focused on improving the electrical conductivities of these composites.

PEDOT has been a focus for flexible TE research due to its high electrical conductivity. The highest *ZT* achieved for PEDOT reached $ZT \sim 0.42$,[109] but more work needs to be done on n-type polymer thermoelectrics. SWNT-PEDOT composites have also shown promising, however SWNTs were mainly used to improve electrical conductivities and not Seebeck coefficients.[110,111]

One major disadvantage to polymer TEs, however, is the thermal instability at high temperatures. PEDOT, for example, breaks down at about 100 °C. Polymers that can withstand higher temperatures such as polyvinylidene fluoride (PVDF) are insulating. Therefore, they would require additional improvements in electrical conductivity in addition to Seebeck coefficient. Studies have demonstrated a scalable low-cost fabric

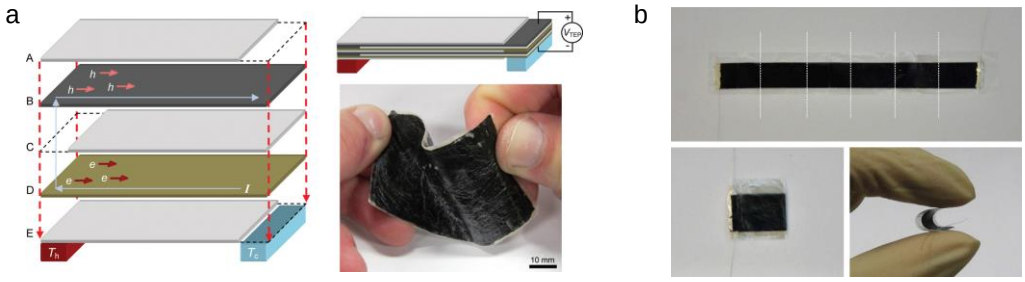

Figure 5.2. (a) PVDF-MWNT layered fabric for power generation. Figure reproduced from Ref. 110. (b) n- and p- type SWNT fabrics on polyethylene terephthalate (PET) substrates. Figure reproduced from Ref. 112.

based on MWNTs and PVDF.[110] However, performance is not optimized since MWNTs are essentially metallic and have low Seebeck coefficients.

Finally, a major challenge with flexible, polymer-based thermoelectrics is designing a device. Most studies have demonstrated flexible fabric-like thermoelectrics using a lateral heat flow as shown in Figure 5.2. The temperature gradient would realistically need to be in the cross-plane direction to optimize power density. A cross-plane polymer-based device can be realized using additive manufacturing methods such as screen- or 3D printing techniques.

5.4 Final Thoughts

The focus of this thesis was the development, validation, and utilization of different metrologies for studying nanomaterial properties. However, there is still room for improvements that can be made in metrology as well as fundamental physical understanding. First, for the 1D steady-state thermal measurement tool, there is a need to improve the losses due to radiation and convection. A smaller version of this tool can be installed in a vacuum system to reduce convective heat loss. To measure samples above room temperature, a series heater can be installed in the bottom meter bar to raise the average temperature across the sample. This would create a more robust measurement system overall.

For the suspended IR thermometry, we have implemented the system to study carbon nanofibers ~50 μm wide as well as 50 nm PEDOT:PSS thin films. For the tool, suspending samples is the main challenge since the Cu contacts are very large. However, this measurement technique and analysis can be applied to any suspended structure, therefore designing a Si-based platform would allow the study of smaller samples. A Si-based platform would also help with measuring a continuous sample TLM to improve contact resistance extraction.

In the on-chip thermoelectric measurements, additional improvements can be made to extract sample *ZT* in one platform. By combining supported thermal conductivity extractions[33] with the existing platform, we can extract all the sample properties required for *ZT* calculations. The main requirement is a four-probe heater must be used to measure the heat flux input. This type of measurement would need to be coupled with finite element modeling to account for heat losses into the substrate.

As we move forward to study more materials for thermoelectric and other applications, we will need to develop more metrologies to try and understand the fundamental physics in these materials. Low dimensional materials such as 2D transition metal dichalcogenides and 1D materials such as nanowires and nanotubes are extremely sensitive to surface defects due to their high surface area to volume ratio. This makes it crucial to understand how different factors will affect transport and how to engineer composites for TEGs.

Finally, for wearable thermoelectrics, the main issue is that our bodies are adaptive to temperatures. The human body responds to heat loss by trying to minimize losses. There are places on the body where we can place thermoelectrics (arteries close to the skin), but this may cause discomfort to the wearer. Since the temperature on the skin surface changes as the body adapts, additional work needs to be done on the power management circuits for thermoelectrics in which the thermal power source is unstable.

Bibliography

1 Crabtree, G., Kócs, E. & Trahey, L. The energy-storage frontier: Lithium-ion batteries and beyond. *MRS Bulletin* **40**, 1067-1078 (2015).

2 Starner, T. Human-powered wearable computing. *IBM Systems Journal* **35**, 618-629 (1996).

3 Wilson, H. J. *Wearables in the Workplace*, <https://hbr.org/2013/09/wearables-in-the-workplace> (2013).

4 Matthews, C. E. *et al.* Amount of Time Spent in Sedentary Behaviors in the United States, 2003–2004. *American Journal of Epidemiology* **167**, 875-881 (2008).

5 Sekine, K. <http://core.cypress.com/article/energy-harvesting-devices-replace-batteries-in-iot-sensors/#.WqbWKOjwaUl> (2014).

6 Laboratory, J. P. *Voyager to the Outer Planets and Into Interstellar Space*, <https://www.jpl.nasa.gov/news/fact_sheets/voyager.pdf> (2013).

7 Systems, R. P. *Multi-Mission Radioisotope Thermoelectric Generator (MMRTG)*, <https://mars.nasa.gov/msl/files/mep/MMRTG_FactSheet_update_10-2-13.pdf> (2013).

8 Vining, C. B. An inconvenient truth about thermoelectrics. *Nature Materials* **8**, 83-85 (2009).

9 Paradiso, J. A. & Starner, T. Energy scavenging for mobile and wireless electronics. *IEEE Pervasive Computing* **4**, 18-27 (2005).

10 Seebeck, T. J. Ueber die magnetische Polarisation der Metalle und Erze durch Temperaturdifferenz. *Annalen der Physik* **82**, 253-286 (1826).

11 Shakouri, A. Recent Developments in Semiconductor Thermoelectric Physics and Materials. *Annual Review of Materials Research* **41**, 399-431 (2011).

12 Hicks, L. D. & Dresselhaus, M. S. Thermoelectric figure of merit of a one-dimensional conductor. *Physical Review B* **47**, 16631 (1993).

13 Snyder, G. J. & Toberer, E. S. Complex thermoelectric materials. *Nature Materials* **7**, 105-114 (2008).

14 Yang, Z., Liao, A. & Pop, E. Multiband Mobility in Semiconducting Carbon Nanotubes. *IEEE Electron Device Letters* **30**, 1078-1080 (2009).

15 Zeghbroeck, B. V. *Principles of Semiconductor Devices*, <https://ecee.colorado.edu/~bart/book/book/chapter2/ch2_4.htm> (2011).

16 Goldsmid, H. J. The Electrical Conductivity and Thermoelectric Power of Bismuth Telluride. *Proceedings of the Physical Society* **71**, 633-646 (1958).

17 Goldsmid, H. J. The Thermal Conductivity of Bismuth Telluride. *Proceedings of the Physical Society. Section B* **69**, 203-209 (1956).

18 Glassbrenner, C. J. & Slack, G. A. Thermal Conductivity of Silicon and Germanium from 3K to the Melting Point. *Physical Review* **134**, A1058-A1069 (1964).

19 Chen, G. *Nanoscale energy transport and conversion : a parallel treatment of electrons, molecules, phonons, and photons*. (Oxford University Press, 2005).

20 Balandin, A. A. Thermal properties of graphene and nanostructured carbon materials. *Nature Materials* **10**, 569-581 (2011).

21 Hochbaum, A. I. *et al.* Enhanced thermoelectric performance of rough silicon nanowires. *Nature* **451**, 163-168 (2008).

22 Boukai, A. I. *et al.* Silicon nanowires as efficient thermoelectric materials. *Nature* **451**, 168-171 (2008).

23 Haxel, G. B., Hedrick, J. B., Orris, G. J., Stauffer, P. H. & Hendley Ii, J. W. Rare earth elements: critical resources for high technology. Report No. 087-02, (2002).

24 Dresselhaus, M. S., Dresselhaus, G. & Saito, R. Physics of carbon nanotubes. *Carbon* **33**, 883-891 (1995).

25 Grady, B. P. *Carbon Nanotube Composites*, <http://coecs.ou.edu/Brian.P.Grady/nanotube.html> (2013).

26 Kataura, H. *et al.* Optical properties of single-wall carbon nanotubes. *Synthetic Metals* **103**, 2555-2558 (1999).

27 Lei, T., Pochorovski, I. & Bao, Z. Separation of Semiconducting Carbon Nanotubes for Flexible and Stretchable Electronics Using Polymer Removable Method. *Accounts of Chemical Research* **50**, 1096-1104 (2017).

28 Collins, P. G. & Avouris, P. Nanotubes for electronics. *Sci Am* **283**, 62-69 (2000).

29 Sood, A. *et al.* Anisotropic and inhomogeneous thermal conduction in suspended thin-film polycrystalline diamond. *J Appl Phys* **119**, 175103 (2016).

30 Yalon, E. *et al.* Energy Dissipation in Monolayer MoS2 Electronics. *Nano Letters* **17**, 3429-3433 (2017).

31 Menges, F. *et al.* Temperature mapping of operating nanoscale devices by scanning probe thermometry. *Nature Communications* **7**, 10874 (2016).

32 Kodama, T. *et al.* Modulation of thermal and thermoelectric transport in individual carbon nanotubes by fullerene encapsulation. *Nature Materials* **16**, 892-898 (2017).

33 Li, Z., Bae, M.-H. & Pop, E. Substrate-supported thermometry platform for nanomaterials like graphene, nanotubes, and nanowires. *Applied Physics Letters* **105**, 023107 (2014).

34 Bae, M.-H. *et al.* Ballistic to diffusive crossover of heat flow in graphene ribbons. *Nature Communications* **4**, 1734 (2013).

35 Barako, M. T. *et al.* Thermal Conduction in Vertically Aligned Copper Nanowire Arrays and Composites. *ACS Applied Materials & Interfaces* **7**, 19251-19259 (2015).

36 Malekpour, H. & Balandin, A. A. Raman-based technique for measuring thermal conductivity of graphene and related materials. *Journal of Raman Spectroscopy* **49**, 106-120 (2018).

37 Grosse, K. L., Bae, M.-H., Lian, F., Pop, E. & King, W. P. Nanoscale Joule heating, Peltier cooling and current crowding at graphene-metal contacts. *Nature Nanotechnology* **6**, 287-290 (2011).

38 Yalon, E. *et al.* Spatially Resolved Thermometry of Resistive Memory Devices. *Scientific Reports* **7**, 15360 (2017).

39 Yu, C., Shi, L., Yao, Z., Li, D. & Majumdar, A. Thermal conductance and thermopower of an individual single-wall carbon nanotube. *Nano Letters* **5**, 1842-1846 (2005).

40 Cahill, D. G. Thermal conductivity measurement from 30 to 750 K: the 3ω method. *Review of Scientific Instruments* **61**, 802-808 (1990).

41 International, A. *ASTM D5470-12 Standard Test Method for Thermal Transmission Properties of Thermally Conductive Electrical Insulation Materials*.

42 Incropera, F. P. *Fundamentals of Heat and Mass Transfer*. (John Wiley & Sons, 2006).

43 Barako, M. T. *et al.* Dense Vertically Aligned Copper Nanowire Composites as High Performance Thermal Interface Materials. *ACS Applied Materials & Interfaces* **9**, 42067-42074 (2017).

44 Kallaher, R. L., Latham, C. A. & Sharifi, F. An apparatus for concurrent measurement of thermoelectric material parameters. *Review of Scientific Instruments* **84**, 013907 (2013).

45 Bar-Cohen, A., Matin, K. & Narumanchi, S. Nanothermal Interface Materials: Technology Review and Recent Results. *Journal of Electronic Packaging* **137**, 040803 (2015).

46 Rowe, D. M. *CRC Handbook of Thermoelectrics*. (CRC Press, 1995).

47 Furukawa, H., Cordova, K. E., O'Keeffe, M. & Yaghi, O. M. The Chemistry and Applications of Metal-Organic Frameworks. *Science* **341** (2013).

48 Blackburn, J. L., Ferguson, A. J., Cho, C. & Grunlan, J. C. Carbon-Nanotube-Based Thermoelectric Materials and Devices. *Advanced Materials*, 1704386 (2018).

49 Zhong, H. & Lukes, J. R. Interfacial thermal resistance between carbon nanotubes: Molecular dynamics simulations and analytical thermal modeling. *Physical Review B* **74**, 125403 (2006).

50 Salaway, R. N. & Zhigilei, L. V. Thermal conductance of carbon nanotube contacts: Molecular dynamics simulations and general description of the contact conductance. *Physical Review B* **94**, 014308 (2016).

51 Prasher, R. S. *et al.* Turning Carbon Nanotubes from Exceptional Heat Conductors into Insulators. *Physical Review Letters* **102**, 105901 (2009).

52 Hecht, D., Hu, L. & Grüner, G. Conductivity scaling with bundle length and diameter in single walled carbon nanotube networks. *Applied Physics Letters* **89**, 133112 (2006).

53 Volkov, A. N., Shiga, T., Nicholson, D., Shiomi, J. & Zhigilei, L. V. Effect of bending buckling of carbon nanotubes on thermal conductivity of carbon nanotube materials. *J Appl Phys* **111**, 053501 (2012).

54 Volkov, A. N. & Zhigilei, L. V. Scaling Laws and Mesoscopic Modeling of Thermal Conductivity in Carbon Nanotube Materials. *Physical Review Letters* **104**, 215902 (2010).

55 Volkov, A. N. & Zhigilei, L. V. Heat conduction in carbon nanotube materials: Strong effect of intrinsic thermal conductivity of carbon nanotubes. *Applied Physics Letters* **101**, 043113 (2012).

56 Behnam, A. *et al.* High-Field Transport and Thermal Reliability of Sorted Carbon Nanotube Network Devices. *ACS Nano* **7**, 482-490 (2013).

57 Fuhrer, M. S. *et al.* Crossed nanotube junctions. *Science* **288**, 494-497 (2000).

58 NanoIntegris. <http://nanointegris.com/>

59 Bae, M. H., Ong, Z. Y., Estrada, D. & Pop, E. Imaging, Simulation, and Electrostatic Control of Power Dissipation in Graphene Devices. *Nano Letters* **10**, 4787-4793 (2010).

60 Behnam, A. *et al.* High-Field Transport and Thermal Reliability of Sorted Carbon Nanotube Network Devices. *ACS Nano* **7**, 482-490 (2013).

61 Estrada, D. & Pop, E. Imaging dissipation and hot spots in carbon nanotube network transistors. *Applied Physics Letters* **98**, 073102 (2011).

62 St-Antoine, B. C., Menard, D. & Martel, R. Single-Walled Carbon Nanotube Thermopile For Broadband Light Detection. *Nano Letters* **11**, 609-613 (2011).

63 Zhang, L., Zhang, G., Liu, C. H. & Fan, S. S. High-Density Carbon Nanotube Buckypapers with Superior Transport and Mechanical Properties. *Nano Letters* **12**, 4848-4852 (2012).

64 Zhong, H. L. & Lukes, J. R. Interfacial thermal resistance between carbon nanotubes: Molecular dynamics simulations and analytical thermal modeling. *Physical Review B* **74**, 125403 (2006).

65 Pop, E., Mann, D. A., Goodson, K. E. & Dai, H. J. Electrical and thermal transport in metallic single-wall carbon nanotubes on insulating substrates. *J Appl Phys* **101**, 093710 (2007).

66 Wang, H.-D. *et al.* Heat transfer between an individual carbon nanotube and gas environment in a wide Knudsen number regime. *Journal of Nanomaterials* **2013**, 181543 (2013).

67 Liao, A. *et al.* Thermal dissipation and variability in electrical breakdown of carbon nanotube devices. *Physical Review B* **82**, 205406 (2010).

68 Pop, E., Varshney, V. & Roy, A. K. Thermal properties of graphene: Fundamentals and applications. *MRS Bulletin* **37**, 1273-1281 (2012).

69 Marconnet, A. M., Panzer, M. A. & Goodson, K. E. Thermal conduction phenomena in carbon nanotubes and related nanostructured materials. *Reviews of Modern Physics* **85**, 1295-1326 (2013).

70 Xu, Y., Li, Z. & Duan, W. Thermal and Thermoelectric Properties of Graphene. *Small* **10**, 2182-2199 (2014).

71 Lindsay, L., Broido, D. A. & Mingo, N. Diameter dependence of carbon nanotube thermal conductivity and extension to the graphene limit. *Physical Review B* **82**, 161402 (2010).

72 Hone, J., Whitney, M., Piskoti, C. & Zettl, A. Thermal conductivity of single-walled carbon nanotubes. *Physical Review B* **59**, R2514-R2516 (1999).

73 Hecht, D., Hu, L. B. & Gruner, G. Conductivity scaling with bundle length and diameter in single walled carbon nanotube networks. *Applied Physics Letters* **89**, 133112 (2006).

74 Hong, W. T. & Tai, N. H. Investigations on the thermal conductivity of composites reinforced with carbon nanotubes. *Diamond and Related Materials* **17**, 1577-1581 (2008).

75 Chen, H. Y. *et al.* Architecting Three-Dimensional Networks in Carbon Nanotube Buckypapers for Thermal Interface Materials. *Journal of Physical Chemistry C* **116**, 3903-3909 (2012).

76 Shulaker, M. M. *et al.* Carbon Nanotube Circuit Integration up to Sub-20 nm Channel Lengths. *ACS Nano* **8**, 3434-3443 (2014).

77 Nakai, Y. *et al.* Giant Seebeck coefficient in semiconducting single-wall carbon nanotube film. *Applied Physics Express* **7**, 025103 (2014).

78 Hung, N. T., Nugraha, A. R. T., Hasdeo, E. H., Dresselhaus, M. S. & Saito, R. Diameter dependence of thermoelectric power of semiconducting carbon nanotubes. *Physical Review B* **92**, 165426 (2015).

79 Wright, D. A. Thermoelectric Properties of Bismuth Telluride and its Alloys. *Nature* **181**, 834 (1958).

80 Shimizu, S. *et al.* Thermoelectric Detection of Multi-Subband Density of States in Semiconducting and Metallic Single-Walled Carbon Nanotubes. *Small* **12**, 3388-3392 (2016).

81 Yanagi, K. *et al.* Tuning of the thermoelectric properties of one-dimensional material networks by electric double layer techniques using ionic liquids. *Nano Letters* **14**, 6437-6442 (2014).

82 Yanagi, K. *et al.* Transport mechanisms in metallic and semiconducting single-wall carbon nanotube networks. *ACS Nano* **4**, 4027-4032 (2010).

83 Avery, A. D. *et al.* Tailored semiconducting carbon nanotube networks with enhanced thermoelectric properties. *Nature Energy* **1**, 16033 (2016).

84 MacLeod, B. A. *et al.* Large n- and p-type thermoelectric power factors from doped semiconducting single-walled carbon nanotube thin films. *Energy & Environmental Science* **10**, 2168-2179 (2017).

85 Norton-Baker, B. *et al.* Polymer-Free Carbon Nanotube Thermoelectrics with Improved Charge Carrier Transport and Power Factor. *ACS Energy Letters* **1**, 1212-1220 (2016).

86 Piao, M. *et al.* Effect of Intertube Junctions on the Thermoelectric Power of Monodispersed Single Walled Carbon Nanotube Networks. *The Journal of Physical Chemistry C* **118**, 26454-26461 (2014).

87 Small, J. P., Perez, K. M. & Kim, P. Modulation of thermoelectric power of individual carbon nanotubes. *Physical Review Letters* **91**, 256801 (2003).

88 Zuev, Y. M., Chang, W. & Kim, P. Thermoelectric and magnetothermoelectric transport measurements of graphene. *Physical Review Letters* **102**, 096807 (2009).

89 Lee, J. *et al.* Thermal conductivity anisotropy and grain structure in Ge2Sb2Te5 films. *J Appl Phys* **109**, 084902 (2011).

90 Dames, C. & Chen, G. 1ω,2ω, and 3ω methods for measurements of thermal properties. *Review of Scientific Instruments* **76**, 124902 (2005).

91 Kayyalha, M., Maassen, J., Lundstrom, M., Shi, L. & Chen, Y. P. Gate-tunable and thickness-dependent electronic and thermoelectric transport in few-layer MoS2. *J Appl Phys* **120**, 134305 (2016).

92 Wong, H. S. P. *et al*. Phase Change Memory. *Proceedings of the IEEE* **98**, 2201-2227 (2010).

93 Arnold, M. S., Green, A. A., Hulvat, J. F., Stupp, S. I. & Hersam, M. C. Sorting carbon nanotubes by electronic structure using density differentiation. *Nature Nanotechnology* **1**, 60-65 (2006).

94 Zheng, M. *et al*. Structure-Based Carbon Nanotube Sorting by Sequence-Dependent DNA Assembly. *Science* **302**, 1545 (2003).

95 Liu, H., Nishide, D., Tanaka, T. & Kataura, H. Large-scale single-chirality separation of single-wall carbon nanotubes by simple gel chromatography. *Nature Communications* **2**, 309 (2011).

96 Lei, T., Chen, X., Pitner, G., Wong, H. S. & Bao, Z. Removable and Recyclable Conjugated Polymers for Highly Selective and High-Yield Dispersion and Release of Low-Cost Carbon Nanotubes. *Journal of the American Chemical Society* **138**, 802-805 (2016).

97 Donghun, K., Noejung, P., Ju-hye, K., Eunju, B. & Wanjun, P. Oxygen-induced p-type doping of a long individual single-walled carbon nanotube. *Nanotechnology* **16**, 1048 (2005).

98 Liu, X., Wang, D., Wei, P., Zhu, L. & Shi, J. Effect of carrier mobility on magnetothermoelectric transport properties of graphene. *Physical Review B* **86**, 155414 (2012).

99 Elkadi, A., Decrossas, E. & El-Ghazaly, S. in *2013 IEEE International Symposium on Electromagnetic Compatibility* 534-538 (2013).

100 Yang, J. *et al.* Contact thermal resistance between individual multiwall carbon nanotubes. *Applied Physics Letters* **96**, 023109 (2010).

101 Yang, J. *et al.* Phonon Transport through Point Contacts between Graphitic Nanomaterials. *Physical Review Letters* **112**, 205901 (2014).

102 Zhbanov, A. I., Pogorelov, E. G. & Chang, Y.-C. Van der Waals Interaction between Two Crossed Carbon Nanotubes. *ACS Nano* **4**, 5937-5945 (2010).

103 Yang, J. *et al.* Enhanced and switchable nanoscale thermal conduction due to van der Waals interfaces. *Nature Nanotechnology* **7**, 91-95 (2011).

104 Prasher, R. Acoustic mismatch model for thermal contact resistance of van der Waals contacts. *Applied Physics Letters* **94**, 041905 (2009).

105 Gingerich, D. B. & Mauter, M. S. Quantity, Quality, and Availability of Waste Heat from United States Thermal Power Generation. *Environmental Science & Technology* **49**, 8297-8306 (2015).

106 BCS, I. *Waste Heat Recovery: Technology and Opportunities in U.S. Industry*. (United States. Department of Energy. Office of Energy Efficiency and Renewable Energy, 2008).

107 Dames, C. Cost optimization of thermoelectric materials for power generation: The case for ZT at (almost) any cost. *Scripta Materialia* **111**, 16-22 (2016).

108 Yee, S. K., LeBlanc, S., Goodson, K. E. & Dames, C. $ per W metrics for thermoelectric power generation: beyond ZT. *Energy & Environmental Science* **6**, 2561-2571 (2013).

109 Kim, G. H., Shao, L., Zhang, K. & Pipe, K. P. Engineered doping of organic semiconductors for enhanced thermoelectric efficiency. *Nature Materials* **12**, 719–723 (2013).

110 Hewitt, C. A. *et al.* Multilayered Carbon Nanotube/Polymer Composite Based Thermoelectric Fabrics. *Nano Letters* **12**, 1307-1310 (2012).

111 Yu, C., Choi, K., Yin, L. & Grunlan, J. C. Light-Weight Flexible Carbon Nanotube Based Organic Composites with Large Thermoelectric Power Factors. *ACS Nano* **5**, 7885-7892 (2011).

112 Zhou, W. *et al.* High-performance and compact-designed flexible thermoelectric modules enabled by a reticulate carbon nanotube architecture. *Nature Communications* **8**, 14886 (2017).